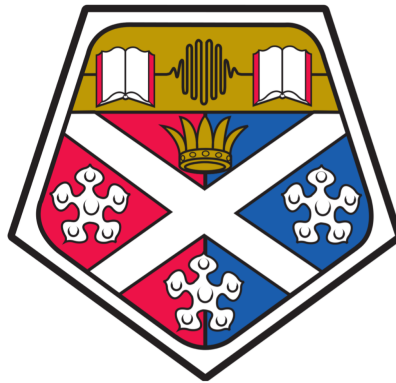


A thesis submitted in partial fulfilment
of the requirements for the degree of
Doctor of Philosophy

Dissipative Engineering of Cold Atoms in Optical Lattices

Jorge Yago Malo



University of Strathclyde
Department of Physics and SUPA

January 2019

This thesis is the result of the author's original research. It has been composed by the author and has not been previously submitted for examination which has led to the award of a degree.

The copyright of this thesis belongs to the author under the terms of the United Kingdom Copyright Acts as qualified by University of Strathclyde Regulation 3.50. Due acknowledgement must always be made of the use of any material contained in, or derived from, this thesis.

Signed:

Date:

For my family and my cacti

Abstract

Cold atom systems in optical lattices provide a promising platform for a wide variety of applications, ranging from quantum simulation to quantum metrology, due to their extremely high tunability and the ability to derive microscopic models under well-controlled approximations that allows us to model them. The proper characterization of those systems requires, in many scenarios, taking into account that they are subject to some dissipation sources, as dissipation can drastically modify the behaviour of the known phases of matter or even generate new ones.

In this thesis, we investigate several important examples of dissipative many-body dynamics. The first one relates to the use of engineered coupling to the environment, both coherent and dissipative, to robustly create spin-symmetric fermionic states. This scheme, which combines a Raman transfer between Bloch bands and sympathetic cooling with a reservoir gas, prepares entangled states that exhibit quantum enhanced precision for metrology. In the second topic we explore, we focus on the study of one-dimensional spinless fermions and hard-core bosons. We observe how dissipation induces differences in local observables that are identical in the closed system. The third topic that we include in this thesis focuses on characterizing the role of dissipation, specifically particle loss and dephasing, in the long-time behaviour of many-body localized systems. We analyze under which conditions dissipation leads to thermalization in the localized phase.

In all these projects, we make use of tensor network techniques to tackle the open system dynamics combining matrix product states and matrix product operator approaches, in both cases, exploiting symmetries in the system to optimize the numerical performance.

All in all, the application of open system ideas to the study of quantum many-body problems provides not only an improved description of the realistic scenario but also can give access novel tools to engineer cold atomic systems in regimes that are not accessible for closed systems.

Acknowledgement

I would like to take this opportunity to reflect upon all the people who made this journey possible. The people who impacted the development of not only my scientific career, but also helped me become the person I am now, who is very different to the scared guy that landed in Glasgow in September 2014. I will always be grateful for their support and guidance. First, I would like to thank my supervisor, Andrew Daley, who gave me the opportunity to move to another country for the first time, taught me scientific techniques that will impact my future career and gave me the chance to travel to incredible places and meet more scientists than I could have dreamt of meeting. Moreover, I would like to thank all my friends in Glasgow from Alex, Andreas, Annemarie, Anton, Araceli, Eduardo, Enrico, Francois (x2), Gioan, Guanglei, Jacopo, Jack, Jennifer, Jess, José, Leire, Liviu, Matteo, Maria, Phil, Roger, Rosaria, Sapphire, Saubhik, Suzanne, Tristan or Tom to Tomohiro and so many more, like the Glasgow Lindyhoppers. They all have been the light I needed in all those dark Scottish winters. I shared with you fun moments, new hobbies, boardgames, coffees (plenty of them), trips, beers, laughter and tears and you all always showed me how it is possible to be far away from your own home and yet feel so welcome and happy.

Now, I would like to thank my family for their love and infinite support that I could feel every day despite the distance between us. I will never forget their pride when I accomplished my PhD and I hope that I manage to make them proud throughout the rest of my career and my life. Especially, my mother who has taught me the most important values in life and was always the best example of what hard work could achieve. Finally, I would like to thank my girlfriend, Alice, who joined this adventure midway but quickly became an essential part of it. Thanks for making me believe that I could achieve anything when I could not see it myself and thanks for your patience and love that made me feel like the luckiest person.

I think that this thesis could have never been what it is without you all, and for that, once again I am grateful to you.

Contents

Abstract	iii
Acknowledgements	iv
1 Introduction	1
1.1 Cold atoms in optical lattices	1
1.2 Numerical methods in quantum many-body systems	3
1.3 Open systems: Reservoir Engineering	5
1.4 Thesis Outline	7
1.5 Publications during PhD	9
2 Cold Atoms in Optical Lattices	11
2.1 Introduction	11
2.2 Atom-light interaction	11
2.3 Atom-atom interaction	14
2.4 Cold atoms in optical lattices	16
2.4.1 Hubbard model	20
2.4.1.1 Jordan-Wigner transformation	21
2.4.2 Bose-Hubbard model	23
3 Dynamics in closed and open quantum systems	25
3.1 Introduction	25
3.2 Closed quantum systems: exact diagonalisation	26
3.2.1 Numerical tools for exact diagonalisation	27
3.3 Open quantum systems	30
3.3.1 Deriving the Master Equation	31

3.3.2	Quantum trajectories: Monte Carlo wave-function method	36
3.4	Reservoir engineering and dark-state preparation	39
4	Reduced Hilbert Space Techniques: Density Matrix Renormalization Group (DMRG)	41
4.1	Matrix product state representation	42
4.1.1	Graphical notation for tensor networks	42
4.1.2	Matrix product state construction	44
4.1.3	Canonical form of an MPS and gauge freedom	47
4.1.3.1	Typical operations in canonical form	50
4.1.4	Entanglement and truncation error	52
4.1.5	Vidal's notation	54
4.1.6	Symmetries and number conserving codes	54
4.2	Matrix product operators	57
4.2.1	MPO example: Transverse Ising model	59
4.3	Time-Evolving Block Decimation	60
4.3.1	Imaginary time evolution	63
4.4	Variational state search	63
4.4.1	Ground state variational search	64
4.4.2	Variational search for a dissipative steady state	66
4.5	Conclusion	73
5	Dissipative engineering of spin-entangled fermionic states in optical lattices	74
5.1	Introduction	74
5.2	The dissipative model	75
5.2.1	Making use of the fermionic symmetries to design our dissipator	76
5.2.1.1	Two-site system	77
5.2.1.2	General system sizes	78
5.3	Proposed scheme	81
5.3.1	Stroboscopic implementation of the driving scheme	84
5.4	Steady state characterization and Quantum Fisher Information	85
5.4.1	Bloch Sphere picture and Ramsey spectroscopy	85

5.4.2	Quantum Fisher Information	86
5.4.3	Reduction to the pure state expression for the QFI	89
5.4.4	Relation between angular momentum and QFI	92
5.5	Numerical results	94
5.5.1	Dependence on the onsite interaction	94
5.5.2	Filling factor dependence of the dissipative driving	96
5.5.3	Spatial inhomogeneities: magnetic field gradient	98
5.5.4	Average steady values	100
5.5.5	State purity analysis	101
5.6	Conclusion	103
6	Particle statistics and dynamics with loss of ultracold atoms in optical lattices	105
6.1	Introduction	105
6.2	Similarities of spinless fermions and hard-core bosons	107
6.2.1	Tensor network representation of loss operators	112
6.3	Differences in the presence of deterministic losses	114
6.4	Differences in the presence of stochastic losses	120
6.4.1	Closed system dynamics	121
6.4.2	Stochastic losses and the distinction of fermions and HCBs . .	124
6.4.3	Analysis of the density fluctuation damping	129
6.4.4	Short-time imbalance profile	130
6.5	Conclusion	131
7	Dynamics of many-body localization in the presence of particle loss	133
7.1	Introduction	133
7.2	Overview on MBL in cold atoms	135
7.2.1	Thermalization in quantum systems and Eigenstate Thermalization Hypothesis	135
7.2.2	Localization in quantum systems	137
7.3	System description	139
7.3.1	Imbalance: experimental figure of merit	139
7.3.2	Open system dynamics	141
7.3.3	Bond-Parity Matrix-Product-Operator Formalism	141

7.4	Results	145
7.4.1	Pure loss	145
7.4.2	Dephasing and loss: weak interactions	148
7.4.3	Dephasing and loss: strong interactions	149
7.4.4	Evolution of entanglement entropy	151
7.5	Conclusion	155
8	Conclusion	156
	Bibliography	159

Chapter 1

Introduction

In recent years, atomic, molecular and optical (AMO) systems have proven to be a reliable platform towards Quantum Simulation [1]. This is due to the high tunability and control over the practical implementation of these systems and the well-understood microscopic models that describe them which we can derive from first principles. In particular, thanks to their high controllability the study of quantum many-body systems have permitted access to interesting quantum regimes at low temperatures in a robust manner; thus, allowing us to investigate fundamental questions of condensed matter physics (e.g. high- T_c superconductors [2]), explain out-of-equilibrium dynamics or becoming a relevant platform for high-precision measurements [3, 4, 5] exploiting their non-trivial quantum properties, e.g. Ramsey spectroscopy experiments with cold atoms [6].

1.1 Cold atoms in optical lattices

The study of many-body systems as a platform for quantum simulation reached an important milestone when the quantum phase transition between a Mott Insulator and a superfluid was observed in a bosonic system [7, 8]. This was only possible due to the enormous development of cooling techniques over the course of many decades including laser cooling [9], evaporative cooling [10] and, later on, sympathetic cooling [11, 12] which is specially relevant for the case of fermions and will play a vital role in the discussion of chapter 5.

By combining different cooling schemes, dilute clouds of neutral atoms (with typical densities of $\sim 10^{13} - 10^{15} \text{ cm}^{-3}$) were cooled to a Bose-Einstein condensate (BEC) (originally in three different alkali atomic species ^{87}Rb [13], ^7Li [14] and ^{23}Na [15], but currently in a broad variety of alkali, alkaline-earth and lanthanide atoms) reaching temperatures of the order of nK. An essential advantage of these systems is that not only temperatures but also dynamical scales correspond to frequencies $\sim \text{Hz-kHz}$ allowing for the experimental observation of the dynamics of the system in real time; with dynamics being also compatible with typical lifetimes ($\gtrsim 1 \text{ s}$) of atomic states.

As mentioned before, another essential feature in quantum many-body systems is the high degree of control and tunability that AMO systems possess. In particular, given the temperature of the system, the inter-particle interaction can be characterized (from low-energy scattering theory) by a single parameter, the scattering length. This parameter can be continuously tuned through a wide range of interaction strength (including attractive and repulsive) via optical or magnetic Feshbach resonances [16, 17, 18].

In addition, neutral atoms can be trapped in periodic potentials formed by counter-propagating laser beams, known as optical lattices. Due to the AC-Stark shift these neutral atoms are trapped in the intensity minima (or maxima) of a far detuned laser field with trapping frequencies of the order of several recoil energies¹. It is important to note that experimental development has allowed to not only realize bosonic models in the lattice like the Bose-Hubbard model [19] but also to trap fermionic species [20, 21, 22] observing non-trivial quantum phases [23, 24].

In this thesis, we will focus on the case of dilute Fermi gases trapped in optical lattices. The realization of non-trivial phases of fermions was especially challenging due to the slowing down of scattering at low-temperatures caused by the fermionic Pauli blocking. This problem was overcome by using s-wave evaporative cooling with several spin species. Alternatively, it is possible to use sympathetic cooling [11, 12], immersing fermionic atoms into another species where standard evaporative cooling

¹The recoil energy is the energy acquired by a trapped atom after emitting a lattice photon, see chapter 2.

techniques are possible. Although sympathetic cooling is typically less efficient than multi-spin evaporation, it provides an important idea that is the controlled coupling of the system to an external bath which plays a vital role throughout this thesis as we discuss briefly in section 1.3.

Furthermore, these periodic structures can present a wide range of geometries depending on the beam alignments which increase the flexibility of these experiments; it is also possible to modify the lattice depth (and so modifying the tunneling amplitude) and to create local offsets on demand (using digital-micromirror-devices, see [25]) to implement random potentials. These random offset are relevant in fundamental condensed-matter phenomena like many-body localization (MBL) [26] as we will discuss in depth in chapter 7.

Finally, in the recent years an enormous advance in the resolution of cold atom experiments led to the development of quantum gas microscopes, both in bosonic [27, 28] and later in fermionic experiments [29, 30, 31, 32, 33, 34]. These experiments allow for single-atom resolution and addressing and, consequently, giving access to the study of the dynamics of individual atoms. As a result, not only collective signatures of the dynamics can be observed but also theoretical predictions for few-atom systems can now be benchmarked in the experiment.

1.2 Numerical methods in quantum many-body systems

The focus of this thesis is the study of dynamical and static properties of cold atomic systems. When studying quantum many-body systems we typically have to perform computations on Hilbert spaces with a prohibitive number of elements. In certain circumstances, we can make use of analytical or semi-analytical approximations that simplify the problem greatly. However, in general we need to tackle the complicated task of manipulating or diagonalizing exponentially large Hamiltonians.

This problem arises due to the quantum nature of the systems we study, since the superposition principle allows for an exponential number of state configurations even for reduced system sizes (a few atoms). In general, if we consider a set of N 2-level atoms (e.g. two hyperfine states of a neutral atomic species or any other implementation of a qubit) the possible state configurations will scale as 2^N . If we consider the storage of the Hamiltonian associated to such a system this task becomes quickly impossible. In particular, if we consider $N = 4$ we only require to store the complex coefficients associated to $2^4 = 16$ states that compose the total Hilbert space \mathcal{H} , however, for the case of $N = 300$ atoms we would require to store a matrix of approximately 10^{82} GB using double precision that is not only extremely large and impractical but it is also larger than the estimated number of barionic particles in the observable universe ($\sim 10^{80}$).

Even though the size of the Hilbert Space is a complex bottleneck for our calculations, in many cases, we will have certain symmetries of the system that we can exploit. A relevant example that we implement in this thesis is particle number conservation (see chapter 6 and 7). We can take advantage of this symmetry in two different ways: reducing the representation to the particle sector we are interested in (e.g. for N atoms in a lattice of length M described by the Hubbard model, $\dim(\mathcal{H}_N) = \frac{M!}{N!(M-N)!}$ for an individual particle sector, in contrast with the total Hilbert space $\dim(\mathcal{H}) = \sum_N \dim(\mathcal{H}_N)$); secondly, even if several particle sectors are relevant we can exploit the block-diagonal form of the Hamiltonian to consider every sector simultaneously. Nevertheless, even given a set of conserved quantities in the system, at certain sizes (tens of atoms), the dimension of every sector will grow exponentially and eventually become impractical to store.

As a result, it is crucial to find approximate methods that capture the most relevant features of these cold atomic systems with moderate computational costs. This is the case of the density matrix renormalization group (DMRG), introduced by S. R. White [35, 36] for the calculation of ground states of large one-dimensional systems. It was later shown that these ground states are represented by so-called matrix product states (MPS) (see [37, 38]). MPS form the basis of the main approximate methods included in this thesis, not only for ground state calculations but also for time-

dependent algorithms (t-DMRG) as introduced by Vidal [39, 40, 41]. These methods provide an efficient truncation of the Hilbert Space based on the amount of bipartite entanglement in the system. As a result, they provide accurate representation for low excited states in one-dimensional systems with gapped Hamiltonians. Later on, extensions to higher dimensions (see [42]) have been developed, finding moderate success in representing the Hilbert Space of the quantum many-body problems in 2D and 3D.

Finally, it is important to consider that beyond the complexity of the pure states systems that we study, in practice they are also subject to some kind of coupling to their environment. The problem of dynamics of open quantum systems is again quite complex. Nevertheless, the existence of well-understood microscopic models and well-controlled approximations in these systems allows for the derivation of equations of motion for the open problem such as master equations [43] or quantum stochastic Schrödinger equation [44]. This is possible due to the existence of a well-defined hierarchy of timescales in the system and environment. Moreover, successful stochastic approaches to map the master equation evolution have been developed throughout the years [45, 46, 47, 48], usually denoted as quantum trajectories. This approach consist on an average of pure state trajectories that map the evolution of the density operator. This method is compatible not only with exact methods but also with MPS approaches, using standard t-DMRG techniques to compute the evolution of every individual trajectory.

1.3 Open systems: Reservoir Engineering

The fact that AMO systems are coupled to their environment poses certain challenges to our ability to describe such systems, but it also provides a new means of controlling and probing cold atomic systems. In particular, the modeling and control of dissipation in AMO systems is not only fundamentally important as it tackles questions such as the understanding of decoherence or the back-action in the system due to the environment; but also, necessary for a complete description of the realistic experimental conditions, but also it provides a useful toolbox for the engineering of quantum many-body states.

This is usually referred to as reservoir engineering [49], and the main idea is based on the tuning of the coupling between the system and environment in such a way that the desired state becomes the stationary state of the open system dynamics, using the environment as a mean to reduce the entropy in the system. This concept was imported to AMO systems from Quantum Optics, where important developments in these directions were widely used for many years. Relevant examples are optical pumping [50] and laser cooling [9] which are commonly applied in experimental atomic physics.

Another important example now in the context of cold atoms is the case of sympathetic cooling [12] where an atomic species (typically harder to cool to physically relevant temperatures) is immersed into another atomic species that is cooled down into a BEC state. The second species, usually referred as reservoir gas, acts as a $T = 0^2$ bath that cools the other species to the lowest Bloch bands by emitting Bogoliubov excitations into the reservoir. We can compare its role with the one of the background radiation field in Quantum Optics. More refined examples in cold atoms combine this with ideas of dark-state driving [52, 53] to improve the cooling schemes, even within the lowest Bloch band [54, 55].

Furthermore, the coupling to the environment can be used beyond cooling schemes to create relevant states in the optical lattice such as entangled states [56, 57, 58] potentially useful for quantum enhanced metrology (see [6, 59]) or topologically protected states [60, 61]. All of these methods give access to new forms of robust state preparation in the lattice and complement the existing techniques for closed systems.

Finally, the study of dissipative dynamics of many-body systems give rise to fundamental questions beyond the practical applications we just described. Incoherent dissipative processes can substantially alter known phases of matter, even generating new ones [62, 63]. In the recent years, a new field has appeared focused on the

²Since $k_B T_{BEC} \ll \Delta E$ with ΔE the energy separation between Bloch bands, see [51].

non-equilibrium critical behaviour of such open systems and analyzing the emergence of new universality classes in driven-dissipative scenarios, see [64, 65].

1.4 Thesis Outline

In this section we describe the structure of the thesis, which is composed of 8 chapters that we can group in three different parts. The first part consists of the overview of the background material related to cold atom systems, to contextualize the discussion of the research results of this thesis. The second part is dedicated to the main numerical techniques used to obtain the research results, including exact (chapters 3) and approximate (chapter 4) methods. Finally, in the last part we will describe the three research projects (chapters 5-7) that compose the results for this thesis. Additionally, we include a conclusion (chapter 8) at the end of the thesis where we provide some final remarks.

More specifically, in chapter 2 we describe in depth the fundamental physics associated with cold atom systems. In particular, we focus on cold atoms in optical lattices, studying the coupling with the laser field and the band structure arising from the periodicity of the system, deriving the Hubbard and Bose-Hubbard models from first principles and discussing the well-controlled approximations that were made to derive those. Furthermore, we emphasize on how these systems couple to their environment and how this can be described and exploited systematically. In particular, we describe the concept of sympathetic cooling that plays a vital role in the cooling of fermionic atoms in optical lattices (see chapter 5).

In chapter 3, we introduce the numerical tools required to compute the time evolution of quantum many-body systems. In particular, we distinguish between: (i) the closed system scenario where we present methods for the exact diagonalisation of the Hamiltonian represented in the entire Hilbert Space; (ii) and open system dynamics where we derive the master equation describing the evolution of the system density operator. Also, we map the open system evolution to a stochastic sampling of quantum trajectories.

In chapter 4, we extend the ideas of chapter 3 to matrix product states (MPS) that provide a representation of the state in an efficiently truncated Hilbert Space. We describe the main routines for calculations of dynamical and equilibrium observables in the language of MPS, linking again to closed and open quantum systems.

In chapter 5, we describe the first of the original research contributions included in the thesis. The project is based on the concept of reservoir engineering to prepare useful states towards metrology. We present a stroboscopic scheme, combining coherent and dissipative driving, to prepare spin-entangled states with fermions. Moreover, we introduce the notion of Quantum Fisher Information (QFI), a metrological quantity to characterize the utility of the proposed scheme. We provide numerical simulations of the time evolution of the QFI as the stroboscopic scheme is iterated testing its robustness against spatial imperfections such as the presence of a field gradient. Finally, we analyze the results obtained and discuss some possible future directions for the project.

In chapter 6, we present the result derived from the project that analyses the role of particle statistics in the presence of single-particle loss in the optical lattice. First, we discuss the differences of hard-core bosons and spinless fermions that we can formalize through a Jordan-Wigner transformation, highlighting the non-local character of losses in the fermionic case. Then, we present a refined algorithm using number-conserving codes, introduced in chapter 4, to compute the dynamics of the system. We consider the differences arising from distinct particle statistics in the presence of both deterministic and stochastic particle loss. Finally, we describe our finding and link the results to the results of chapter 7 and to possible new directions to investigate in the future.

In chapter 7, we discuss a second research project related to single particle-loss. However, this time we focus on its role in many-body-localization. In particular, we analyze the interplay between interaction, particle loss and dephasing in the system and study relevant quantities such as the odd-even imbalance (relevant for experiments) or the entanglement entropy. Finally, we link the results to some of the findings in chapter 6 and propose interesting new directions.

To conclude, in chapter 8, we briefly describe the main findings that are included in this thesis and its relevance in the context of quantum many-body physics.

1.5 Publications during PhD

1. Evert P. L. van Nieuwenburg, Jorge Yago Malo, Andrew J. Daley, Mark H. Fischer, *Dynamics of many-body localization in the presence of particle loss*, Quantum Science and Technology 3 (1), 01LT02 (2017).

The author of this thesis performed the quantum-trajectory calculations included in this publication. This is described in chapter 7.

2. Jorge Yago Malo, Evert P. L. van Nieuwenburg, Mark H. Fischer, Andrew J. Daley, *Particle statistics and lossy dynamics of ultracold atoms in optical lattices*, Physical Review A 97 (5), 053614 (2018).

The author of this thesis performed the calculations, produced the plots and wrote most of the manuscript text for this publication. This is described in chapter 6.

3. Jorge Yago Malo, Suzanne McEndoo, Ana M. Rey, Andrew J. Daley, *Dissipative preparation of spin-entangled states with ultracold fermions in optical lattices*, in preparation.

To be submitted to Physical Review Letters, 2018. This is described in chapter 5.

Conference talk presentations

1. Young Atom Opticians (YAO) conference, February 2016, Max Planck Institute of Quantum Optics, Garching, Germany.
2. First UQUAM Topical Workshop on Open Quantum Systems, April 2016, Weizmann Institute of Science, Rehovot, Israel.
3. Symposium on Quantum Information, Simulation and Metrology, June 2016, University of Strathclyde, UK.
4. Numerical methods for Quantum Optics QUINFOG, January 2017, Madrid, Spain
5. QuProCS III workshop, March 2018, Oxford, UK.

Chapter 2

Cold Atoms in Optical Lattices

2.1 Introduction

In this chapter we provide the fundamental description of cold atom system coupled to laser fields that allows us to derive the many-body Hamiltonians, i.e. Hubbard models, that we study throughout the results of this thesis.

In particular, in section 2.2 we discuss the atom-light interaction from a semiclassical approach, introducing the important AC Stark shift; in section 2.3 we describe inter-atomic interaction through scattering theory and how scattering properties can be modified by external fields. Finally, in section 2.4 we use the previous models to derive the many-body Hamiltonian for bosonic and fermionic atoms in an optical lattice. Additionally, we introduce the Jordan-Wigner transformation, a mapping between fermionic and spin operators of this model that we extensively use in this thesis.

2.2 Atom-light interaction

In this section, we provide a brief overview of the atom-light interaction and how this can be used to trap neutral atoms in periodic potentials formed by laser light, so-called optical lattices. For a more detailed discussion, see [66, 67].

We consider the coupling of the atom and the light field via the dipole-approximation to describe the coupling Hamiltonian given by

$$\hat{H} = -\mathbf{d}(\mathbf{r}, t) \cdot \mathbf{E}(\mathbf{r}, t), \quad (2.1)$$

with \mathbf{d} the dipole moment of the atom and \mathbf{E} is the electric field associated with the laser light that we can express as

$$\mathbf{E}(\mathbf{r}, t) = [E_0(\mathbf{r}) \mathbf{p} \exp(-i\omega_{\text{opt}}t) + \text{c.c.}] , \quad (2.2)$$

where E_0 contains the spatial dependence of the field, \mathbf{p} is the polarization vector and ω_{opt} is the laser frequency. For a weak driving, the dipole moment acquires the same frequency and can be written as

$$\mathbf{d}(\mathbf{r}, t) = [\mathbf{d}_0(\mathbf{r}) \exp(-i\omega_{\text{opt}}t + \varphi) + \text{c.c.}] , \quad (2.3)$$

with φ a given phase.

Let us consider now the spectrum of the atomic Hamiltonian given by the set of states $\{|n\rangle\}$ with energies E_n . Our objective is to perturbatively compute the effects of a weak field on the atomic ground state $|0\rangle$. The first term of our perturbation theory expansion is given by

$$\Delta E^{(1)}(\mathbf{r}) = -\langle 0 | \mathbf{d}_0(\mathbf{r}) \cdot E_0(\mathbf{r}) \mathbf{p} | 0 \rangle = 0. \quad (2.4)$$

This term vanishes due to the eigenstates parity. Therefore, we require to study the second order terms

$$\Delta E^{(2)}(\mathbf{r}) = \alpha(\omega_{\text{opt}}) |E_0(\mathbf{r})|^2. \quad (2.5)$$

where $\alpha(\omega_{\text{opt}})$ is denoted as the dynamic polarizability and is given by

$$\alpha(\omega_{\text{opt}}) = \sum_{n=1} |\langle 0 | \mathbf{d}_0(\mathbf{r}) \cdot \mathbf{p} | n \rangle|^2 \left(\frac{1}{E_0 - E_n + \hbar\omega_{\text{opt}}} + \frac{1}{E_0 - E_n - \hbar\omega_{\text{opt}}} \right). \quad (2.6)$$

This second order term accounts for the interaction of the ground state with an excited state together with the emission or the absorption of a photon of frequency ω_{opt} . From Eq.(2.5) we observe that the energy of the ground state is modified according to the intensity of the laser field; this is known as the AC Stark shift and will play a vital role in our ability to trap neutral atoms.

The most interesting scenario occurs when the laser frequency ω_{opt} is in the vicinity of an atomic transition between the ground state $|0\rangle \equiv |g\rangle$ and an excited state $|n_0\rangle \equiv |e\rangle$. Then, we can restrict our description to these two levels and define the transition frequency from

$$\hbar\omega_{\text{eg}} = E_e - E_g. \quad (2.7)$$

From Eq.(2.6) we observe that for energies close to the transition, the second term in the sum, with a much smaller denominator $E_0 - E_n - \hbar\omega_{\text{opt}}$, will have a much larger contribution. Then, we can write the polarizability as

$$\alpha(\omega_{\text{opt}}) = \frac{1}{\hbar\Delta} |\langle g | \mathbf{d}_0(\mathbf{r}) \cdot \mathbf{p} | e \rangle|^2. \quad (2.8)$$

where $\Delta = \omega_{\text{opt}} - \omega_{\text{eg}}$ is the laser detuning. We can also define the Rabi frequency as

$$\Omega_0(\mathbf{r}) = 2\langle g | \mathbf{d}_0(\mathbf{r}) \cdot \mathbf{p} E_0(\mathbf{r}) | e \rangle / \hbar. \quad (2.9)$$

And, consequently,

$$\Delta E^{(2)}(\mathbf{r}) = \frac{\hbar |\Omega_0(\mathbf{r})|^2}{4\Delta}. \quad (2.10)$$

All in all, we can describe the energy shift of the ground state energy due to the presence of the laser field by two parameters. Moreover, the energy change is proportional to the intensity of the field (AC Stark Shift). Thus, a neutral atom in the presence of the laser field experiences an optical potential

$$V_{\text{opt}}(\mathbf{r}) \propto \frac{I(\mathbf{r})}{\Delta}. \quad (2.11)$$

This effect constitutes one of the foundations of the optical trapping and manipulation of neutral atoms. Moreover, we observe that by changing the sign of the detuning Δ we can change the behaviour of the atoms. For a blue-detuned laser ($\Delta > 0$) neutral atoms will be repelled by the intensity maxima, while for a red-detuned one ($\Delta < 0$) intensity maxima will attract the atoms.

Finally, if several laser beams are combined a wide variety of optical periodic potentials can be created. In particular, using counter-propagating beams with identical polarization and frequency we can create a standing wave potential given by

$$V_{\text{opt}}(x) = V_0 \sin^2(k_L x) \quad (2.12)$$

with V_0 the lattice depth, $k_L = 2\pi/\lambda$ the laser field wavenumber and λ the laser wavelength. We can create higher dimensional lattices by intersecting beams in the other orthogonal directions. Moreover, changing the alignment of the beams and their polarization gives rise to interesting geometries in the periodic potentials, substantially increasing the experimental possibilities.

2.3 Atom-atom interaction

In this section we provide the model to describe inter-atomic interaction in the cold atom gas in an optical lattice. In particular, we will describe it through low-energy scattering theory justified by the low temperatures of optical lattices experiments. Moreover, we will consider a dilute gas so that we can restrict our treatment to two-body interactions (this is discussed in section 2.4).

We can define the two-body scattering Hamiltonian in the relative center of mass as

$$\hat{H}_{\text{scat}} = \frac{p^2}{2\mu} + V(r), \quad (2.13)$$

with $\mu = m/2$ the relative mass for two atoms of mass m and $V(r)$ the interaction potential. The eigenstates of the Hamiltonian in the far-field (implying that $r \gg b$ with b the effective interaction range of the potential, see [68]) are given by

$$\phi_{\mathbf{k}}(\mathbf{r}) = e^{i\mathbf{k}\cdot\mathbf{r}} + f(\mathbf{k}, \mathbf{n}) e^{i\mathbf{k}\cdot\mathbf{r}}/r, \quad (2.14)$$

with the direction vector $\mathbf{n} = \mathbf{r}/r$ and the scattering amplitude

$$f(\mathbf{k}, \mathbf{n}) = -\frac{\mu}{2\pi\hbar^2} \int d\mathbf{r}' e^{-i\mathbf{k}\cdot\mathbf{r}'} V(\mathbf{r}') \phi_{\mathbf{k}}(\mathbf{r}'). \quad (2.15)$$

The scattering amplitude can be subject to certain approximations that will lead to its description by a single free parameter, the scattering length a_S . First, if we assume that we are in the low-energy regime, i.e. $k \ll b^{-1}$, we can restrict the scattering to s-wave and so our scattering amplitude becomes independent of the direction \mathbf{n} (spherical symmetry). The second approximation is to assume weak-interaction ($a_S \ll k^{-1}$). If both conditions are met, we can approximate our scattering amplitude as¹

$$f(\mathbf{k}, \mathbf{n}) = -\frac{1}{(1/a_S) + ik}. \quad (2.16)$$

In the general many-body problem, using a second-quantized description, we can describe the inter-particle interaction by a coupling constant depending only on a_S ,

$$g = 4\pi\hbar^2 a_S/m. \quad (2.17)$$

More importantly, we can not only describe the interaction properties by a single parameter but also tune it experimentally with great precision. In particular, the scattering length can be modified by the use of Feshbach resonances. These resonances occur by the coupling of atoms into bound molecular states which possess substantially different scattering properties and these can be externally controlled by, for example, a magnetic field [70, 71]. In particular, near the resonance we can parametrize the scattering length as

$$a_S(B) = a_{S,0} \left(1 - \frac{\Delta B}{B - B_{\text{res}}} \right), \quad (2.18)$$

where $a_{S,0}$ is the scattering length in the absence of the molecular coupling, B_{res} is the resonant field value and ΔB is the resonance width.

¹For a detailed derivation, see [68, 69].

2.4 Cold atoms in optical lattices

Now that we have discussed how to model atom-light and inter-atomic interaction, we have the necessary tools to characterize the behaviour of atoms trapped in optical lattices. Describing these periodic potentials is vital since they constitute the main platform for the trapping of atoms that we will model in all of the research chapters included in this thesis (chapters 5, 6 and 7).

We can describe the many-body Hamiltonian of a cold fermionic or bosonic gas experiencing the optical lattice potential with lattice constant a from a microscopic second-quantized picture as

$$\begin{aligned} \hat{H} = & \sum_{\sigma} \int d^3r \hat{\Psi}_{\sigma}^{\dagger}(\mathbf{r}) \left[-\frac{\hbar^2 \nabla^2}{2m} + V(\mathbf{r}) \right] \hat{\Psi}_{\sigma}(\mathbf{r}) \\ & + \frac{g}{2} \sum_{\sigma, \sigma'} \int d^3r \hat{\Psi}_{\sigma}^{\dagger}(\mathbf{r}) \hat{\Psi}_{\sigma'}^{\dagger}(\mathbf{r}) \hat{\Psi}_{\sigma'}(\mathbf{r}) \hat{\Psi}_{\sigma}(\mathbf{r}), \end{aligned} \quad (2.19)$$

with $\hat{\Psi}_{\sigma}^{(\dagger)}(\mathbf{r})$ the fermionic/bosonic annihilation (creation) field operator of a particle with spin σ . These operators obey the corresponding fermionic or bosonic commutation rules. The first term in Eq.(2.19) describes the kinetic energy of atoms with mass m and their interaction with the external potential $V(\mathbf{r}) = V_{\text{opt}}(\mathbf{r}) + V_{\text{ext}}(\mathbf{r})$ that we can divide into the periodic 3D optical lattice potential $V_{\text{opt}}(\mathbf{r}) = \sum_{i=x,y,z} V_{0,i} \sin^2(k_L^i i)$ and some additional external fields $V_{\text{ext}}(\mathbf{r})$ (e.g., trapping field in an experiment.). The second term in Eq.(2.19) accounts for the inter-particle interaction with interaction constant $g = 4\pi\hbar^2 a_S/m$ [68].

We can consider now the expansion of the field operator $\hat{\Psi}_{\sigma}(\mathbf{r})$ in terms of the Wannier functions [72, 73]

$$\hat{\Psi}_{\sigma}(\mathbf{r}) = \sum_{n,j,\sigma} w^{[n]}(x - x_{i_x}) w^{[n]}(y - y_{i_y}) w^{[n]}(z - z_{i_z}) \hat{a}_{j,\sigma}, \quad (2.20)$$

with $w^{[n]}$ the Wannier function associated to the n -th Bloch band and $\hat{a}_{j,\sigma}$ is the annihilation operator on site j with coordinates $\mathbf{j} \equiv (x_{j_x}, y_{j_y}, z_{j_z})$, i.e. the location

of the j -th lattice potential minimum. The Wannier functions form an orthonormal basis that describe single-particle wavefunctions that are localized around a lattice site. They are obtained as a transformation of the Bloch functions basis [74]

$$w^{[n]}(x - x_{jx}) = \sqrt{\frac{a}{2\pi}} \int_{-\pi/a}^{\pi/a} dq \phi_q^{[n]}(x) e^{-iqx_{jx}}, \quad (2.21)$$

and similarly for y and z directions. Here, $\phi_q^{[n]} = e^{iqx} u_q^{[n]}(x)$ with $u_q^{[n]}(x)$ the Bloch functions, which possess the same periodicity as $V_{\text{opt}}(\mathbf{r})$, and q the quasi-momentum in the first Brillouin zone $(-\pi/a, \pi/a]$.

We can apply this transformation to Eq.(2.19) to obtain the general multi-band Hamiltonian \hat{H}

$$\hat{H} = - \sum_{\substack{i,j,\sigma \\ m,n}} J_{i,j}^{m,n} \hat{a}_{i\sigma}^{[m]\dagger} \hat{a}_{j\sigma}^{[n]} + \sum_{\substack{i,j,k,l,\sigma,\sigma' \\ m,n,p,q}} U_{i,j,k,l}^{m,n,p,q} \hat{a}_{i\sigma}^{[m]\dagger} \hat{a}_{j\sigma'}^{[n]\dagger} \hat{a}_{k\sigma}^{[p]} \hat{a}_{l\sigma}^{[q]} + \sum_{\substack{i,\sigma \\ m,n}} \epsilon_i^{m,n} \hat{a}_{i\sigma}^{[m]\dagger} \hat{a}_{i\sigma}^{[n]}, \quad (2.22)$$

where the corresponding constants for tunneling, interaction and local offset are respectively given by

$$J_{i,j}^{m,n} = \int d^3r w^{[m]*}(\mathbf{r} - \mathbf{r}_i) \left[-\frac{\hbar^2 \nabla^2}{2m} + V_{\text{opt}}(\mathbf{r}) \right] w^{[n]}(\mathbf{r} - \mathbf{r}_j), \quad (2.23)$$

$$U_{i,j,k,l}^{m,n,p,q} = \frac{g}{2} \int d^3r w^{[m]*}(\mathbf{r} - \mathbf{r}_i) w^{[n]*}(\mathbf{r} - \mathbf{r}_j) w^{[p]}(\mathbf{r} - \mathbf{r}_k) w^{[q]}(\mathbf{r} - \mathbf{r}_l), \quad (2.24)$$

$$\epsilon_i^{m,n} = \int d^3r w^{[m]*}(\mathbf{r} - \mathbf{r}_i) V_{\text{ext}}(\mathbf{r}) w^{[n]}(\mathbf{r} - \mathbf{r}_i). \quad (2.25)$$

This Hamiltonian contains a large number of terms, however, in practice there are certain well-controlled approximations that will significantly simplify this Hamiltonian. On top of these approximations, we will focus on the case of one-dimensional lattices as it is the case of the numerical studies throughout this thesis. Quasi-1D systems can be experimentally realized by tightly confining the atoms along two directions such that $V_{0,y} = V_{0,z} = V_{0,\perp} \gg V_{0,x} = V_0$.

Now, let us consider the first approximation which is to assume that atoms will

only populate the lower Bloch band, this is true if all energy scales (temperature, tunneling and onsite-interaction constants) are smaller than the energy associated to the band separation given by the trapping frequency $\hbar\omega_T$. Then, we can restrict to a one-dimensional single-band Hamiltonian described in terms of $w^{[0]}(x)$. Furthermore, we can consider that the lattice is deep enough so that the tunneling amplitude is only relevant for nearest-neighbours and so that we can approximate any other longer-range tunneling term to zero; similarly, for inter-atomic interactions where only onsite interactions are not negligible. Finally, we consider that the temperature is low enough so that inter-particle interaction are two-body² and can be described through low-energy s-wave scattering theory, as we discussed in section 2.3.

After taking this set of approximations we obtain

$$\hat{H} = -J \sum_{\langle ij \rangle, \sigma} \hat{a}_{i\sigma}^\dagger \hat{a}_{j,\sigma} + U \sum_{i,\sigma} \hat{a}_{i,\sigma}^\dagger \hat{a}_{i,\sigma}^\dagger \hat{a}_{i,\sigma} \hat{a}_{i,\sigma} + \sum_{i,\sigma} \epsilon_i \hat{a}_{i\sigma}^\dagger \hat{a}_{i,\sigma}, \quad (2.26)$$

with $\langle ij \rangle$ denoting a sum over nearest-neighbours, J the tunneling amplitude, U the onsite-interaction constant and ϵ_i the onsite energy offset (this term can also correspond to the chemical potential). These constants are given by

$$J = \int dx w^{[0]*}(x) \left[-\frac{\hbar^2 \nabla_x^2}{2m} + V_{\text{opt}}(\mathbf{x}) \right] w^{[0]}(x - a), \quad (2.27)$$

$$U = \frac{g}{2} \int dx |w^{[0]}(x)|^4, \quad (2.28)$$

$$\epsilon_i = \int dx V_{\text{ext}}(x) |w^{[0]}(x - x_{i_x})|^2. \quad (2.29)$$

The Hamiltonian we just derived corresponds to the Hubbard model which describes the dynamics of a dilute ultracold gas in the lowest band of an optical lattice. This Hamiltonian is the object of study of numerous theoretical and experimental efforts in the last decades. One of the main reasons is the extreme tunability of this Hamiltonian. For example, increasing the lattice depth V_0 will decrease the tunneling amplitude to neighbouring sides and also modify the onsite interaction; similarly we can modify the scattering length a_S through Feshbach resonances (as we explained in

²This requires the cold gas to be dilute, i.e. $\rho r_{aa}^3 \ll 1$ as we indicate later on in this section.

section 2.3) leading to a change in U ; in addition, the application of external fields can modify the values of ϵ_i arbitrarily (using digital-micromirror-devices, see [25]). Note that in typical experiments, the lattices are usually subject to a certain harmonic local offset $\epsilon_i \neq 0$ dependent on the experimental laser beam waist. This can be avoided by restricting the dynamics to the central region of the lattice potential.

Let us now summarize and justify the approximations that we used to derive the single-band Hubbard model:

1. The system energy scales are lower than the inter-band separation, meaning that $\hbar\omega_T \gg J, U, k_B T$ and justifying a single band model. This condition is fulfilled when the trapping potential V_0 is greater than several recoil energies $E_R = \hbar^2 k^2 / 2m$. For example, for $V_0 = 10E_R$ and optical wavelengths for the trapping we obtain that the band separation is $\omega_T \sim 100$ kHz while the tunneling $J \sim 100$ Hz and the onsite interaction $U \sim 1$ kHz.
2. The gas is dilute enough so that we can restrict to two-body interactions, implying that $\rho r_{aa}^3 \ll 1$ with $\rho = N/V$ being the atomic density in the trapped volume V and r_{aa} the range of the atom-atom interaction. In this scenario two-body collisions are unlikely enough so that three or more particle events can be neglected.
3. The temperature of the system is required to be low enough so that we can describe the two-body interactions via low-energy s-wave scattering theory. In this case, the range of the atomic interaction r_{aa} is much smaller than their thermal wavelength $\lambda_d B = 2\pi\hbar/p$ with the momentum $p \propto \sqrt{mk_B T}$. As a result, the scattering properties are characterized by a single parameter, the scattering length a_S , independently of the energy of the particles. Hence, we can rewrite condition 2. as $\rho a_S^3 \ll 1$.
4. The lattice is deep enough so that long-range tunneling or inter-site interactions can be neglected. To justify this condition one should evaluate equations (2.23) and (2.24). If we consider again the case of $V_0 = 10E_R$, then $J_{i,i+3} \sim 0.01J_{i,i+2} \sim 0.01J_{i,i+1}$ and with a similar decrease for the inter-site interactions.

2.4.1 Hubbard model

Throughout this thesis we will consider both the bosonic and fermionic cases of the Hubbard model and in some cases exploit their differences (see chapter 6). Hence, it is relevant to discuss the main features of the Hubbard (fermionic) and the Bose-Hubbard (bosonic) model.

The Hubbard model was originally derived in the context of fermionic particles, as it was the case of strongly correlated electrons [75]. This model can be directly applied to fermionic atoms in optical lattices, where we typically consider a two-spin-component mixture of fermionic atoms, i.e. $\sigma \in \{\uparrow, \downarrow\}$, in the lowest Bloch band of a lattice of length M

$$\hat{H} = -J \sum_{\langle ij \rangle, \sigma} \hat{a}_{i, \sigma}^\dagger \hat{a}_{j, \sigma} + U \sum_i \hat{n}_{i, \uparrow} \hat{n}_{i, \downarrow} + \sum_{i, \sigma} \epsilon_i \hat{n}_{i, \sigma}. \quad (2.30)$$

Here, the operator $\hat{a}_{i, \sigma}^{(\dagger)}$ creates (annihilates) a particle with spin σ in site i and $\hat{n}_{i, \sigma} = \hat{a}_{i, \sigma}^\dagger \hat{a}_{i, \sigma}$ is the number operator of spin σ in site i . These operators follow the canonical fermionic commutation rules $\{\hat{a}_{i, \sigma}, \hat{a}_{j, \sigma'}^\dagger\} = \delta_{i, j} \delta_{\sigma, \sigma'}$. Given the fermionic nature of the model, the site occupation for each spin species can only be 0 or 1. As a result, the filling factor plays an important factor in the ground state properties of the model: metallic for average lattice occupations $n = N/M < 1$ and a band insulator for $n = 1$. Even though the model can be analytically solved using the Bethe Ansatz [76] in 1D, we lack a proper analytical or numerical approach in higher dimensions to resolve the full phase diagram of the model. Even in 1D, the problem becomes numerically challenging due to the rapid growth of the Hilbert space. For example, in a lattice of length M with N_\uparrow and N_\downarrow atoms with spin \uparrow and \downarrow respectively, the dimension is given by

$$\dim(\mathcal{H}) = \frac{(M!)^2}{N_\uparrow! (M - N_\uparrow)! N_\downarrow! (M - N_\downarrow)!}. \quad (2.31)$$

Nevertheless, there are certain well-studied regimes in the phase diagram of the Hubbard model [77]. For attractive interactions we observe a BCS-BEC crossover as the interaction increases [78, 79, 80]. On the other hand, in the case of repulsive

interaction we observe antiferromagnetic ordering at low temperatures [81, 82].

In this thesis, we discuss several examples of fermionic systems including a multiple Bloch band description (chapter 5), fermionic systems subject to disorder (chapter 7) and, in general, open fermionic systems (chapters 5-7). In many of these instances, the anticommutation of fermionic operators will play an important role, e.g. giving non-local properties to single-particle loss (chapters 6-7). In the following section we formalize this anticommutation through the Jordan-Wigner (J-W) transformation.

2.4.1.1 Jordan-Wigner transformation

In this section, we apply the J-W transformation [83] to the Hubbard model as a means to systematically account for all the signs arising from the fermionic anti-commutation. This transformation will be used explicitly in chapters 6 and 7 to describe single-particle loss. The J-W transformation is a well-established technique that allows for the mapping of fermionic systems into spin operators or vice-versa. Please note that here we define the transformation restricting to 1D.

In order to define this transformation we need to choose an order convention for our state description, we select the lattice ordering

$$\hat{a}_{1,\uparrow}^\dagger \hat{a}_{2,\uparrow}^\dagger \dots \hat{a}_{M,\uparrow}^\dagger \hat{a}_{1,\downarrow}^\dagger \hat{a}_{2,\downarrow}^\dagger \dots \hat{a}_{M,\downarrow}^\dagger |vac\rangle \quad (2.32)$$

with $|vac\rangle$ the vacuum state. From this choice, the transformation is defined as

$$\hat{a}_{l,\sigma}^{(\dagger)} = \exp\left(\mp i\pi \sum_{j<l} \hat{s}_{j,\sigma}^+ \hat{s}_{j,\sigma}\right) \hat{s}_{l,\sigma}^{-(+)} ; \quad \hat{s}_{l,\sigma}^{-(+)} = \exp\left(\pm i\pi \sum_{j<l} \hat{a}_{j,\sigma}^\dagger \hat{a}_{j,\sigma}\right) \hat{a}_{l,\sigma}^{(\dagger)}, \quad (2.33)$$

and, consequently a string operator is associated with every spin operator

$$\hat{a}_{l,\sigma}^{(\dagger)} \rightarrow (-1)^{\theta_l} \hat{s}_{l,\sigma}^{-(+)}, \quad (2.34)$$

where we define the phase factor as $\theta_l = \sum_{i<l} \hat{s}_{a,j}^+ \hat{s}_{a,j} = \sum_{i<l} \hat{n}_{i,\sigma}$. The spin operators obey the fermionic commutation relation for a given site and the bosonic

commutation rules for different sites:

$$\begin{aligned} \{\hat{s}_{\alpha,\sigma}^{-(+)}, \hat{s}_{\alpha,\sigma}^{-(+)}\} &= 0; \{\hat{s}_{\alpha,\sigma}, \hat{s}_{\alpha,\sigma}^+\} = 1; \\ [\hat{s}_{\alpha,\sigma}^{-(+)}, \hat{s}_{\beta,\sigma}^{-(+)}] &= 0; [\hat{s}_{\alpha,\sigma}, \hat{s}_{\beta,\sigma}^+] = 1. \end{aligned} \quad (2.35)$$

We can apply the transformation to Eq.(2.30) to obtain

$$\hat{H} = -J \sum_{\langle ij \rangle, \sigma} \hat{s}_{i,\sigma}^+ \hat{s}_{j,\sigma} + U \sum_i^M \hat{s}_{i,\uparrow}^+ \hat{s}_{i,\downarrow}^+ \hat{s}_{i,\downarrow} \hat{s}_{i,\uparrow} + \sum_{i,\sigma}^M \epsilon_i \hat{s}_{i,\sigma}^+ \hat{s}_{i,\sigma}. \quad (2.36)$$

We observe that crucially all phases vanish for the single-band Hubbard model in 1D. For the onsite-interaction and onsite-energy terms this can be immediately understood as they are quadratic in $\hat{a}_{i,\sigma}, \hat{a}_{i,\sigma}^\dagger$ and so they are proportional to $(-1)^{2\theta_i} = 1$. For the tunneling terms, all phases disappear if only first neighbours are included, for example, we can consider $\hat{a}_{i,\sigma}^\dagger \hat{a}_{i+1,\sigma} = (-1)^{\theta_i} \hat{s}_{i,\sigma}^+ (-1)^{\theta_{i+1}} \hat{s}_{i+1,\sigma} = \hat{s}_{i,\sigma}^+ (-1)^{\hat{n}_{i,\sigma}} \hat{s}_{i+1,\sigma} = \hat{s}_{i,\sigma}^+ \hat{s}_{i+1,\sigma}$ since Pauli exclusion principle requires $\hat{n}_{i,\sigma} = 0$ for this tunneling element to be non-zero ($(\hat{a}_{i,\sigma}^\dagger)^2 \equiv 0$).

However, more generic terms, such as, the case of single-particle loss given by $\hat{a}_{i,\sigma} = (-1)^{\sum_{i < l} \hat{n}_{i,\sigma}} \hat{s}_{i,\sigma}$, do have a non-vanishing string operator associated to them. Other relevant examples are long-range tunneling (where the sign depends on the occupation in the intermediate sites), inter-band tunneling processes or particle injection terms. In the presence of this type of terms, the use of the J-W transformation allows for the systematic bookkeeping of all the corresponding signs and simplifies notably our calculations. Moreover, this representation will simplify in great degree the use of symmetry-preserving numerical techniques in section 4.1.6 that we then apply to the calculations in chapters 6 and 7.

2.4.2 Bose-Hubbard model

A single-species ultracold bosonic gas trapped in an optical lattice can be described through the Bose-Hubbard Hamiltonian

$$\hat{H} = -J \sum_{\langle ij \rangle} \hat{b}_i^\dagger \hat{b}_j + U \sum_i^M \hat{n}_i (\hat{n}_i - 1) - \mu \sum_i^M \hat{n}_i. \quad (2.37)$$

Here, the operator $\hat{b}_i^{(\dagger)}$ creates (annihilates) a bosonic particle in site i and $\hat{n}_i = \hat{b}_i^\dagger \hat{b}_i$ is the number operator in site i . These operators follow the canonical bosonic commutation rules $[\hat{b}_i, \hat{b}_j^\dagger] = \delta_{i,j}$. In this model the addition of $\epsilon_i = \mu (\forall i)$, with μ the chemical potential, guarantees a well-defined fixed particle number in the system. Similarly, to the Hubbard model, the dimension of the Hilbert Space grows rapidly. In particular, in a lattice of length M with N atoms

$$\dim(\mathcal{H}) = \frac{(N + M - 1)!}{N!(M - 1)!}. \quad (2.38)$$

Moreover, as cooling techniques of bosonic atoms in optical lattices have proven to be less demanding experimentally, the implementation of the Bose-Hubbard model, and the observation of its quantum phase transition [19] from a Mott insulator (MI) into a superfluid (SF) phase, set one of the first milestones in the field of quantum simulation with cold atomic gases [7]. These two phases, which are the ground states of the Bose-Hubbard model for different regimes of the ratio U/J , have substantially different properties.

On the one hand, in the case of $U/J \rightarrow 0$ bosonic atoms are delocalized along the lattice minimizing their kinetic energy. In this case, the atoms are in the superfluid phase and the spectrum becomes gapless. Moreover, in 1D, off-diagonal single particle density matrices $\langle \hat{b}_i \hat{b}_{i+l}^\dagger \rangle$ decay polynomially with the lattice distance l . The SF state is given by

$$|\psi_{\text{SF}}\rangle \propto \left(\frac{1}{M} \sum_{i=1}^M \hat{b}_i^\dagger \right)^N |vac\rangle \quad (U/J \rightarrow 0). \quad (2.39)$$

In the limit of $M, N \rightarrow \infty$, with N/M fixed, the state exhibits Poisson statistics and approaches a coherent state

$$|\psi_{\text{SF}}\rangle \propto \prod_{i=1}^M \exp\left(\sqrt{\frac{N}{M}} \hat{b}_i^\dagger\right) |vac\rangle. \quad (2.40)$$

On the other hand, in the limit of $J/U \rightarrow 0$ on-site interactions reduce the probability of tunneling events. In the commensurate filling regime ($N = M$), the most energetically favourable occupation for every lattice site is the average filling $n = N/M$ and all particles become exponentially localized. The spectrum of the system exhibits a finite gap $\Delta = U$. In the MI phase single-particle density matrix elements decay exponentially with the lattice distance. The MI state is given by

$$|\psi_{\text{MI}}\rangle = \prod_{i=1}^M (\hat{b}_i^\dagger)^n |vac\rangle. \quad (2.41)$$

There has been an extensive theoretical effort over the last decades to characterize this phase transition beyond the two limits we just discussed. The difficulty of it arises from the fact that the problem cannot be solved analytically beyond the case of an integer average filling factor n via mean-field theory [84]. For 1D, the critical point has been numerically predicted $(U/J)_C \approx 3.3$ via DMRG techniques [85], we will discuss this technique in chapter 4.

Chapter 3

Dynamics in closed and open quantum systems

3.1 Introduction

In this chapter we will briefly describe the main numerical techniques to compute the dynamics of quantum many-body systems considering the complete Hilbert Space. Due to the exponential growth of the Hilbert Space dimension with the system size, all the methods presented have a limited applicability regarding the system sizes we can describe with them. However, they will connect with the approximate techniques that we will describe in chapter 4 to describe bigger systems.

In section 3.2 we first analyze the problem of computing the dynamics of quantum systems that are isolated and describe several approaches to compute the evolution operator; while in section 3.3 we adapt the formalism to tackle systems that are subject to dissipative processes due to their coupling to their environment. In this section we derive a master equation for the system density operator.

3.2 Closed quantum systems: exact diagonalisation

First, let us describe the basics of the problem to introduce the notation that we follow. In the study of dynamics of closed quantum systems the problem reduces to the computation of the evolution of a state described by the Schrödinger equation,

$$d|\psi\rangle/dt = -i\hbar\hat{H}(t)|\psi\rangle, \quad (3.1)$$

with $\hat{H}(t)$ the time-dependent Hamiltonian of the system and $|\psi\rangle$ the state of the system. In the case of a time-independent Hamiltonian $\hat{H}(t) \equiv \hat{H}$, the state vector $|\psi(t)\rangle$ is given by

$$|\psi(t)\rangle = \hat{U}(t)|\psi(0)\rangle = e^{-i\hat{H}t}|\psi(0)\rangle, \quad (3.2)$$

where $\hat{U}(t)$ is the evolution operator. Now, we can express any state in the eigenbasis of \hat{H} , $\{|\lambda\rangle\}$, as

$$|\psi(0)\rangle = \sum_{\lambda} \alpha_{0,\lambda} |\lambda\rangle, \quad (3.3)$$

with $\alpha_{0,\lambda} = \langle\lambda|\psi(0)\rangle$ and $\hat{H}|\lambda\rangle = E_{\lambda}|\lambda\rangle$. Hence,

$$\hat{U}(t) = e^{-i\hat{H}t} = \sum_{\lambda} e^{-iE_{\lambda}t} |\lambda\rangle\langle\lambda|. \quad (3.4)$$

so that, substituting in (3.2),

$$|\psi(t)\rangle = \hat{U}(t)|\psi(0)\rangle = \sum_{\lambda} e^{-iE_{\lambda}t} |\lambda\rangle\langle\lambda|\psi(0)\rangle = \sum_{\lambda} e^{-iE_{\lambda}t} \alpha_{0,\lambda} |\lambda\rangle. \quad (3.5)$$

As a result, the computation of the evolution turns into an eigenvalue problem of the form

$$\hat{H}|\lambda\rangle = E_{\lambda}|\lambda\rangle. \quad (3.6)$$

Due to the exponential growth of the Hilbert Space, this task will quickly become numerically unaffordable as the size \hat{H} explodes.

Note, that even if we are interested in static properties, such as ground state properties, we will in general still require to diagonalize the Hamiltonian: either to find the spectrum minimum or to use imaginary-time evolution (see section 4.3.1 where we apply this technique in the context of matrix product states).

3.2.1 Numerical tools for exact diagonalisation

In general, the main strategies to overcome the diagonalization task rely on a certain form of time discretization of the evolution or exponentiation of \hat{H} ; this implies that the evolution of the state gains a stroboscopic character where approximate forms of the evolution operator are applied in intervals of length Δt . Within this approach we can consider two different ways to tackle the problem, namely explicit or implicit methods. The former is the simplest of them and relies on the explicit computation of the state after a timestep $|\psi(t + \Delta t)\rangle$ from the known state vector $|\psi(t)\rangle$ at time t :

$$|\psi(t + \Delta t)\rangle = (I - i\hat{H}\Delta t) |\psi(t)\rangle + \mathcal{O}(\Delta t^2). \quad (3.7)$$

However, this, so-called Euler method [86] is not the most stable due to the large timestep error and the fact that the evolution operator applied is not unitary. Consequently, we require the state to be renormalized in every step. We can refine this technique by combining it with implicit algorithms using the Crank-Nicholson method [86]:

$$|\psi(t + \Delta t)\rangle = \frac{(I - i\hat{H}\Delta t/2)}{(1 + i\hat{H}\Delta t/2)} |\psi(t)\rangle + \mathcal{O}(\Delta t^2). \quad (3.8)$$

This expression, which is norm-preserving, arises from a subdivision of the evolution into an intermediate step with:

$$\begin{cases} |\psi(t + \Delta t/2)\rangle = (I - i\hat{H}\Delta t/2) |\psi(t)\rangle + \mathcal{O}(\Delta t^2), \\ |\psi(t + \Delta t/2)\rangle = (I + i\hat{H}\Delta t/2) |\psi(t + \Delta t)\rangle + \mathcal{O}(\Delta t^2), \end{cases} \quad (3.9)$$

where we have computed the intermediate state vector $|\psi(t + \Delta t/2)\rangle$ from a forward and backward time evolution. It might seem that for this method to be practical we require to know in advance the evolved state $|\psi(t + \Delta t)\rangle$. However, we can iteratively solve the first part of Eq.(3.9) for the intermediate step and then consider that $|\psi(t + \Delta t/2)\rangle = (|\psi(t)\rangle + |\psi(t + \Delta t)\rangle) / 2$ to obtain the evolved state as:

$$|\psi(t + \Delta t)\rangle = 2|\psi(t + \Delta t/2)\rangle - |\psi(t)\rangle + \mathcal{O}(\Delta t^2). \quad (3.10)$$

This method has a better robustness and scaling with the timestep truncation than the Euler method.

Furthermore, there are numerous generalizations of these methods to higher orders. A relevant example is the popular 4th-order Runge-Kutta method [86]. Moreover, there are two particular examples that it is worth mentioning as they have both been an essential part in the diagonalisation routines used to produce the results of this thesis, namely Krylov subspaces and Trotter expansions.

1. *Krylov subspace expansion*: the first of the methods relies on a decomposition of the time evolution consisting on a Taylor expansion of the evolution operator. Given the evolution operator, we can expand it as

$$\hat{U}(t) = e^{-i\hat{H}t} = I + (-i\hat{H}t) + \frac{(-i\hat{H}t)^2}{2!} + \dots, \quad (3.11)$$

and so,

$$|\psi(t)\rangle = \hat{U}(t)|\psi(0)\rangle = |\psi(0)\rangle + (-i\hat{H}t)|\psi(0)\rangle + \frac{(-i\hat{H}t)^2}{2!}|\psi(0)\rangle + \dots \quad (3.12)$$

Thus, for a expansion of k -th order our evolved state can be spanned by a basis of so-called Krylov subspace given by $\{|\psi\rangle, \hat{H}t|\psi\rangle, \dots, (\hat{H}t)^k |\psi\rangle\}$:

$$|\psi(t)\rangle = |\psi(0)\rangle + a_1 (\hat{H}t) |\psi(0)\rangle + a_2 (\hat{H}t)^2 |\psi(0)\rangle + \dots + a_k (\hat{H}t)^k |\psi(0)\rangle + \mathcal{O}(t^{k+1}). \quad (3.13)$$

This method is based on the idea that the Taylor coefficient may not be the best set of $\{a_k\}$ to represent the evolved state. Thus, this method search for

the optimal linear combination in the Krylov subspace to represent $|\psi(t)\rangle$. Efficient implementations of this method rely on a representation of the subspace elements on an orthonormal basis (see discussion on Arnoldi and Lanczos processes in [87]). Typically for sparse matrices, Krylov methods require k values much smaller than the dimension of \mathcal{H} where $|\psi(t)\rangle$ and $U(t)$ are represented.

In addition, this technique constitutes the essential ingredient for the standard routines used in MATLAB for matrix diagonalisation and the computation of time evolution (extensive details can be found in [88]). This plays a vital role in the calculations for small systems in chapters 5, 6 and 7.

2. *Suzuki-Trotter decomposition*: the second method we mentioned is the Suzuki-Trotter decomposition¹. The main idea of the algorithm is to decompose the evolution operator into local operators that describe the Hamiltonian acting on a reduced number of sites. This comes as a natural step when we consider short-ranged (i.e. first-neighbour tunneling or interactions) Hamiltonians although it can be generalized to long-ranged ones. As a result, we can express the evolution operator as a product of local terms of the form:

$$\hat{U}(\Delta t) = e^{-i\hat{H}\Delta t} = \prod_j^{M-1} e^{-i\hat{H}_{j,j+1}\Delta t} + \mathcal{O}(\Delta t^2). \quad (3.14)$$

where $\hat{H}_{j,j+1}$ is composed by the terms of the total Hamiltonian that act on sites j and $j+1$. By applying this decomposition we no longer require to store or manipulate a Hamiltonian of the size of the whole Hilbert Space but much smaller operators $\hat{H}_{j,j+1}$. As a result, we gain access to computing system sizes of which we can no longer store the whole Hamiltonian.

Something relevant to consider is that in general the terms $\hat{H}_{j,j+1}$ do not commute with each other and so refined versions of this method account for the error associated with the commutation of these operators. For example,

¹For a longer discussion see section 4.3 where we apply it in the context of tensor networks and we describe in greater detail the practical implementation.

a relevant case is the 4th-order decomposition (see [89]). As this technique will be used throughout this thesis in the context of tensor networks, a longer discussion about the practical implementation and usefulness of the method together with higher order expansions is provided in section 4.3.

Finally, another important point when considering the diagonalisation of \hat{H} is the possibility of exploiting certain system symmetries (we will also discuss this advantage in section 4.1.6). In many of the systems we study we have certain conservation laws, for example, when we study the Hubbard model for two Bloch bands in section 5.3. For that specific system, we know that the particle number is preserved since $[\hat{H}, \hat{N}] = 0$, with $\hat{N} = \sum_k^M \hat{n}_k$ the total particle number operator. Then, we can restrict our total Hilbert Space to the sector corresponding to the initial particle number N_0 , avoiding to compute the Hamiltonian for all the particle number sectors.

In general, the main idea is to find these conserved quantities that allow for the construction of Hamiltonians in restricted spaces or Hamiltonians in the global Hilbert space that become block-diagonal. In all these cases, the problem reduces to the diagonalisation of the individual blocks instead of the larger Hamiltonian providing a relevant speed-up and allowing to access bigger systems.

So far, we have focus on the evolution of a system that is isolated from its environment. However, in all physical scenarios the system will experience some external coupling with the environment. In the following section, we discuss how our ability to describe the system is modified in those cases.

3.3 Open quantum systems

An important consideration that we did not mention in chapter 2 when describing the quantum-many body problem is that in general all the systems that we study are open systems. Even in the case of cold atoms were experimental conditions guarantee them to be better isolated than many other quantum many-body systems (low temperatures, ultra-high vacuum, etc.), the coupling to the environment can play an important role in the system.

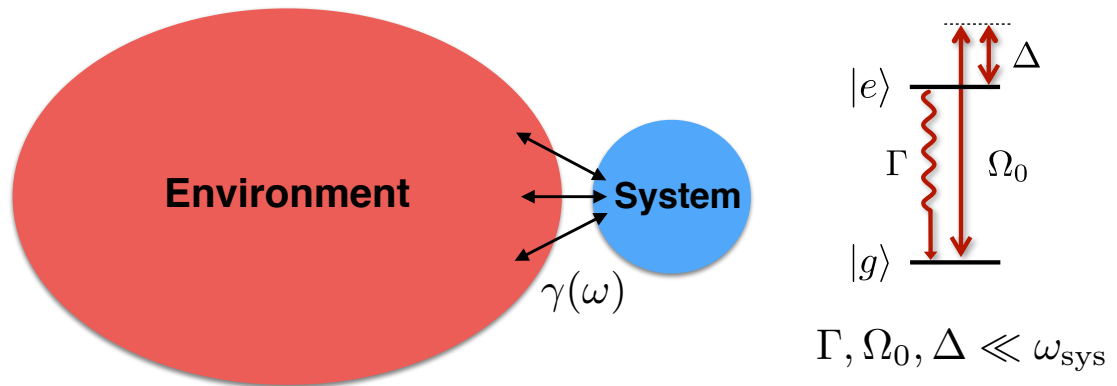


Figure 3.1: (Left) Open system diagram, the system couples to different modes ω of the environment with a coupling $\gamma(\omega)$; (right) depiction of the relevant frequency scales in the open system problem for the example of a two-level atom coupling to a radiation field. The system-environment coupling constant $\Gamma \equiv \gamma^2(\omega_{\text{sys}})$ must be much smaller than the dominant frequency ω_{sys} given by the energy separation ΔE of the two-levels $|e\rangle$ and $|g\rangle$ with $\Delta E = \hbar\omega_{\text{sys}}$, i.e. $\Gamma \ll \omega_{\text{sys}}$. Moreover, if the system is subject to an external coherent driving characterized by the coupling strength Ω_0 of the Rabi oscillations and detuning $\Delta = \omega_{\text{sys}} - \omega$ to the resonant coupling, both of these quantities are also required to satisfy $\Omega_0, \Delta \ll \omega_{\text{sys}}$.

As a result, throughout this thesis we require tools to describe the dynamics of systems weakly coupled to their environment as depicted in Fig.3.1. In this section, we will discuss the main approximations that allow for a Master Equation description of the quantum systems based on the separation of timescales between system and environment. With this derivation we will be able to not only tackle the dynamics of the system but also analyze how this coupling to an external bath can be exploited, for example, for the robust preparation of interesting states in the system².

3.3.1 Deriving the Master Equation

When describing the dynamics of the system plus its environment there are several important points to consider. First, the system is generally much smaller than its environment as for a thermal bath in Thermodynamics. Despite the fact that our closed system can be quite complex (with an exponential growth of its Hilbert Space), we always consider a bath composed of a much greater number of degrees

²For a relevant example, see chapter 5.

of freedom. This is clear in most examples in the context of Quantum Optics or Quantum Many-Body Physics, including a background radiation field or a reservoir gas for sympathetic cooling.

When we consider the global system (system and bath) we can decompose its Hamiltonian into different contributions:

$$\hat{H}_{\text{tot}} = \hat{H}_{\text{sys}} + \hat{H}_{\text{env}} + \hat{H}_{\text{int}}, \quad (3.15)$$

where \hat{H}_{sys} describes the Hamiltonian of the system, \hat{H}_{env} describes the Hamiltonian corresponding to the environment degrees of freedom and finally \hat{H}_{int} is associated with the (weak) coupling between both system and bath. As an example, we can consider the system as a two-level system composed of a ground state $|g\rangle$ and an excited state $|e\rangle$ that will couple to the bath. Therefore, its Hamiltonian can be described as $\hat{H}_{\text{sys}} = \omega_{\text{sys}} a_{\text{sys}}^\dagger a_{\text{sys}}$ where ω_{sys} is the frequency related to the separation of the two system levels with $\Delta E = \hbar\omega_{\text{sys}}$ and $a_{\text{sys}} = |g\rangle\langle e|$. In principle, the system can be subject to some external driving whose coupling constants are the associated Rabi frequency Ω_0 and the detuning Δ . Moreover, the reservoirs that we consider are typically composed by bosonic modes whose Hamiltonian is given by $\hat{H}_{\text{env}} = \int d\omega \omega b^\dagger(\omega)b(\omega)$ with the bosonic operators satisfying the standard commutation rules $[b(\omega), b^\dagger(\omega')] = \delta(\omega - \omega')$. Finally, the coupling between system and environment is described by terms of the form:

$$\hat{H}_{\text{int}} \propto \gamma(\omega) \left(a_{\text{sys}}^\dagger b(\omega) + b^\dagger(\omega) a_{\text{sys}} + b(\omega) a_{\text{sys}} + b^\dagger(\omega) a_{\text{sys}}^\dagger \right), \quad (3.16)$$

with $\gamma(\omega)$ the system-environment (S-E) coupling constant that, in principle, has a certain frequency dependence.

The aim is to compute the dynamics of the system in the presence of the environment. We can describe the system through the reduced density operator $\rho_{\text{sys}} = \text{Tr}_{\text{env}}(\rho_{\text{tot}})$ that we obtain by tracing out the environment degrees of freedom from the density operator ρ_{tot} describing the global system. In the following, we outline the main steps and key approximations to derive the evolution of ρ_{sys} via a Master Equation (for a complete derivation see [43, 44]).

We know that the equation of motion of the global system in the Schrödinger picture will be given by ($\hbar \equiv 1$):

$$\dot{\rho}_{\text{tot}} = -i \left[\hat{H}_{\text{sys}} + \hat{H}_{\text{env}} + \hat{H}_{\text{int}}, \rho_{\text{tot}} \right]. \quad (3.17)$$

From this expression we can move into the interaction picture, where:

$$\tilde{\rho}_{\text{tot}}(t) = e^{i(\hat{H}_{\text{sys}} + \hat{H}_{\text{env}})t} \rho_{\text{tot}}(t) e^{-i(\hat{H}_{\text{sys}} + \hat{H}_{\text{env}})t}, \quad (3.18)$$

and

$$\hat{H}_{\text{int}}(t) = e^{i(\hat{H}_{\text{sys}} + \hat{H}_{\text{env}})t} \hat{H}_{\text{int}} e^{-i(\hat{H}_{\text{sys}} + \hat{H}_{\text{env}})t}, \quad (3.19)$$

to obtain the following expression:

$$\dot{\tilde{\rho}}_{\text{tot}} = -i \left[\hat{H}_{\text{int}}(t), \tilde{\rho}_{\text{tot}}(t) \right]. \quad (3.20)$$

Now, we can differentiate and integrate again Eq.(3.20) to obtain the integro-differential equation:

$$\dot{\tilde{\rho}}_{\text{tot}} = -i \left[\hat{H}_{\text{int}}(t), \tilde{\rho}_{\text{tot}}(0) \right] - \int_0^t dt' \left[\hat{H}_{\text{int}}(t), \left[\hat{H}_{\text{int}}(t'), \tilde{\rho}_{\text{tot}}(t') \right] \right]. \quad (3.21)$$

Then, if we trace over the bath degrees of freedom in Eq.(3.21) we obtain:

$$\dot{\tilde{\rho}}_{\text{tot}} = - \int_0^t dt' \text{Tr}_{\text{env}} \left(\left[\hat{H}_{\text{int}}(t), \left[\hat{H}_{\text{int}}(t'), \tilde{\rho}_{\text{tot}}(t') \right] \right] \right), \quad (3.22)$$

where we used that $\text{Tr}_{\text{env}} \left(\hat{H}_{\text{int}}(t) \tilde{\rho}_{\text{tot}}(0) \right) = 0$. In general, we can satisfy this by simply adding any diagonal term of \hat{H}_{int} to \hat{H}_{sys} when considering the diagonal basis of \hat{H}_{env} .

So far, the derivation has been exact. However, in order to derive a master equation from Eq.(3.22) we need to introduce the two key approximations namely the Born and Markov approximations. These are described below:

1. *Born Approximation*: this first approximation assumes that the dynamics induced by the S-E coupling are small compared to the system or environment

ones. This implies that we can factorize our density operator as:

$$\tilde{\rho}_{\text{tot}}(t) \approx \rho_{\text{sys}}(t) \otimes \rho_{\text{env}}. \quad (3.23)$$

In other words, we consider that the S-E induced dynamics can be considered irrelevant for the environment while they can still be relevant for the system. Thus, the bath is assumed to be static. We can insert Eq.(3.23) this into Eq.(3.21) to obtain.

$$\dot{\tilde{\rho}}_{\text{tot}} = - \int_0^t dt' \text{Tr}_{\text{env}} \left(\left[\hat{H}_{\text{int}}(t), \left[\hat{H}_{\text{int}}(t'), \rho_{\text{sys}}(t') \otimes \rho_{\text{env}} \right] \right] \right), \quad (3.24)$$

2. *Markov Approximation*: this approximation has two implications. First, it assumes a constant S-E coupling (not frequency dependent over short timescales), that we implicitly used when defining Γ . Secondly, it implies that the dynamics of the system do not depend on its own previous history.

Indeed, if we consider the bath correlation functions given by $\langle b^\dagger(t)b(0) \rangle \rightarrow 0$ for times of the order of $t = \tau_{\text{env}}$. Typical decay times of the correlations τ_{env} ³, for example, thermal correlations, will be much smaller than the rate of change of $\tilde{\rho}_{\text{tot}}(t')$ which is given by $t \sim \Gamma^{-1}$ (see [43, 91]). That is to say,

$$\tau_{\text{env}} \ll \Gamma^{-1}. \quad (3.25)$$

As a result, we can substitute $\tilde{\rho}_{\text{tot}}(t')$ by $\tilde{\rho}_{\text{tot}}(t)$ and since the S-E coupling is weak we consider that $t \rightarrow \infty$.

From these approximations, we can derive a general form of the master equation given by:

$$\dot{\tilde{\rho}}_{\text{tot}} = - \int_0^\infty d\tau \text{Tr}_{\text{env}} \left(\left[\hat{H}_{\text{int}}(t), \left[\hat{H}_{\text{int}}(t - \tau), \rho_{\text{sys}}(t) \otimes \rho_{\text{env}} \right] \right] \right), \quad (3.26)$$

This equation, often referred as Redfield equation [43], does not guarantee a positive map for the density operator. For that condition to be fulfilled we require another approximation, namely the rotating-wave approximation [43, 92], that neglects the

³Values of τ_{env} are related to the inverse of the spectral width of the bath, see [90].

fast rotating terms of \hat{H}_{int} (in particular $b(\omega)a_{\text{sys}}$ and $b^\dagger(\omega)a_{\text{sys}}^\dagger$). This approximation requires that $\Omega_0, \Delta \ll \omega_{\text{sys}}$.

Since in typical cold atom systems $\tau_{\text{env}} \lesssim \omega_{\text{sys}}^{-1}$ [43, 90], it is quite common in the literature (see for example [92]) to discuss the existence of a dominant frequency in the total system or, in other words, the existence of a hierarchy of timescales given by:

$$\Gamma, \Omega_0, \Delta \ll \omega_{\text{sys}}, \quad (3.27)$$

which ensures the correctness of the Born, Markov and rotating-wave approximations; consequently, making it possible to derive the equation of motion for the density operator describing the system in the presence of dissipation induced by its environment.

We could stop this derivation here but it is important to consider a particular form of the master equation that is the one we utilize throughout the numerical calculations of this thesis. This is the case of the Lindblad form of the master equation (for a complete derivation see [93, 94]). This form defines the Lindbladian \mathcal{L} as a map to the evolution of ρ_{sys} that preserve the density operator properties (i.e. trace, hermiticity and positivity), treating the master equation as a quantum Markov process. The Lindblad master equation is given by⁴:

$$\dot{\rho} = \mathcal{L}\rho = -i [\hat{H}_{\text{sys}}, \rho] + \sum_i \frac{\Gamma}{2} \left(2\hat{L}_i \rho \hat{L}_i^\dagger - \{ \hat{L}_i^\dagger \hat{L}_i, \rho \} \right), \quad (3.28)$$

where the operators \hat{L}_i describe the i -th dissipation channel acting on the system after tracing out the environment degrees of freedom. This equation is equivalent to Eq.(3.26) after applying the rotating-wave approximation.

It is useful to provide some example of the type of operators that we consider throughout the different chapters of this thesis. As we consider atoms in optical lattices and the dissipation processes are usually local it is quite natural to associate

⁴To simplify the notation we use $\rho_{\text{sys}} \equiv \rho$

the index i with the i -th site of the lattice, however, in many occasions different dissipation processes are present in our models or these terms affect several sites. Then, in those cases the index will only have an ordering purpose. Typical examples of \hat{L}_i that we encounter range from completely local operators related to dephasing $\hat{L}_i = a_{\text{sys},i}^\dagger a_{\text{sys},i}$ or single-particle loss $\hat{L}_i = a_{\text{sys},i}$ (chapters 6 and 7) to more general terms that involve a set of sites $\hat{L}_i = b_{\text{sys},i+l}^\dagger a_{\text{sys},i}^\dagger b_{\text{sys},i} a_{\text{sys},i}$ with l a given distance in the lattice (chapter 5).

The master equation in Eq.(3.28) allows us to compute the evolution of the reduced density operator describing the system in a simple way. However, the exponential growth of the Hilbert Space causes the computation of open system dynamics to face serious bottlenecks as the system size grows since our reduced density operator ρ has a matrix representation of dimension $\dim(\mathcal{H}) \times \dim(\mathcal{H})$. One of the possible solutions to overcome this limitation is to consider the Markov process character of this equation and map the evolution into some form of stochastic evolution that after averaging recovers the same map. This is the topic of the following section.

3.3.2 Quantum trajectories:

Monte Carlo wave-function method

The notion of quantum trajectories was introduced by several independent groups studying a variety of Quantum Optics systems [45, 46, 47, 48], resulting in similar implementations of the same principle: a pure state sampling of the master equation (see reviews [92, 95]). The idea behind quantum trajectories is to overcome the obstacle of computing the evolution of ρ by evolving stochastically pure states that we can sample from the initial $\rho(0)$. In every instance a state $|\phi\rangle \in \mathcal{H}$ evolves under a non-Hermitian Hamiltonian and undergoes certain quantum jumps. Thus, every trajectory is numerically much less costly at the price of requiring certain sampling. It is clear that if the required sampling is smaller than the dimension of \mathcal{H} we obtain in principle an advantage by using quantum trajectories.

In order to provide a clear picture of how this works, let us now specify how the pure state evolution is calculated in a simple (first order) example. First, is it useful

to look at the form of Eq.(3.28) where we can absorb the commutator with the dissipation into our Hamiltonian to obtain:

$$\dot{\rho} = \mathcal{L}\rho = -i [\hat{H}_{\text{eff}}, \rho] + \sum_i \Gamma (\hat{L}_i \rho \hat{L}_i^\dagger), \quad (3.29)$$

where the effective Hamiltonian \hat{H}_{eff} is given by:

$$\hat{H}_{\text{eff}} = \hat{H}_0 - \frac{i\Gamma}{2} \sum_j \hat{L}_j^\dagger \hat{L}_j. \quad (3.30)$$

As a result, if we interpret Eq.(3.29) we can consider that the system evolves under a non-Hermitian Hamiltonian \hat{H}_{eff} and at certain times undergoes quantum jumps described by the operators \hat{L}_i . From this interpretation we can deduce the specifics of the implementation of the quantum trajectory method.

Firstly, suppose that we know the wavefunction that describes the system at time t , $|\phi(t)\rangle$. Then, we will calculate the “tentative” state at time $t + \delta t$ as (first order):

$$|\phi^{(1)}(t + \delta t)\rangle = (I - i\hat{H}_{\text{eff}} \delta t) |\phi(t)\rangle. \quad (3.31)$$

Simply by evolving under the effective Hamiltonian. As the system is evolving non-unitarily, the norm of the wavefunction will decrease:

$$\langle \phi^{(1)}(t + \delta t) | \phi^{(1)}(t + \delta t) \rangle = 1 - \delta p, \quad (3.32)$$

where $\delta p = \langle \phi(t) | i\delta t(\hat{H}_{\text{eff}} - \hat{H}_{\text{eff}}^\dagger) + O(\delta t^2) | \phi(t) \rangle = \Gamma \delta t \sum_j \langle \phi(t) | \hat{L}_j^\dagger \hat{L}_j | \phi(t) \rangle = \sum_j \delta p_j$.

Based on the change on the norm of the wavefunction, we can make the evolved state selection. We will choose:

- With probability $1 - \delta p$: the propagated state is just the normalized version of the “tentative” state:

$$|\phi(t + \delta t)\rangle = \frac{|\phi^{(1)}(t + \delta t)\rangle}{\sqrt{1 - \delta p}}. \quad (3.33)$$

- With probability δp : the system will perform a quantum jump:

$$|\phi(t + \delta t)\rangle = \frac{\sqrt{\Gamma} \hat{L}_j |\phi(t)\rangle}{\sqrt{\delta p_j / \delta t}}. \quad (3.34)$$

The j -th dissipative channel is chosen taking into account the weight of each δp_j in δp :

$$\Pi_j = \delta p_j / \delta p = \frac{\Gamma \delta t \langle \phi(t) | \hat{L}_j^\dagger \hat{L}_j | \phi(t) \rangle}{\delta p}. \quad (3.35)$$

Simply by iterating this method over time, and then, treating it as a stochastic propagation that should be averaged over trajectories we can calculate the time evolution of the system. What is now left to show is how this recovers the evolution given by the master equation.

Recovering the master equation

As we previously pointed out, we are going to relate this trajectory time evolution with the one provided in Eq.(3.28). Firstly, let us define the density operator from our initial pure state:

$$\sigma(t) = |\phi(t)\rangle \langle \phi(t)|. \quad (3.36)$$

Then, in a single time step, the trajectory averaged propagation of the density operator will be given by:

$$\overline{\sigma(t + \delta t)} = (1 - \delta p) \frac{|\phi^{(1)}(t + \delta t)\rangle \langle \phi^{(1)}(t + \delta t)|}{\sqrt{1 - \delta p}} + \delta p \Gamma \sum_j \Pi_j \frac{\hat{L}_j |\phi(t)\rangle \langle \phi(t)| \hat{L}_j^\dagger}{\delta p_j / \delta t}, \quad (3.37)$$

simply by choosing the evolved state or the jump instance with the corresponding probability. In first order, we can write $|\phi^{(1)}(t + \delta t)\rangle = (\mathbb{I} - i\hat{H}_{\text{eff}}\delta t) |\phi(t)\rangle$ and substitute in Eq.(3.37):

$$\begin{aligned} \overline{\sigma(t + \delta t)} &= |\phi(t)\rangle \langle \phi(t)| - i\delta t \left(\hat{H}_{\text{eff}} |\phi(t)\rangle \langle \phi(t)| - |\phi(t)\rangle \langle \phi(t)| \hat{H}_{\text{eff}}^\dagger \right) \\ &\quad + \Gamma \delta t \sum_j \hat{L}_j |\phi(t)\rangle \langle \phi(t)| \hat{L}_j^\dagger + O(\delta t^2). \end{aligned} \quad (3.38)$$

Thus, if we neglect second order terms in δt we obtain:

$$\overline{\sigma(t + \delta t)} = \sigma(t) - i\delta t(\hat{H}_{\text{eff}}\sigma(t) - \sigma(t)\hat{H}_{\text{eff}}^\dagger) + \Gamma\delta t \sum_j \hat{L}_j\sigma(t)\hat{L}_j^\dagger. \quad (3.39)$$

That we can rewrite as:

$$\frac{\overline{\sigma(t + \delta t)} - \sigma(t)}{\delta t} = -i(\hat{H}_{\text{eff}}\sigma(t) - \sigma(t)\hat{H}_{\text{eff}}^\dagger) + \Gamma \sum_j \hat{L}_j\sigma(t)\hat{L}_j^\dagger. \quad (3.40)$$

The expression in Eq.(3.40) is equivalent to the master equation evolution (Eq.(3.28)) in a single step. Thus, we can interpret the master equation as a weighted stochastic average over all possible jumps at all possible times.

Now, that we have proposed a method to overcome the problem of computing the evolution in the squared Hilbert Space, it is important to note that these techniques can be applied not only to the exact methods for time evolution presented in section 3.2 but also are applicable to the approximate methods that we discuss in chapter 4, related to matrix product states, where we can combine both methods to compute open system dynamics of larger systems.

3.4 Reservoir engineering and dark-state preparation

An immediate application of open many-body systems arises from a parallelism with a well-established technique in the closed system scenario. This technique, usually denoted as Hamiltonian engineering, is based on the modification of the system Hamiltonian in such a way that the desired state becomes the ground state of the engineered Hamiltonian. Then, it is enough to cool the system to its ground state to systematically prepare such a state:

$$|\psi(t)\rangle = e^{-i\hat{H}t}|\psi(0)\rangle \rightarrow |g\rangle \langle g| \quad (t \rightarrow \infty). \quad (3.41)$$

To complement this method we can consider the possibility of engineering the coupling to external reservoirs in such a way that the stationary state of the dissipative

dynamics is the target state. This method is usually referred to as reservoir engineering.

As we explain in previous sections, under the Born-Markov approximation, we can describe the dissipative evolution via a master equation in Lindblad form:

$$\dot{\rho} = \mathcal{L}\rho = -i [\hat{H}_{\text{sys}}, \rho] + \sum_i \frac{\Gamma}{2} \left(2\hat{L}_i \rho \hat{L}_i^\dagger - \{ \hat{L}_i^\dagger \hat{L}_i, \rho \} \right). \quad (3.42)$$

The steady state solution under such an evolution can be found from

$$\mathcal{L}\rho = 0 \Rightarrow \rho(t \rightarrow \infty) = \rho_{\text{steady}}. \quad (3.43)$$

If the steady state is pure we can describe it by its wavefunction $|\phi_{\text{steady}}\rangle$ which should satisfy

$$\left. \begin{aligned} \hat{H}_{\text{sys}}|\phi_{\text{steady}}\rangle &= E_\phi |\phi_{\text{steady}}\rangle \\ \hat{L}_i|\phi_{\text{steady}}\rangle &= 0 \quad \forall i \end{aligned} \right\}. \quad (3.44)$$

Thus, the state requires to be an eigenstate of the unitary Hamiltonian and also, a dark state of the jump operators describing the dissipation.

The method of dark-state driving [52, 53] has been successfully applied, for example, in cooling schemes [54, 55] or in the preparation of entangled states [56, 57, 58].

Chapter 4

Reduced Hilbert Space

Techniques: Density Matrix

Renormalization Group (DMRG)

As we already mentioned in the previous chapter, the nature of quantum mechanics poses important challenges when we try to compute static or dynamical properties of a quantum system. The main obstacle is the exponential growth of the Hilbert Space \mathcal{H} of these systems. The dimension of the Hamiltonians that describe cold atomic models grows too quickly to be able to numerically handle systems that have more than a few tens of atoms. In the case of a complicated local physical structure (such as several hyperfines levels per site or several Bloch bands included in the description) the size limit can become even smaller.

Moreover, if we pick a state from our large \mathcal{H} at random, the entanglement in spatial modes of such state will typically be much higher than the ones we are interested in. More specifically, in one-dimensional systems entanglement is known to be moderate for the ground or low-excited states of the Hamiltonians describing local motion and interactions. Then, in many cases the full Hilbert Space representation is unnecessary since the statics and dynamics of the system are restricted to a smaller part of these exponentially large spaces. Then, it is vital to consider methods that can represent efficiently the states we are interested in at a lower numerical cost.

This is the case of Density Matrix Renormalization Group introduced by S. R. White [35, 36], that allows for the calculation of ground states of large one-dimensional systems. These ground states can be represented by matrix product states (MPS) as it was later shown in ([37, 38, 96]). Later on, the concept of time-dependent DMRG (t-DMRG) ([39, 40, 41]) that adapts the Hilbert Space basis as the evolution occurs allowed for the calculation of dynamical quantities. Finally, it is important to mention the representation of operators in the language of matrix product operators (MPOs) as an extension of MPS [97, 98]. Throughout the years t-DMRG techniques have developed in different ways (see reviews [42, 99]) providing tools to tackle system that include higher dimensions. However, as the object of study in this thesis are one-dimensional systems we will restrict to the case of 1D tensor networks here, i.e. matrix product states.

The chapter is structured as follows: in section 4.1 we introduce the concept of MPS and how to systematically express a quantum state in this form. Moreover, we present the main properties of this formalism and how the success of this representation links to bipartite entanglement; in section 4.2 we discuss the extension to the representation of operators through MPOs; in section 4.3 we describe the main ideas behind t-DMRG and computing time evolution using MPSs; in section 4.4 we present the variational state search algorithm applying it not only to ground states but also to dissipative system calculations; finally, in section 5.6 we summarize the main advantages and possibilities that MPS provide. All the diagrams included are original unless indicated otherwise.

4.1 Matrix product state representation

4.1.1 Graphical notation for tensor networks

Before jumping into the explanation of matrix product states, it is useful when making use of density matrix renormalization group techniques to introduce a graphical notation to support the representation of the high-dimensional tensors that form the networks representing our states and operators. In the graphical notation the tensor representation becomes quite natural and so do all of the typical contractions

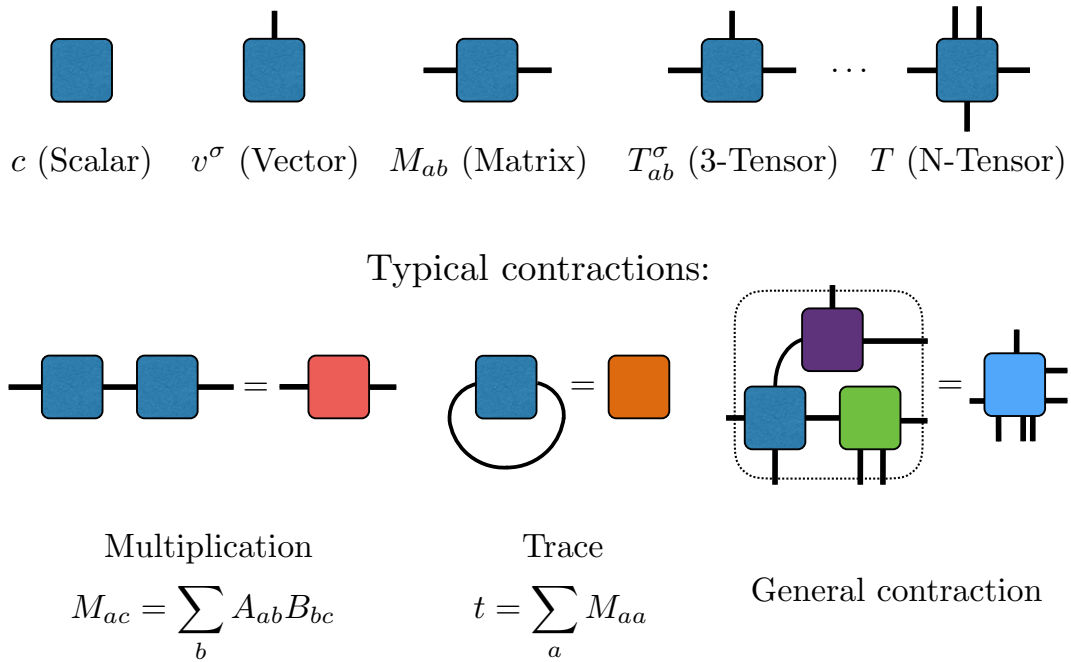


Figure 4.1: Summary of the graphical notation of tensor networks. The number of legs or links in every object denotes the dimension of the tensor which in general can have any number of legs. We will use greek letters to denote vertical links (related to the local physical dimension) and roman ones for horizontal legs (related to state compression). This will come naturally as we construct our matrix product state. In the bottom part we include some of the typical contractions that we perform: any two links that are connected indicate matrix multiplication through that index, we can also close indices of the same object as shown in the case of the trace.

that the algorithms that we will include require. Moreover, this notation will allow us to simplify the long matrix multiplications that typically represent states and operations.

In Fig.4.1 we include a summary of the rules of the graphical notation that will simplify in great manner the expressions required to compute relevant static and dynamical quantities in the language of matrix product states. In the next section we will describe how to construct a matrix product state from a given state expressed in the standard Hilbert space.

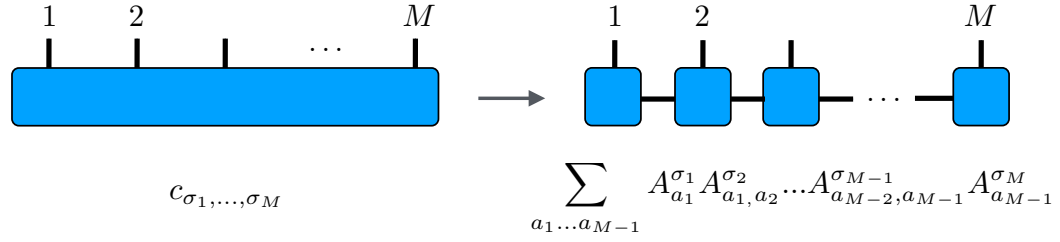


Figure 4.2: Graphical representation of the state $|\phi\rangle$ in standard and matrix product state form.

4.1.2 Matrix product state construction

In the following we will consider open boundary conditions (OBC), as that is the case of the models we will study in the result chapters and also it is the most relevant in optical lattice experiments¹. In order to construct the matrix product state (MPS) form, let us consider a state $|\phi\rangle$ in the Hilbert space \mathcal{H} with $\dim(\mathcal{H}) = d^M$ where d is the local physical dimension of our system (e.g. $d = 2$ for spin-1/2 particles or $d = 3$ for spin-1 particles) and M is the system size. As we mentioned earlier this space is exponentially large in the system size. If we want to describe our state $|\phi\rangle$ we will require a set of d^M coefficients that we denote as $c_{\sigma_1, \dots, \sigma_M}$ with $c_{\sigma_1, \dots, \sigma_M} = \langle \psi | \sigma_1, \dots, \sigma_M \rangle$ where the set $|\sigma_1, \dots, \sigma_M\rangle$ forms a complete basis in \mathcal{H} each local base σ^i with local dimension d . Then, we can express our state as:

$$|\phi\rangle = \sum_{\sigma_1, \dots, \sigma_M} c_{\sigma_1, \dots, \sigma_M} |\sigma_1, \dots, \sigma_M\rangle. \quad (4.1)$$

We can rewrite this set of coefficients in the following form²:

$$c_{\sigma_1, \dots, \sigma_M} = \sum_{a_1 \dots a_{M-1}} A_{a_1}^{[1] \sigma_1} A_{a_1, a_2}^{[2] \sigma_2} \dots A_{a_{M-2}, a_{M-1}}^{[M-1] \sigma_{M-1}} A_{a_{M-1}}^{[M] \sigma_M}, \quad (4.2)$$

where the matrices $A_{a_{i-1}, a_i}^{[i] \sigma_i}$ are three-dimensional matrices (there is a matrix for every local state on site $[i]$ with base $\{\sigma_i\}$). Each matrix has dimension dD_i^2 with d again

¹Similar analysis can be made for the case of periodic boundaries obtaining equivalent expressions (see [42, 99]) but this will not be covered in the chapter.

²This form might seem unnatural at first but we will justify it in section 4.1.3.

describing the local dimension and D_i so-called bond dimension that correspond to the dimension of the link between matrices (the links we multiply over). Please note that here we are considering that the local physical dimension d is homogeneous but this condition is just a simplification that is not required for this mapping. Then, we can express:

$$|\phi\rangle = \sum_{\sigma_1, \dots, \sigma_M} A^{[1]\sigma_1} A^{[2]\sigma_2} \dots A^{[M-1]\sigma_{M-1}} A^{[M]\sigma_M} |\sigma_1, \dots, \sigma_M\rangle. \quad (4.3)$$

The state of the system is now expressed via a matrix product state and can be graphically depicted as in Fig.4.2. So far we have not obtained any advantage from this new form since we have simply rewritten the state coefficients into a product of matrices of dimension MdD_i^2 instead of the general vector of coefficients of length d^M . The key-point here is the size of the bond dimension D_i . In order to understand this better let us consider two examples:

- Product state: If the state of the system is a product state then the global state of the system is just the product of the local states. Consequently, it is clear that every matrix $A_{a_{i-1}, a_i}^{[i]\sigma_i}$ should be able to capture the state in every site independently from the state in other sites. As a result, a product state has the trivial bond dimension $D_i = 1$ as shown in Fig.4.3.

We can immediately observe that this representation has a great advantage in the case of a product state since we simply need to keep $MdD_i^2 = Md$ complex numbers in comparison with the standard d^M . Even though the case of a product state is quite specific, product states or states closely related to them appear quite naturally in many of the projects discussed in this thesis. In particular, current experimental advantages allow to prepare systematically product states as initial state for many of the schemes that we will discuss.

For example, let us suppose that we have two spin-1/2 particles that are prepared independently in a superposition of state $|0\rangle$ and $|1\rangle$. Then, the state of the system

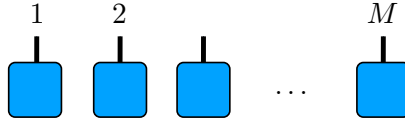


Figure 4.3: Graphical representation of a product state. The matrix product state representation of the state has the trivial bond dimension $D = 1$.

is given by the tensor product of both superposition states:

$$|\phi_{\text{Product}}\rangle = \frac{|0\rangle + |1\rangle}{\sqrt{2}} \otimes \frac{|0\rangle + |1\rangle}{\sqrt{2}}. \quad (4.4)$$

And, we have $\forall c_{i,j} = 1/2$. This can be then expressed in the matrix product form:

$$A^{[1]0} = A^{[2]0} = A^{[1]1} = A^{[2]1} = 1/\sqrt{2}. \quad (4.5)$$

Here, as the bond dimension becomes $D = 1$, these matrices become scalars.

- **Bell state [100]:** This is an interesting example not only for its physical relevance but also from the fact that it is the first state with non-trivial bond dimension D that we consider. The state is given by:

$$|\phi_{\text{Bell},+}\rangle = (|0_1\rangle |0_2\rangle + |1_1\rangle |1_2\rangle) / 2, \quad (4.6)$$

and so, we have $c_{0,0} = c_{1,1} = 1/\sqrt{2}$, $c_{1,0} = c_{0,1} = 0$. In terms of our matrix representation, we cannot express the state with just scalars as the state on one site conditions the state on the other one. We obtain:

$$A^{[1]0} = \begin{pmatrix} 1 & 0 \end{pmatrix}, \quad A^{[1]1} = \begin{pmatrix} 0 & 1 \end{pmatrix} \\ A^{[2]0} = \begin{pmatrix} 1/\sqrt{2} \\ 0 \end{pmatrix}, \quad A^{[2]1} = \begin{pmatrix} 0 \\ 1/\sqrt{2} \end{pmatrix}. \quad (4.7)$$

And $c_{\sigma_1, \sigma_2} = \sum_j A_{1j}^{[1]\sigma_1} A_{j1}^{[2]\sigma_2}$. We observe that our bond dimension is $D = 2$. Later on in section 4.1.4 we will link the growth of the bond dimension to the bipartite entanglement in the system and how these conditions our ability to represent efficiently a state in MPS form.

4.1.3 Canonical form of an MPS and gauge freedom

In order to construct our state we make use of a tool of the singular value decomposition (SVD). Given a matrix M with $\dim(M) = d_{M1} \times d_{M2}$ we can decompose it in a product of matrices of the following form:

$$M = USV^\dagger, \quad (4.8)$$

with U composed of orthonormal columns as they fulfill the property $U^\dagger U = I$ and $\dim(U) = d_{M1} \times \min(d_{M1}, d_{M2})$; S is a diagonal matrix of $\dim(S) = \min(d_{M1}, d_{M2}) \times \min(d_{M1}, d_{M2})$ formed by the singular values $\lambda_1 < \lambda_2 < \dots < \lambda_r$, we denote as Schmidt rank r the number of non-zero entries of S (we will describe the physical meaning of this rank in section 4.1.4); and, V^\dagger is composed of orthonormal rows as $VV^\dagger = I$ and $\dim(V) = \min(d_{M1}, d_{M2}) \times d_{M2}$.

One essential property of this decomposition is the fact that the best approximation to M with a smaller rank $r' < r$ is given by $M' = US'V^\dagger$ with S' the resulting diagonal matrix if we set to zero the singular values between r' and r . Then, we immediately observe that this provides a natural mechanism for the truncation of the matrices that we will describe in 4.1.4.

Now, we can apply this decomposition to our quantum state systematically and exploit the properties of orthonormality of U and V^\dagger .

Let us consider a given quantum state in a system of length M in one dimension in the same for as in Eq.4.1:

$$|\phi\rangle = \sum_{\sigma_1, \dots, \sigma_M} c_{\sigma_1, \dots, \sigma_M} |\sigma_1, \dots, \sigma_M\rangle. \quad (4.9)$$

In order to be able to perform SVD on our state we should first reshape the vector of coefficients into a matrix $c_{\sigma_1, \dots, \sigma_M} = M_{\sigma_1, (\sigma_2, \dots, \sigma_M)}$ of dimension $(d \times d^M - 1)$. We can decompose this matrix:

$$M_{\sigma_1, (\sigma_2, \dots, \sigma_M)} = \sum_{l_1}^{r_1} U_{\sigma_1, l_1} S_{l_1, l_1} V_{l_1, (\sigma_2, \dots, \sigma_M)}^\dagger \quad (4.10)$$

In order to recover a form consistent with MPS, we can group $S_{l_1, l_1} V_{l_1, (\sigma_2, \dots, \sigma_M)}^\dagger$ and obtain a new vector c . We also reshape U_{σ_1, l_1} as a set of row vectors $M_{l_1}^{[1] \sigma_1}$. With these transformations we can rearrange our state as:

$$c_{\sigma_1, \dots, \sigma_M} = \sum_{l_1}^{r_1} M_{l_1}^{[1] \sigma_1} c_{l_1, (\sigma_2, \dots, \sigma_M)} \quad (4.11)$$

This form already provided the desired MPS form in the first lattice site. Then, the process can be iterated to the next site:

$$c_{l_1, (\sigma_2, \dots, \sigma_M)} = M_{(l_1 \sigma_2), (\sigma_3, \dots, \sigma_M)} = U_{(l_1 \sigma_2), l_2} S_{l_2, l_2} V_{l_2, (\sigma_3, \dots, \sigma_M)}^\dagger \quad (4.12)$$

We can apply this new transformation to the state and again using $U_{(l_1 \sigma_2), l_2} = M_{l_1, l_2}^{[2] \sigma_2}$ and $S_{l_2, l_2} V_{l_2, (\sigma_3, \dots, \sigma_M)}^\dagger = c_{l_2, (\sigma_3, \dots, \sigma_M)}$ we obtain the following expression:

$$c_{\sigma_1, \dots, \sigma_M} = \sum_{l_1}^{r_1} \sum_{l_2}^{r_2} M_{l_1}^{[1] \sigma_1} M_{l_1, l_2}^{[2] \sigma_2} c_{l_2, (\sigma_3, \dots, \sigma_M)} \quad (4.13)$$

This procedure can be continued until we have covered the whole lattice as indicated in Fig.4.4. We finally obtain the form

$$|\phi\rangle = \sum_{\sigma_1, \dots, \sigma_M} \sum_{l_1}^{r_1} \sum_{l_2}^{r_2} \dots \sum_{l_M}^{r_M} M_{l_1}^{[1] \sigma_1} M_{l_1, l_2}^{[2] \sigma_2} \dots M_{l_{M-2}, l_{M-1}}^{[M-1] \sigma_{M-1}} M_{l_{M-1}, l_M}^{[M] \sigma_M}. \quad (4.14)$$

This form of an MPS is known as left-canonical³ since we have constructed it from the set of matrices U that contain the left singular vectors resulting of our SVD process. As a result, the matrices M possess the property of left-normalization:

³For a longer discussion of the different canonical forms see [99].

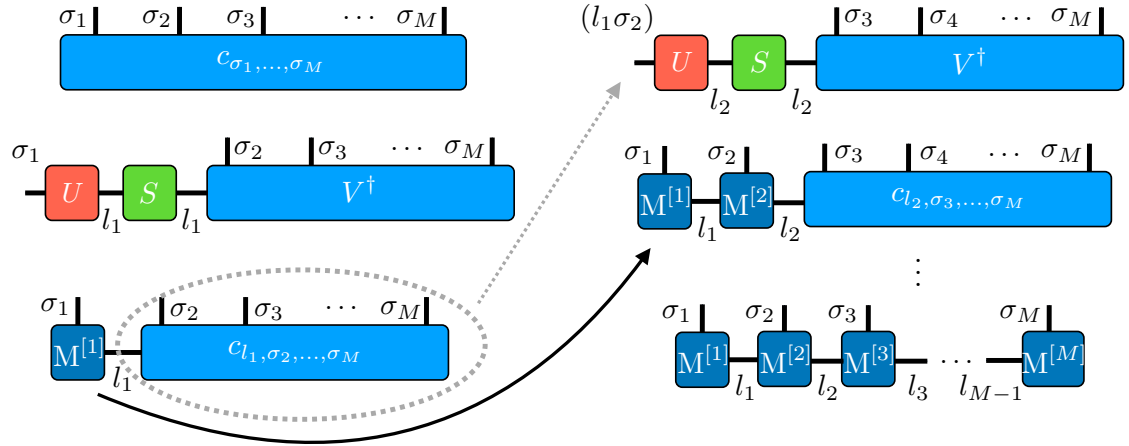


Figure 4.4: Iterative construction of a left-canonical MPS. Starting from the left hand-side, a singular value decomposition is performed taking one physical index σ_i at a time. After every decomposition the matrix U is reshaped into the appropriate form to create $M^{[i]}$ and the product of SV^\dagger is reshaped into a vector formed by a bond index to the left l_i and the set of left physical indices $\sigma_i + 1, \dots, \sigma_M$. This process is iterated until the whole lattice is covered. Original diagram based on [99].

$$\sum_{\sigma_i} \left(M^{[i] \sigma_i} \right)^\dagger M^{[i] \sigma_i} = I. \quad (4.15)$$

The utility of this normalization will be systematically explored in section 4.1.3.1, where we make use of the different normalization possibilities. Note that as the matrices are constructed from a systematic SVD taking a physical index of dimension d at every step, the maximum bond dimensions of the local tensors $M^{[i]}$ will follow the sequence $(1 \times d), (d \times d^2) \dots, (d^{L/2-1} \times d^{L/2}) \dots (d^2 \times d), (d \times 1)$, the fact that the first and last indices have dimension 1 is not surprising since the product of all matrices should produce a scalar that is the corresponding state coefficient.

We could naturally have started the process from the other end of the lattice and used the right singular vectors from V^\dagger during SVD operations to create our local matrices. If this second choice is iterated, the resulting matrices will be right-normalized fulfilling:

$$\sum_{\sigma_i} M^{[i] \sigma_i} \left(M^{[i] \sigma_i} \right)^\dagger = I, \quad (4.16)$$

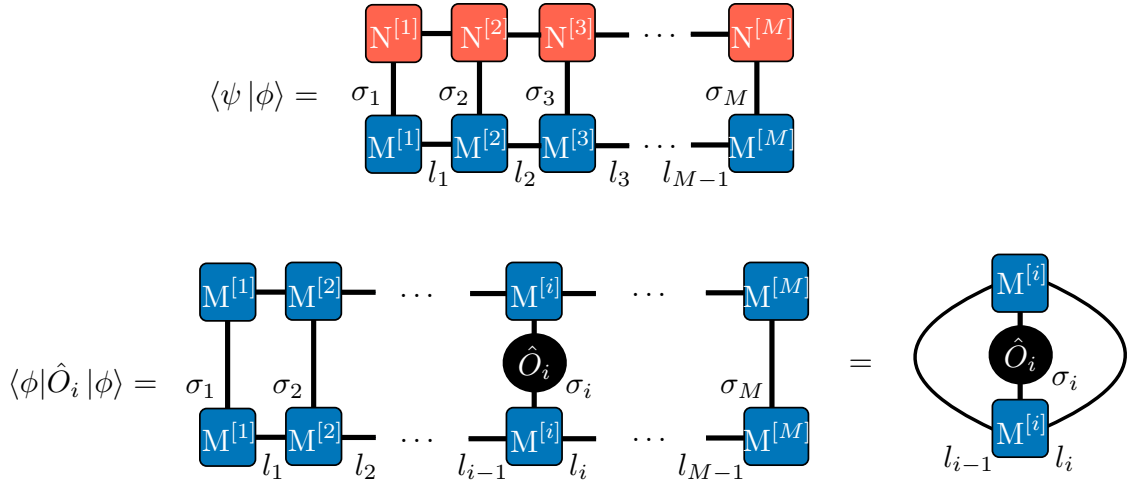


Figure 4.5: (Top) Overlap of two quantum states in MPS form; (bottom) local expectation value of the operator \hat{O}_i acting on site i through the use of left- and right-normalization we can eliminate any contribution outside the site where the operator acts on.

and the MPS is said to be in right-canonical form.

Moreover, we could consider the case of a mixture of both, where the SVD is performed starting from both left and right sides, meeting at site i , this choice becomes particularly useful when computing expectation values of local operators on site i (see 4.1.3.1). We note that here we have only presented a few possible representations but the MPS gauge freedom is much larger. In particular, in any bond with bond index l_i between matrices $M^{[i]}$ and $M^{[i+1]}$ we could insert an identity in the form $I_{l_i, l_i} = AA^{-1}$. Then, matrices A and A^{-1} could be absorbed into the left and right matrices generating $\tilde{M}^{[i]} = M^{[i]}A$ and $\tilde{M}^{[i+1]} = A^{-1}M^{[i+1]}$. We immediately observe that the representation has been modified keeping the state unchanged.

4.1.3.1 Typical operations in canonical form

The existence of the gauge freedom in the MPS representation will play a significant role in the calculation of overlaps and expectation values in MPS form. First, let us consider the overlap of two states in MPS form:

$$\langle \psi | \phi \rangle = \sum_{\sigma_1, \dots, \sigma_M} \left(N^{[1] \sigma_1} N^{[2] \sigma_2} \dots N^{[M-1] \sigma_{M-1}} N^{[M] \sigma_M} \right)^\dagger \cdot \left(M^{[1] \sigma_1} M^{[2] \sigma_2} \dots M^{[M-1] \sigma_{M-1}} M^{[M] \sigma_M} \right), \quad (4.17)$$

where we have omitted for simplicity the indices for the matrix multiplication. We can rearrange the expression in a more natural way:

$$\langle \psi | \phi \rangle = \sum_{\sigma_M} \left(N^{[M] \sigma_M} \right)^\dagger \left(\dots \left(\sum_{\sigma_1} \left(N^{[1] \sigma_1} \right)^\dagger M^{[1] \sigma_1} \right) \dots \right) M^{[M] \sigma_M}. \quad (4.18)$$

The graphical notation for the overlap can be found in the top part of Fig.4.5.

On the other hand, we could consider how we would compute expectation values of operators. Let us for the time being consider the operators to be local (if that is not the case we will typically make use of methods in section 4.2).

Given an operator \hat{O}_i acting on site i with dimension $(d \times d)$ we can first simply multiply it to either the *bra* or the *ket*, what it is important is that this operator will only appear in the link σ_i leaving the rest of the links unchanged. As we discussed before, if we choose to set the sites to the left $1, \dots, i-1$ to be left-normalized then, $\sum_{\sigma_j} \left(M^{[j] \sigma_j} \right)^\dagger M^{[j] \sigma_j} = I$ and consequently all the local contraction of indices just give an identity until reaching the site i . In the same way we could use right-normalization for sites $i+1, \dots, M$ given again no contribution in the contractions but an identity. As a result, computing expectation values of local operators becomes just the contraction of three matrices

$$\begin{aligned} \langle \psi | \hat{O}_i | \phi \rangle &= \sum_{l_{i-1}, l_i} \sum_{\sigma_i, \sigma'_i} \left(M_{l_{i-1}, l_i}^{[i] \sigma'_i} \right)^\dagger \cdot \hat{O}_i^{\sigma_i, \sigma'_i} \cdot M_{l_{i-1}, l_i}^{[i] \sigma_i} \\ &= \sum_{\sigma_i, \sigma'_i} \hat{O}_i^{\sigma_i, \sigma'_i} \text{Tr} \left(\left(M^{[i] \sigma'_i} \right)^\dagger M^{[i] \sigma_i} \right), \end{aligned} \quad (4.19)$$

which is numerically efficient (it scales with $\mathcal{O}(MD^3d)$, see [99]).

Often we require to compute expectation values of the form $\langle \psi | \hat{A}_i \hat{B}_j | \phi \rangle$ (e.g., two-point correlators). Then, normalization of our MPS can only be exploited in the region outside of the operators applied (between $1, \dots, i-1$ and $j+1, \dots, M$, assuming $i < j$), but still offers a numerical advantage.

4.1.4 Entanglement and truncation error

We can relate the systematic application of SVD to the state to the concept of Schmidt decomposition [100] of the quantum state. The Schmidt decomposition allows for the expression of a pure state in a pair of orthonormal bases $\{|i\rangle_A\}, \{|j\rangle_B\}$ spanning two partitions of the system that we denote as A and B :

$$|\phi\rangle = \sum_{i,j} \lambda_{ab} |i\rangle_A |j\rangle_B. \quad (4.20)$$

From this representation we can immediately construct the reduced density operator of the system bipartitions as $\rho_{A/B} = \text{Tr}_{B/A} (|\phi\rangle\langle\phi|)$. Then, if we choose this bipartition to correspond to the local matrices to the left and to the right of a given bond i . We can express our reduced density operator of a subsystem as:

$$\rho_{1,\dots,i-1} = \text{Tr}_{i+1,\dots,M} (|\phi\rangle\langle\phi|) = \sum_{l_i}^{r_i} (\lambda_i)^2 |i\rangle_A \langle i|_A. \quad (4.21)$$

where λ_i represent the singular values associated with the partition at site i .

Typically, our representation has a fixed maximum bond dimension D_{max} that we can numerically afford. The existence of this cutoff forces us to truncate the size of the local matrices $M^{[i]}$. As we mentioned in section 4.1.3 SVD naturally provides the best approximation for our matrices with a given fixed rank (simply by keeping the D_{max} greater singular values when storing the result of our SVD) with an associated truncation error:

$$\epsilon_i \equiv \sum_{l_i=D_{max}+1}^{r_i} (\lambda_i)^2. \quad (4.22)$$

Thus, this truncation has certain consequences in the states that we have the ability to represent efficiently (with manageable ϵ_i). An easy way to interpret which ones are those well presented states comes from Eq.(4.21) and the definition of Von Neumann entropy [100]:

$$S_{vN} = -\text{Tr}(\rho_{1,\dots,i-1} \ln \rho_{1,\dots,i-1}) = -\sum_{\lambda_i}^{r_i} (\lambda_i)^2 \ln (\lambda_i)^2 . \quad (4.23)$$

Consequently, there is an upper bound for the entanglement entropy that we can represent given by:

$$S_{vN}^{max} \leq \ln(D_{max}) . \quad (4.24)$$

As a result, the MPS representation will only be able to represent states with an entanglement inside this bound. Our truncated MPS representation covers now a much smaller region of the total Hilbert space \mathcal{H} .

Nevertheless, MPS has found great success in representing the lower energy states of gapped 1D systems. This is due in part to the existence of so-called “area laws” [101, 102, 103] that cause the entanglement entropy to be only dependent of the size of the partition boundary and not on the size of the system itself (not scaling with its volume) for the ground state of gapped Hamiltonian with local interactions. This is usually applicable more broadly to the low-energy states.

In the case of time evolution this condition becomes more complex as not always the dynamics will remain restricted to the small sector represented. In some of the cases we can faithfully represent the evolved state [104]. However, in general, the system will couple to highly excited states and that will limit the times that we are able to reach with the MPS representation as typical linear growths of entanglement will imply the need to exponentially increase D_{max} .

4.1.5 Vidal's notation

In section 4.1.3 we discussed the fact that the MPS representation is not unique and how we can exploit normalization properties to obtain interesting features in our representation. Now, it is important to introduce a different representation, namely Vidal's notation [39], that is particularly useful when considering system bipartitions.

This notation arises naturally from the concept of Schmidt decomposition that we introduced in section 4.1.4, as instead of a single matrix $M^{[i]\sigma_i}$ per site, our representation now consist of a matrix $\Lambda^{[i-1]}$ including the Schmidt coefficients associated with the bipartition in link $i - 1$ and a matrix $\Gamma^{[i]\sigma_i}$ such that:

$$M_{l_{i-1}, l_i}^{[i]\sigma_i} = \Lambda_{l_{i-1}, l_{i-1}}^{[i-1]} \Gamma_{l_{i-1}, l_i}^{[i]\sigma_i} \quad (4.25)$$

Thus, the total state can be written as

$$|\phi\rangle = \sum_{\sigma_1, \dots, \sigma_M} \Gamma^{[1]\sigma_1} \Lambda^{[1]} \Gamma^{[2]\sigma_2} \Lambda^{[2]} \dots \Gamma^{[M-1]\sigma_{M-1}} \Lambda^{[M-1]} \Gamma^{[M]\sigma_M} \quad (4.26)$$

The main advantage of this notation is that it gives immediate access to relevant quantities such as the reduced density operators on link $i - 1$ or the Von Neumann entropy associated with the bipartition (see Eq.4.21 and Eq.7.19). We will benefit from this notation in the calculations in chapter 6 and chapter 7. In the latter, we will explicitly use this notation when describing our parity-preserving algorithm (see section 7.3.3) that bases on ideas that we describe below in section 4.1.6.

4.1.6 Symmetries and number conserving codes

So far we have discussed how MPS provide an efficient representation of states with moderate entanglement. We can go one step farther and try to exploit certain properties of the system we aim to represent via MPS, to gain extra numerical advantages [105, 106]. In particular, in many instances we will have certain conserved quantities that reduce the sector of the global Hilbert space that we require to explore.

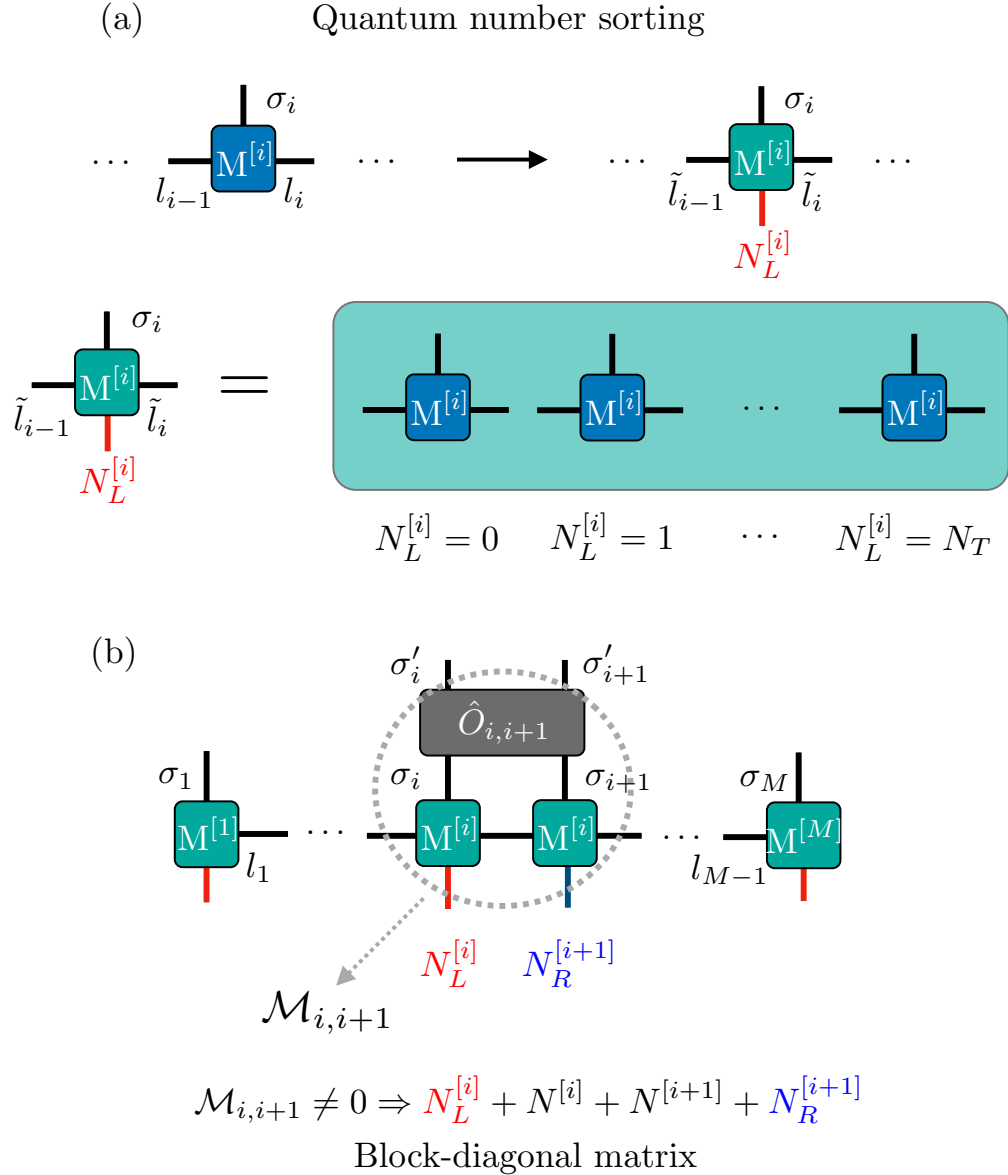


Figure 4.6: (a) Restructure of the MPS representation into the symmetry conservation rule. All Schmidt states acquire an associated quantum number related to the conserved quantity. We store our state in a vector of MPSs with each of the entries containing the MPS related to a given value of $N_L^{[i]}$; (b) when a local operator $\hat{O}_{i,i+1}$ acts on our number conserving MPS, the resulting matrix $\mathcal{M}_{i,i+1}$ that we have to recompress into an MPS is block-diagonal due to the symmetry conservation rules. This provides a relevant numerical advantage.

This is the case of number conserving codes that exploit the fact that our Hamiltonian possess that symmetry. For example, when studying closed system Hubbard models (see chapter 2) our Hamiltonian commutes with the particle number operator $\hat{n}_i = a_i^\dagger a_i$ with $[\hat{H}, \hat{n}_i] = 0$ and so the application of \hat{H} to our state (for variational state search or time evolution) will preserve \hat{n}_i .

Moreover, if we consider a bipartition of the system, we know that Schmidt decomposition provides an orthonormal basis to the left and to the right of that bond. Then, we can associate to every Schmidt vector in the basis the corresponding particle quantum number to the left or the right $N_{L/R}^{[i]}$. With this sorting index $N_{L/R}^{[i]}$, we can group together our MPS in a vector that contains in every entry the reduced MPS associated with a particular quantum number $N_{L/R}^{[i]} = n$.

The utility of this sorting becomes clear when we update our state after applying a local operator. In order to enforce this symmetry into our algorithms we can make use of the fact that during our MPS routines we typically modify matrices locally (see sections 4.4 and 4.3). Both variational state search and time evolution rely on every step on a SVD of the updated site or pair of sites.

If we apply a local operator $\hat{O}_{i,i+1}$ (see Fig.4.6) onto our state such that $[\hat{O}_{i,i+1}, \hat{n}_i + \hat{n}_{i+1}] = 0$. Then, the total particle quantum number N_T should be preserved, imposing that $N_T = N_L^{[i]} + N^{[i]} + N^{[i+1]} + N_R^{[i+1]}$ with $N^{[i]}$ and $N^{[i+1]}$ the local quantum numbers of the site affected by the operator. This constrain simplifies the resulting matrix $\mathcal{M}_{i,i+1}$ that we generate after applying $\hat{O}_{i,i+1}$ on our state, making it block-diagonal since only elements that fulfill the number condition can be non-zero.

As a result, we can perform SVD on a set of smaller matrices instead of the full $\mathcal{M}_{i,i+1}$ gaining a significant advantage in the numerical performance. Furthermore, as this storage scheme is sparse we can typically deal with bigger D_{max} values, as the overall size of the matrices gets significantly reduces. A final advantage that is important to mention is the fact that this storage naturally provides a mean for parallelization as different particle sectors get treated independently.

Note, that the particle conservation rules can be adapted to certain operators that do not preserve particle number as long as we update the indexing accordingly. An example is single-particle loss (we include this type of dissipation in many calculations in chapters 6 and 7). We can update the state as the loss occurs by a single-site operator \hat{a}_i acting on site i only modifying the particle number in the given site ($N_L^{[i]}$ and $N_R^{[i]}$ do not change). As a result, the application of the operator implies $\tilde{N}_T = N_L^{[i]} + N^{[i]} + N_R^{[i]} = N_T - 1$ and we just need to update the index values of $N_{L/R}^{[j \neq i]}$ in the rest of sites.

The use of symmetries in MPS will have an enormous impact in our calculations in chapters 6 and 7 where we make use of the number conserving in two ways. On the one hand, we will exploit the numerical advantages just mentioned to provide a relevant speed-up to our calculations. On the other hand, including this symmetry in our representation allows for the immediate extraction of the particle number $N^{j < i}$ to the left of a given site i . This number operator is quite crucial when computing fermionic operators as anticommutation of fermions creates highly non-local string operators associated with the Jordan-Wigner transformation (see section 2.4.1.1). Then, if our state representation stores these population sectors separated we do not require to compute the non-local strings but simply apply the appropriate phases. This avoids dealing with non-local operators in MPS language which typically requires the use of matrix product operators as we will now explain.

4.2 Matrix product operators

Now that we have introduced the notion of MPS and how it represents a given quantum state, we can easily generalize this concept to operators [98, 99]. When we considered operators so far in this chapter they were completely local. As a result, we can represent them as local matrices $\hat{O}_{\sigma_i, \sigma'_i}$ with dimension $(d \times d)$ that act on the physical indices of our MPS, this was also generalized to a two-site operator $\hat{O}_{(\sigma_i, \sigma'_i), (\sigma_{i+1}, \sigma'_{i+1})}$ with dimension $(d^2 \times d^2)$.

However, operators in general are non-local and require an expression in the whole

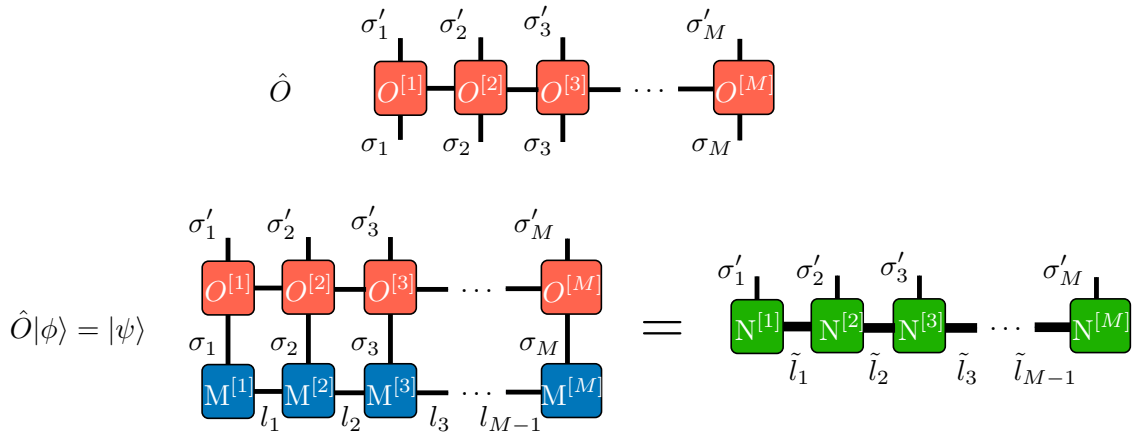


Figure 4.7: (Top) Graphical representation of a matrix product operator (MPO); (bottom) application of an MPO on a MPS representation of a state. The application does not alter the MPS form of the state at the cost of requiring a higher bond dimension \tilde{l}_i to represent it.

Hilbert space of dimension $(d^M \times d^M)$. Given an operator we can express it as:

$$\hat{O} = \sum_{\sigma_1, \dots, \sigma_M, \sigma'_1, \dots, \sigma'_M} c_{(\sigma_1, \dots, \sigma_M), (\sigma'_1, \dots, \sigma'_M)} |\sigma_1, \dots, \sigma_M\rangle \langle \sigma'_1, \dots, \sigma'_M|. \quad (4.27)$$

Then, we should be able to find a representation of operators as a generalization of the MPS representation of states. In particular, we can find the matrix elements of an operator as

$$\langle \vec{\sigma} | \hat{O} | \vec{\sigma}' \rangle = \sum_{\vec{\sigma}, \vec{\sigma}'} O^{[1] \sigma_1 \sigma'_1} O^{[2] \sigma_2 \sigma'_2} \dots O^{[M-1] \sigma_{M-1} \sigma'_{M-1}} O^{[M] \sigma_M \sigma'_M}, \quad (4.28)$$

where $|\vec{\sigma}\rangle, |\vec{\sigma}'\rangle$ are two given states in \mathcal{H} . This expression, that we denote as matrix product operator (MPO), is simply an extension of the form of an MPS with two physical indices instead of one corresponding to the in- and out-going indices acting on an operator. Then, the local matrices $O^{\sigma_1 \sigma'_1}$ are now 4-legged tensors with two physical indices and as MPS two bond dimensions D_{i-1}, D_i that in principle can be different, so every local tensor has dimension $d^2 \times D_{i-1} \times D_i$.

Although with the use of MPO we cannot find a canonical representation of our operators as we did with states, MPO representations are typically quite sparse and

require moderate bond dimensions D_i for the model that we usually consider in 1D many-body physics. This can be seen in the example we include below. Furthermore, another advantage of the use of MPO is that it preserves the form of the MPS when acting on a state:

$$\hat{O}|\phi\rangle = \sum_{\sigma_1, \dots, \sigma_M, \sigma'_1, \dots, \sigma'_M} \left(O^{[1]\sigma_1\sigma'_1} O^{[2]\sigma_2\sigma'_2} \dots O^{[M-1]\sigma_{M-1}\sigma'_{M-1}} O^{[M]\sigma_M\sigma'_M} \right) \times \left(M^{[1]\sigma_1} M^{[2]\sigma_2} \dots M^{[M-1]\sigma_{M-1}} M^{[M]\sigma_M} \right), \quad (4.29)$$

this can be reexpressed as:

$$\hat{O}|\phi\rangle = \sum_{\sigma'_1, \dots, \sigma'_M} N^{[1]\sigma'_1} N^{[2]\sigma'_2} \dots N^{[M-1]\sigma'_{M-1}} N^{[M]\sigma'_M}, \quad (4.30)$$

with

$$N_{(D_{i-1}l_{i-1}), (D_i l_i)}^{[i]\sigma'_i} = \sum_{\sigma_i} O_{D_{i-1}, D_i}^{[i]\sigma_i\sigma'_i} M_{l_{i-1}, l_i}^{[i]\sigma_i}. \quad (4.31)$$

Where the MPS structure has been preserved at the cost of increasing the bond dimensions as the product of the original bond dimensions of the MPO and the MPS. This can also be incorporated naturally to the graphical notation as depicted in Fig.4.7.

4.2.1 MPO example: Transverse Ising model

We are going to consider the Ising model as an example for the MPO construction. Since it only includes first-neighbour interaction and a local field term we will obtain bond dimensions that are quite small so it is an illustrative example. The Hamiltonian of the Ising model with transverse field is given by:

$$\hat{H} = -J \sum_{\langle ij \rangle} \hat{\sigma}_i^z \hat{\sigma}_j^z - h \sum_i \hat{\sigma}_i^x, \quad (4.32)$$

with $\langle ij \rangle$ denoting first neighbour summation, J the spin-interaction strength, h the magnetic field constant and $\hat{\sigma}_i$ the Pauli matrices on the local Hilbert space of site

i. This Hamiltonian can be expressed as a product of local 4-legged matrices that can be obtained from the general rule provided in [99, 107], which takes into account when sweeping from one end of the lattice the operators we can find moving along the lattice,

$$O^{[i]} = \begin{pmatrix} \hat{I} & \sqrt{J}\hat{\sigma}_i^z & h\hat{\sigma}_i^x \\ 0 & 0 & \sqrt{J}\hat{\sigma}_i^z \\ 0 & 0 & \hat{I} \end{pmatrix}, \quad (4.33)$$

with the boundaries

$$O^{[1]} = \begin{pmatrix} \hat{I} & \sqrt{J}\hat{\sigma}_1^z\hat{I} & h\hat{\sigma}_1^x \end{pmatrix}, \quad O^{[M]} = \begin{pmatrix} h\hat{\sigma}_M^x \\ \sqrt{J}\hat{\sigma}_M^z \\ \hat{I} \end{pmatrix}. \quad (4.34)$$

As was the case of the MPS, the boundary matrices $O^{[1]}, O^{[M]}$ differ in their dimensions as they need to provide a scalar at both ends of the chain. We immediately observe that the bond dimension is rather small due to the fact that we are only considering first-neighbour terms.

MPOs allow for the efficient representation of models that have more complex coupling such as long-range interactions at the cost of an increasing bond dimension (see [98]) in general any function can be expressed as a sum of exponentials that can be then inserted into our MPO. MPO find also utility when representing open quantum systems as they can be used to encode density operators in the form of MPDO (see [97]).

4.3 Time-Evolving Block Decimation

Different algorithms for the computation of time-evolution in the language of MPS have been developed over the years. Here we will focus on the Suzuki-Trotter decomposition applied to the tensor network language (see also section 3.2.1). This method, so-called Time-Evolving Block Decimation, ([39, 40]) adapts the application of local partitions of the evolution operator to the language of matrix product states.

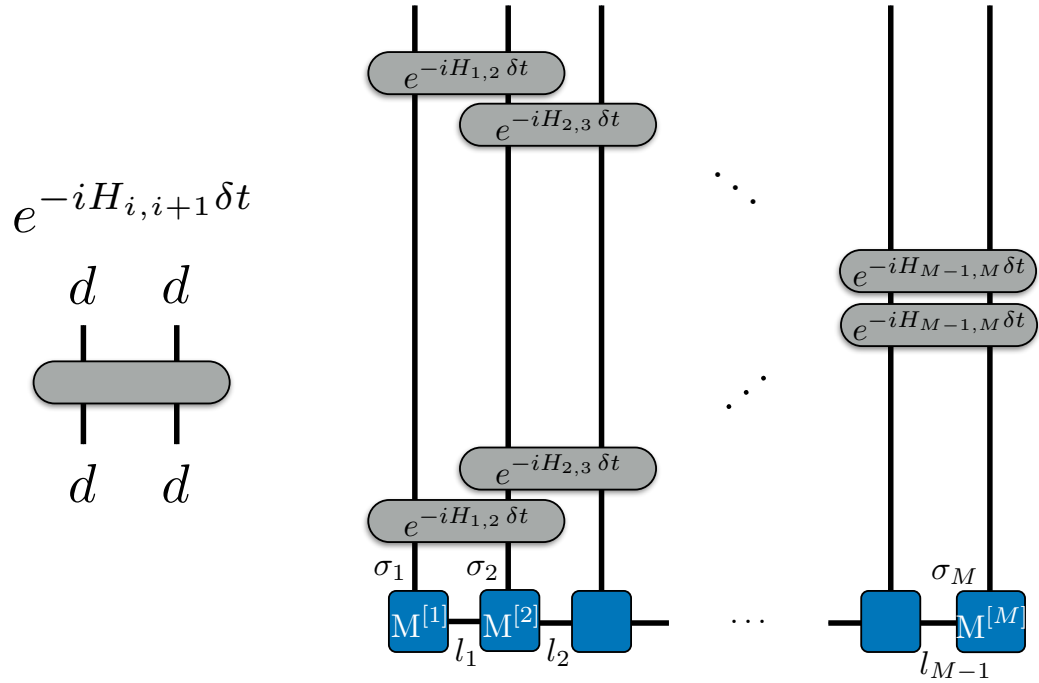


Figure 4.8: Diagram of the iterative application of the time-evolving blocks to the state in MPS form. Each evolution operator has dimension $(d^2 \times d^2)$.

This method seems as a natural step when we consider Hamiltonians with short-range interactions (as it is the cases of this thesis) as every term of the evolution operator can be decomposed into a set of local evolution operators $\hat{U}_{j,j+1}(t) = e^{-i\hat{H}_{j,j+1}t}$ where $\hat{H}_{j,j+1}$ is composed by the terms of the total Hamiltonian that act on sites j and $j + 1$. Thus, we can express:

$$\hat{U}(\delta t) = e^{-i\hat{H}\delta t} = \prod_j^{M-1} e^{-i\hat{H}_{j,j+1}\delta t} + \mathcal{O}(\delta t^2). \quad (4.35)$$

Note that given a Hamiltonian with first-neighbours coupling only, we can immediately provide a higher order approximation by considering that all terms with odd or even values of i commute with each other. Then, we can define $e^{-i\hat{H}_{\text{odd}}\delta t} = \prod_{j \in \text{odd}} e^{-i\hat{H}_{j,j+1}\delta t}$ and $e^{-i\hat{H}_{\text{even}}\delta t} = \prod_{j \in \text{even}} e^{-i\hat{H}_{j,j+1}\delta t}$ with which we can easily express the second-order Trotter expansion:

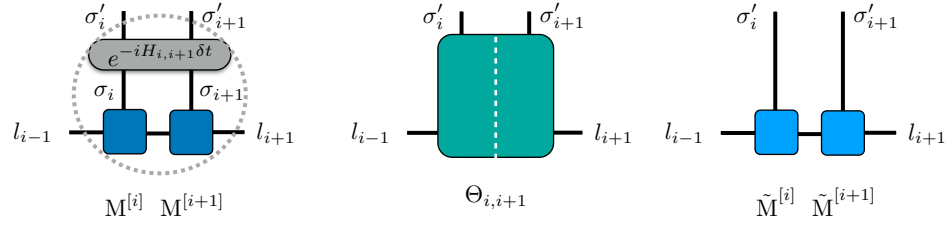


Figure 4.9: Application of a single TEBD gate to the local MPS tensors, the contraction of the tensors generates $\Theta_{i,i+1}$ over which we perform SVD to truncate our increasing bond dimension and recover the local MPS structure.

$$\hat{U}(\delta t) = e^{-i\hat{H}\delta t} = e^{-i\hat{H}_{\text{odd}}\delta t/2} e^{-i\hat{H}_{\text{even}}\delta t} e^{-i\hat{H}_{\text{odd}}\delta t/2} + \mathcal{O}(\delta t^3). \quad (4.36)$$

Similar extensions to higher-order Trotter expansions can be constructed (see [89]). The main idea is that extending the algorithm to higher orders allows for the increase in the size of the time-step and potentially provide and speed-up for the calculation. A relevant factor to take into account is that the application of the evolution operators in the local tensors of our MPS will increase the required bond dimension to represent them. As our resources are limited (see section 4.1.4) we need to truncate our tensor after every application to a maximum bond dimension D_{max} .

The process is depicted in Fig.4.9. After we apply the evolution operator on sites i and $i+1$, we contract the inner indices generating a 4-legged tensor that we reshape into a matrix $\Theta_{i,i+1}$ of dimension $(dD_i - 1 \times dD_i)$, grouping together the left and right indices. Then, we can perform SVD on $\Theta_{i,i+1}$ keeping the D_{max} greater Schmidt coefficients. After this, the resulting truncated matrices can be reshaped into the local tensors to preserve the MPS structure.

By iteratively applying TEBD steps to our state we can compute the desired time evolution. Note that there are two different error sources here. On the one hand, we have the truncation error in every SVD step which is the one that we can monitor from the Schmidt coefficients that we discard. This first error source is the one that usually sets the maximum times we can evolve to, as at a given point in the evolution our D_{max} will not be able to represent our state within an acceptable error. On the other hand, there is the error associated with the Trotter expansion that accumulates

over the application of TEBD steps. A study of the convergence for different values of δt can ensure that this error does not affect our result.

4.3.1 Imaginary time evolution

An interesting application of our time evolution algorithm is imaginary time evolution that instead of dynamics allows for the computation of the system's ground state. The idea behind it is rather simple, we simply consider time evolution under imaginary time $\tau = -it$. If we express our state in terms of the eigenvectors of \hat{H} :

$$|\psi\rangle = \sum_n \alpha_n |\phi_n\rangle \quad (4.37)$$

with $\hat{H}|\phi_n\rangle = E_n|\phi_n\rangle$ and $E_0 < E_1 < \dots$. Thus, we can decompose the time evolution as:

$$\begin{aligned} |\psi(\tau)\rangle &= \sum_{n=0} \alpha_n e^{-E_n\tau} |\phi_n\rangle = \sum_{n=0} \alpha_n e^{-E_0(E_n/E_0)\tau} |\phi_n\rangle = \\ &= e^{-E_0\tau} |\phi_0\rangle + \sum_{n=1} \alpha_n e^{-E_0(E_n/E_0)\tau} |\phi_n\rangle \xrightarrow{\tau \rightarrow \infty} |\phi_0\rangle \end{aligned} \quad (4.38)$$

Then, we observe that as the ground state is the slower decaying term in the imaginary time evolution the system will converge to $|\phi_0\rangle$. In principle, for this method to be successful we require that there is some overlap of our initial state and the ground state $\langle\psi|\phi_0\rangle \neq 0$. However, numerical error comes in our aid since any numerical noise proportional to the ground state will be exponentially amplified during the procedure. As a result, in practical terms this requirement can be relaxed.

4.4 Variational state search

Now, that we have discussed the building blocks of our representation it is quite pertinent to discuss the algorithms that we can develop with them in order to be able to calculate equilibrium quantities or to compute the system evolution.

The first of the algorithms we will discuss is based on the variational modification of

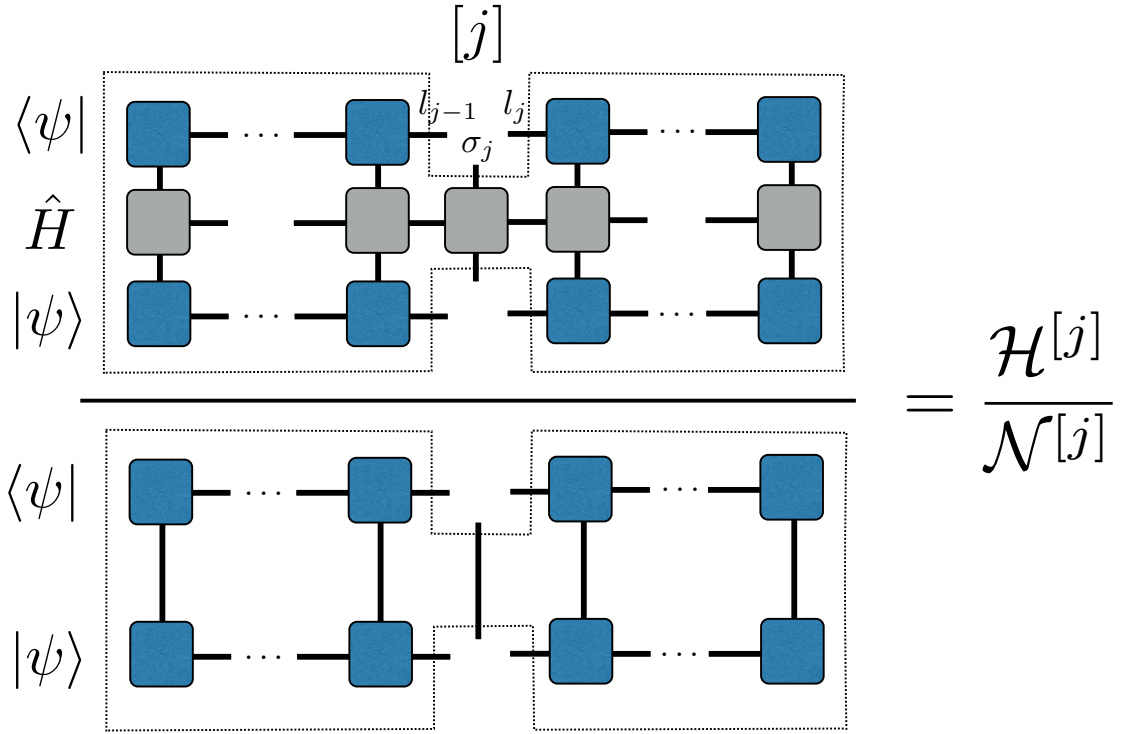


Figure 4.10: Graphical representation of the effective Hamiltonian $H_{eff} := \langle l_{j-1} \sigma_j l_j | \hat{H} | l'_{j-1} \sigma'_j l'_j \rangle$.

our state locally. This method is a natural extension of the real space renormalization of the original DMRG techniques [35, 36].

4.4.1 Ground state variational search

MPS techniques allow for two straight-forward ways of computing ground states: variational state search, which modifies our state locally minimizing the energy in every local iteration and imaginary time evolution (see section 4.3.1). The main idea behind variational DMRG is to iteratively minimize the energy on a given site sweeping from side to side of the lattice until convergence to the ground state is obtained. First, we can express the Hamiltonian as an MPO that we then apply to our state building the expectation value of the state energy $\langle \psi | \hat{H} | \psi \rangle$ in an MPS-MPO-MPS form.

Then, we can remove the local tensors representing the state on site j . In order to optimize this calculation, we can exploit the gauge freedom on our MPS (mixed canonical form centered in the considered site) obtaining:

$$|\psi\rangle = \sum_{\sigma} A^{\sigma_1} \dots A^{\sigma_{j-1}} \Psi^{\sigma_j} B^{\sigma_{j+1}} \dots B^{\sigma_M} |\vec{\sigma}\rangle. \quad (4.39)$$

The removal of the local tensors in site j allows for the construction of an effective Hamiltonian of dimension $(d^2 \times D_{j-1}^2 \times D_j^2)$ out of the contraction of the rest of the sites:

$$\begin{aligned} \langle l_{j-1} \sigma_j l_j | \hat{H} | l'_{j-1} \sigma'_j l'_j \rangle &= \sum_{b_{j-1}, b_j} L_{b_{j-1}}^{l_{j-1}, l'_{j-1}} H_{b_{j-1} b_j}^{\sigma_j, \sigma'_j} R_{b_j}^{l_j, l'_j} \\ L_{b_{j-1}}^{l_{j-1}, l'_{j-1}} &= \sum_{\{l_i, b_i, l'_i; i < j-1\}} \left(\sum_{\sigma_1 \sigma'_1} \left(A_{1, l_1}^{\sigma_1} \right)^* H_{1, b_1}^{\sigma_1, \sigma'_1} A_{1, l'_1}^{\sigma'_1} \right) \dots \\ &\quad \left(\sum_{\sigma_{j-1} \sigma'_{j-1}} \left(A_{l_{j-2}, l_{j-1}}^{\sigma_{j-1}} \right)^* H_{b_{l-2}, b_{l-1}}^{\sigma_{j-1}, \sigma'_{j-1}} A_{l'_{j-2}, l'_{j-1}}^{\sigma'_{j-1}} \right) \\ R_{b_j}^{l_j, l'_j} &= \sum_{\{l_i, b_i, l'_i; i > j\}} \left(\sum_{\sigma_{j+1} \sigma'_{j+1}} \left(B_{l_j, l_{j+1}}^{\sigma_{j+1}} \right)^* H_{b_j, b_{j+1}}^{\sigma_{j+1}, \sigma'_{j+1}} B_{l'_j, l'_{j+1}}^{\sigma'_{j+1}} \right) \dots \\ &\quad \left(\sum_{\sigma_M \sigma'_M} B_{l_{M-1}, l_M}^{\sigma_M} H_{b_{M-1}, b_M}^{\sigma_M, \sigma'_M} B_{l'_{M-1}, l'_M}^{\sigma'_M} \right). \end{aligned} \quad (4.40)$$

This construction is depicted in Fig.4.10. Thus, our goal is to iteratively minimize the following local expression⁴:

$$\min \left(\frac{V^{[j]\dagger} H_{eff}^{(j)} V^{[j]}}{V^{[j]\dagger} N_{eff}^{(j)} V^{[j]}} \right), \quad (4.41)$$

where $N_{eff}^{(j)}$ is nothing but the effective norm of the state given by the MPS obtained by performing the same contraction around the site j . Here $V_{\sigma_j a_{j-1} a_j}^{[j]}$ represents the vectorization of the MPS for site j of dimension $(d D_{i-1} D_i)$. Once we have obtained this lower energy eigenvector, we can reshape it into our updated $M_{a_{l-1}, a_l}^{\sigma_l}$. Then, we perform either QR decomposition (if we are moving to the right) or LQ (if vice versa). Supposing we are moving to the right, then:

$$M_{a_{l-1}, a_l}^{\sigma_l} = Q_{a_{l-1}, a_{l-1}}^{\sigma_l} R_{a_{l-1}, a_l}^{\sigma_l}, \quad (4.42)$$

⁴This expression corresponds to the generalized eigenvalue problem $\hat{H}V - \lambda \hat{N}V = 0$.

where we are only store the matrix Q , which is a unitary matrix. Through the use of QR decomposition we can ensure normalization of the local state and thus turn the problem into a standard eigenvalue problem.

This process can be iterated through the lattice until we find convergence to the ground state.

4.4.2 Variational search for a dissipative steady state

Similarly, to what we just presented we can use a variational state update to search for the steady state solution of open system dynamics [108]. In the same spirit as in section 3.3 we search for a state that satisfies:

$$\mathcal{L}\rho_{ss} = \dot{\rho}_{ss} = 0. \quad (4.43)$$

That is to say, ρ_{ss} is an eigenvector with eigenvalue zero of the superoperator \mathcal{L} . Furthermore, this state also satisfies:

$$\mathcal{L}^\dagger \mathcal{L} \rho_{ss} = 0. \quad (4.44)$$

Then, the steady state ρ_{ss} corresponds to the lower eigenvalue of $\mathcal{L}^\dagger \mathcal{L}$ since $\mathcal{L}^\dagger \mathcal{L} \geq 0$. As a result, we are presented with an equivalent problem to the case of the ground state variational search although now the space of the problem is \mathcal{H}^2 instead of H . Note that in general, $\mathcal{L}^\dagger \mathcal{L}$ can become not local and, thus only certain \mathcal{L} can be tackled through this method.

Choi's Isomorphism: vectorizing the density operator

Since our density operator is indeed an operator, it should be represented through a MPDO and, consequently, we cannot immediately make use of all the existing tools that we have presented for variational search. In order to do so, we have to vectorize ρ to be able to express it through a MPS. This procedure is known as Choi's Isomorphism and it is given by:

$$|\sigma_i\rangle \langle \sigma'_i| \Rightarrow |\sigma_i \sigma'_i\rangle \quad \rho = \sum_{\sigma_i, \sigma'_i} \rho_{\sigma_i \sigma'_i} |\sigma_i\rangle \langle \sigma'_i| \rightarrow \rho := \sum_{\sigma_i, \sigma'_i} \rho_{\sigma_i \sigma'_i} |\sigma_i \sigma'_i\rangle, \quad (4.45)$$

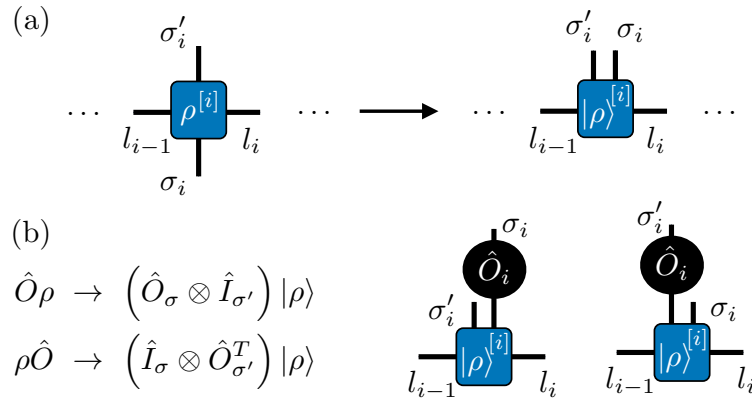


Figure 4.11: (a) Choi’s Isomorphism for the density operator: the rearrangement of the local matrices allows for the expression of ρ in the form of an MPS of physical dimension d^2 . This vectorization can be generalized to any operator; (b) rules of the extension of local operators acting on the matrices of the vectorized $|\rho\rangle$.

with $|\sigma_i\sigma'_i\rangle := |\sigma_i \otimes \sigma'_i\rangle$. This is illustrated in Fig.4.11.(a). Although the underlying idea is quite simple, just a rearrange of the indices, it has some relevant implications in our formalism as we have access to the toolbox of MPS at the price of representing our density operator as an MPS with squared local dimension d^2 . At the same time this representation should preserve certain properties of a density operator, namely: trace unitarity, hermiticity and positivity. The two first conditions can be easily enforced from the local matrices. On the other hand, the third condition is non-local as it requires to consider the whole spectrum so it cannot be immediately enforced. There are certain ways to work around this problem, the main one is the purification (see [109] and [110]for 2D) of the state that consist in the construction of our density operator from a pure state tracing out some auxiliary degrees of freedom that we introduce.

Now that we have a vectorized form of our density operator, we can think of \mathcal{L} simply as an operator acting linearly on $|\rho\rangle$. Nevertheless, it is important to consider the way that operators have to be extended to the squared physical space and how they

act on the MPS of dimension d^2 (see Fig.4.11.(b)). Let us consider a simple case:

$$\begin{aligned}\hat{O}\rho &= \sum_{\sigma_i, \sigma'_i} (\hat{O}\rho)_{\sigma_i \sigma'_i} |\sigma_i\rangle \langle \sigma'_i| = \sum_{\sigma_i, \sigma'_i, k} \hat{O}_{\sigma_i k} \rho_{(k \sigma'_i)} |\sigma_i\rangle \langle \sigma'_i| \\ &\rightarrow \sum_{\sigma_i, \sigma'_i, k} \hat{O}_{\sigma_i k} \rho_{(k \sigma'_i)} |\sigma_i \sigma'_i\rangle .\end{aligned}\tag{4.46}$$

$$\begin{aligned}\rho\hat{O} &= \sum_{\sigma_i, \sigma'_i} (\rho\hat{O})_{\sigma_i \sigma'_i} |\sigma_i\rangle \langle \sigma'_i| = \sum_{\sigma_i, \sigma'_i, k} \rho_{(\sigma_i k)} \hat{O}_{k, \sigma'_i} |\sigma_i\rangle \langle \sigma'_i| \\ &\rightarrow \sum_{\sigma_i, \sigma'_i, k} \rho_{(\sigma_i k)} \hat{O}_{k \sigma'_i} |\sigma_i \sigma'_i\rangle = \sum_{\sigma_i, \sigma'_i, k} \hat{O}_{\sigma'_i k}^T \rho_{(\sigma_i k)} |\sigma_i \sigma'_i\rangle .\end{aligned}$$

Then, given our local extended basis, we can see that the operators can be described depending on the side on which they act as

$$\begin{aligned}\hat{O}\rho &\rightarrow (\hat{O}_\sigma \otimes \hat{I}_{\sigma'}) |\rho\rangle , \\ \rho\hat{O} &\rightarrow (\hat{I}_\sigma \otimes \hat{O}_{\sigma'}^T) |\rho\rangle ,\end{aligned}\tag{4.47}$$

with $\hat{I}_{\sigma/\sigma'}$ the identity of dimension $(d \times d)$ acting on the corresponding physical index. The essential point is that from this rule we can extract the form of the Lindbladian for the vectorized density operator space directly as

$$\begin{aligned}\mathcal{L} &= -i (\hat{H} \otimes \hat{I} - \hat{I} \otimes \hat{H}^T) + \\ &+ \gamma \left[\sum_i \hat{L}_i \otimes \overline{(\hat{L}_i)} - \frac{1}{2} (\sum_i \hat{L}_i^\dagger \hat{L}_i) \otimes \hat{I} - \frac{1}{2} \hat{I} \otimes (\sum_i \hat{L}_i^T \overline{(\hat{L}_i)}) \right] ,\end{aligned}\tag{4.48}$$

where the operators L_i define the local dissipation jumps that we want to model, the overbar defines complex conjugation and γ is the dissipation strength that we have chosen to be constant for the sake of simplicity. Let us consider again an example with the transverse Ising model

$$\hat{H} = -J \sum_{\langle ij \rangle} \hat{\sigma}_i^z \hat{\sigma}_j^z - h \sum_i \hat{\sigma}_i^x .\tag{4.49}$$

In addition, our Lindbladian is given by

$$\mathcal{L}\rho = -i [\hat{H}, \rho] + \sum_i \frac{\gamma}{2} \left(2\hat{L}_i\rho\hat{L}_i^\dagger - \{\hat{L}_i^\dagger\hat{L}_i, \rho\} \right), \quad (4.50)$$

where we have chosen as an example that our dissipator is given by $\hat{L}_i = \hat{\sigma}_i^+$. Now, our goal is to express this sum of local operators as an MPO. In order to do that we can consider the same method discussed in [99, 107]. If we consider the commutator, we have to take into account the fact that the operators $\sigma_i^{x,z}$ are indeed now $\sigma_i^{x,z} \otimes \hat{I}$ or vice-versa. Let us then define to simplify our expressions

$$\tilde{\sigma}_i^{x,z} := \hat{\sigma}_i^{x,z} \otimes \hat{I} \quad \tau_i^{x,z} := \hat{I} \otimes \hat{\sigma}_i^{x,z}. \quad (4.51)$$

First, let us consider the terms arising from the commutator $-i [\hat{H}, \rho]$ in MPO form

$$O^{[i]} = \begin{pmatrix} \hat{I} \otimes \hat{I} & -i\sqrt{J}\tilde{\sigma}_i^z & i\sqrt{J}\tau_i^z & -ih(\tilde{\sigma}_i^x - \tau_i^x) \\ 0 & 0 & 0 & \sqrt{J}\tilde{\sigma}_i^z \\ 0 & 0 & 0 & \sqrt{J}\tau_i^z \\ 0 & 0 & 0 & \hat{I} \otimes \hat{I} \end{pmatrix}, \quad (4.52)$$

with the boundaries

$$O^{[1]} = \begin{pmatrix} \hat{I} \otimes \hat{I} & -i\sqrt{J}\tilde{\sigma}_1^z & i\sqrt{J}\tau_1^z & -ih(\tilde{\sigma}_1^x - \tau_1^x) \end{pmatrix}, \quad (4.53)$$

$$O^{[M]} = \begin{pmatrix} -ih(\tilde{\sigma}_M^x - \tau_M^x) \\ \sqrt{J}\tilde{\sigma}_M^z \\ \sqrt{J}\tau_M^z \\ \hat{I} \otimes \hat{I} \end{pmatrix}.$$

If we consider now the addition of the local dissipation given by \hat{L}_i , those elements will only appear on the right upper corner term as they are completely local. Then,

the rest of the matrix will remain unchanged obtaining

$$\mathcal{L} \rightarrow O_{\mathcal{L}}^{[i]} = \begin{pmatrix} \hat{I} \otimes \hat{I} & -i\sqrt{J}\tilde{\sigma}_i^z & i\sqrt{J}\tau_i^z & O_{\mathcal{L}03}^{[i]} \\ 0 & 0 & 0 & \sqrt{J}\tilde{\sigma}_i^z \\ 0 & 0 & 0 & \sqrt{J}\tau_i^z \\ 0 & 0 & 0 & \hat{I} \otimes \hat{I} \end{pmatrix}, \quad (4.54)$$

with the boundaries

$$O_{\mathcal{L}}^{[1]} = \begin{pmatrix} \hat{I} \otimes \hat{I} & -i\sqrt{J}\tilde{\sigma}_1^z & i\sqrt{J}\tau_1^z & O_{\mathcal{L}03}^{[1]} \end{pmatrix}, \quad O_{\mathcal{L}}^{[M]} = \begin{pmatrix} O_{\mathcal{L}03}^{[M]} \\ \sqrt{J}\tilde{\sigma}_M^z \\ \sqrt{J}\tau_M^z \\ \hat{I} \otimes \hat{I} \end{pmatrix}. \quad (4.55)$$

where, we remind the reader that given the dissipator choice we have $\hat{L}_i = \sigma_i^+$, $\hat{L}_i^\dagger = \sigma_i^-$ and $\overline{(\hat{L}_i)} = \sigma_i^+$, then:

$$O_{\mathcal{L}03}^{[i]} = -ih(\tilde{\sigma}_i^x - \tau_i^x) + \gamma \left[\hat{\sigma}_i^+ \otimes \tau_i^+ - \frac{1}{2} (\hat{\sigma}_i^- \hat{\sigma}_i^+ \otimes \hat{I} + \hat{I} \otimes \tau_i^- \tau_i^+) \right]. \quad (4.56)$$

Variational search for steady state

Once we have obtained the expression of the Lindbladian as a MPO, there are several alternatives in order to search for the steady state solution. In principle, all the tools developed for the ground state variational search can be used with the physical dimension of all our tensors being now d^2 .

1. We could consider to simply find the eigenvector of eigenvalue $\lambda_{\mathcal{L}} = 0$ of the operator \mathcal{L} (see [111]). In this way we do not need to compute $\mathcal{L}^\dagger \mathcal{L}$, which would substantially increase the bond dimension of the MPO. The cost of this choice is that typically as a non-Hermitian operator \mathcal{L} behaves worse in terms of convergence for the variational algorithm.
2. We can consider the product $\mathcal{L}^\dagger \mathcal{L}$ as an MPO already contracted before the construction obtaining an expression similar to Eq.(4.54) and (4.55). This allows for the immediate use of the variational search algorithm. However, the MPO

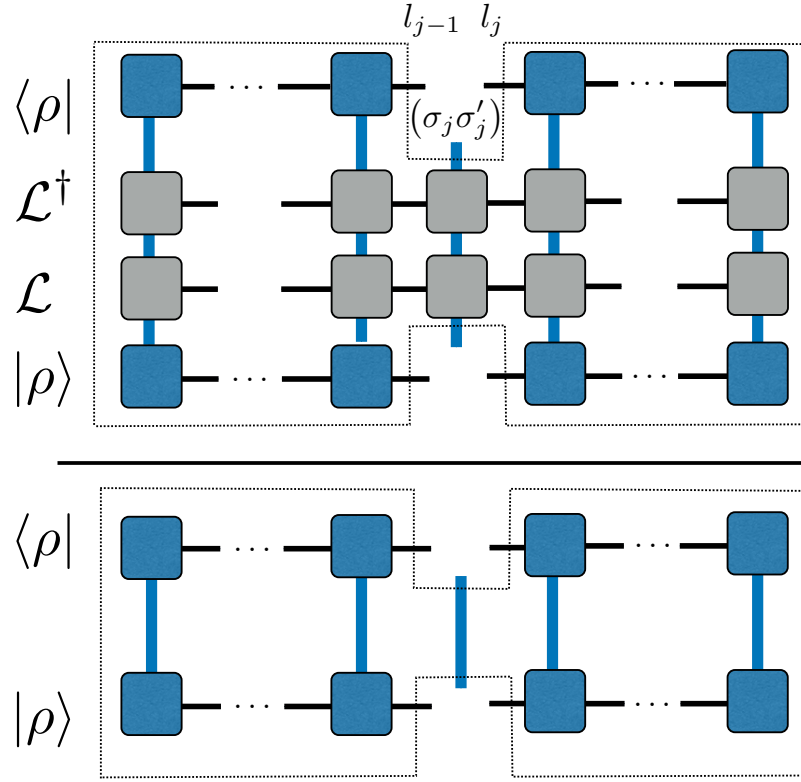


Figure 4.12: Diagram of $\mathcal{L}^\dagger \mathcal{L}_{eff} := \langle l_{j-1} (\sigma_j \sigma'_j) l_j | \mathcal{L}^\dagger \mathcal{L} | l'_{j-1} (\sigma''_j \sigma'''_j) l'_j \rangle$. The rearranged physical index of dimension d^2 is highlighted in blue.

is not the most efficient as the bond dimension of the product of operators increases substantially.

3. The best approach is to consider both terms \mathcal{L}^\dagger and \mathcal{L} as different MPOs, then we can contract it in the most efficient way, as it is discussed in [99] for the case of a single MPO. Then, our tensor structure will be composed of an MPS, MPO, MPO and MPS (see Fig.4.12) optimizing the contractions and providing a relevant speed-up.

Regardless of the method chosen, to find the steady state of a master equation, is it enough to formulate again a generalized eigenvalue problem as we did for the ground state (Eq.(4.41)). We can formulate our problem as an eigenvector equation for the vector arising when we vectorize $|\rho\rangle$, into a vector $V_{l_{j-1}l_j}^{[j] \sigma_j \sigma'_j}$ of dimension $(d^2 D_{j-1} D_j)$:

$$\min \left(\frac{V^{[j]\dagger} \mathcal{M}_{eff}^{(j)} V^{[j]}}{V^{[j]\dagger} N_{eff}^{(j)} V^{[j]}} \right), \quad (4.57)$$

with $\mathcal{M}_{eff}^{(j)}$ the effective matrix generated from the contractions of all sites but j of our MPS and our MPO (representing either \mathcal{L} or $\mathcal{L}^\dagger \mathcal{L}$ depending on the choice). There are certain technical points that it is important to mention regarding this method and its comparison with ground state search.

First, the convergence of the variational search for steady state, as for ground states of 1D systems depends on the existence of an energy gap in the spectrum. Then, the convergence of this algorithm can be compromised if there is some degeneracy on the steady state of the Lindbladian (e.g. the model in chapter 5). In general, the spectrum of typical Lindbladians for cold atom systems will be typically worse-behaved than the corresponding Hamiltonians requiring higher bond dimensions for convergence.

Secondly, as we mentioned before, the vectorized form of $|\rho\rangle$ cannot ensure the physicality of the result by construction. This is due to the fact that we cannot guarantee the positivity of the spectrum. However, on the models that we tested we observed that starting from a positive state and updating the state locally, as shown in Fig.4.12, positivity was preserved. This was, nevertheless, an observation from the benchmarking in simple Lindbladians that we cannot assume as a general property.

It is also important to mention that this method has shown better performance when the steady state of the system is mixed. We can intuitively understand this by thinking of the bond dimension cost of representing a maximally mixed state ($\rho \propto I$) with the vectorized MPS is rather small compared to the density operator coming for a highly-entangled pure state. Thus, mixed states exhibit typically better numerical performance with this variational method.

As a result, this method will provide an additional tool for the calculations on open systems and an interesting method to test our results of other methods. However, more generally we will focus on combining time-evolution techniques as TEBD (see section 4.3) and quantum trajectories (see section 3.3.2) to tackle open systems.

4.5 Conclusion

In this chapter we presented a summary of relevant numerical techniques that we will exploit throughout this thesis. In particular, we have presented why MPS provided a useful truncated representation of one-dimensional quantum systems. This is due to the fact that MPS support sufficient bipartite entanglement to represent low-excited states of physically relevant Hamiltonians.

In addition, we provided a set of tools to compute both ground-state properties and dynamics where we systematically compress our state representation to the best possible way for the given resources. In all of the presented techniques we have the ability to monitor the errors derived from the different approximations performed and so we have access to the regimes of validity of the calculations performed.

All of the MPS-related techniques, together with the exact methods provided in chapter 3, allowed to compute the numerical results obtained in the different result chapters. In particular, the combination of quantum trajectories and MPS played a vital role in tackling open system dynamics.

In the following chapters, we will make use of these techniques adapting existing codes in the group in C++ and MATLAB. In particular, the group codes contained a wide set of standard routines with MPS (section 4.1.3.1 and 4.1.4) including time evolution (section 4.3) or ground state calculation (section 4.4). The author of this thesis adapted the existing TEBD algorithms to open systems (see section 3.3.2) also in the case of quantum number conservation (section 4.1.6) and developed the codes for density matrix algorithms including the variational steady state search (section 4.4.2). None of the presented results was based on an open access library.

Chapter 5

Dissipative engineering of spin-entangled fermionic states in optical lattices

5.1 Introduction

The efficient and systematic engineering of many-body entangled states in atomic and molecular (AMO) systems has become an essential tool in the field of quantum simulation and also in quantum metrology, where the use of entanglement has allowed us to surpass the precision of classical schemes [112, 3, 5, 113, 114]. The preparation of many entangled states relies on the cooling of the system to the ground state of a tunable Hamiltonian. However, this approach usually requires in order to obtain a highly-entangled state for experimentally relevant system sizes not only a really fine control over the system parameters but also a preparation scheme that is robust to imperfections and noise sources in the system. Recently, inspired by ideas of Quantum Optics, the ultracold atom community has considered the possibility of including dissipative drivings, coherent and non-coherent, that can filter the system into states that were not accessible in the closed system scenario or that improve the efficiency with which those states are prepared. Relevant examples of dissipation processes for the present discussion include particle losses in the optical lattice [63, 62] and the coupling to a reservoir gas [51, 54, 55]. The ideas presented can be included

in the more general framework of reservoir engineering (see section 3.4), which is based on the modification of the coupling of the system and environment interaction in such a way that the desired state is the steady state of the open system dynamics.

In this chapter we propose a new scheme, based on dissipative dynamics, for the preparation of completely spin-symmetric states exploiting statistics of fermions in an optical lattice which are coupled to a BEC reservoir [51]. We make use of the correspondence between spatial and spin symmetries in fermions [115] and the fact that for ultracold atoms the dominant scattering is s-wave two-body collisions, which is spatially symmetric, to dynamically filter out the desired spin symmetry sector. Previously, proposals suggested to use this collisional mechanism at the cost of a significant decrease in the particle number [58]. By combining a Raman coupling between lattice bands and dissipative coupling with a BEC reservoir, this new scheme prepares a spin-symmetric state preserving the particle number and enhancing the potential precision for quantum metrology experiments.

The structure of this chapter is as follows: in section 5.2 we discuss the dissipative model that we based on and how we can exploit the symmetries to create a useful dark state; in section 5.3 we discuss in depth the specific scheme to prepare a completely spin-symmetric state; in section 5.4 we characterize the properties of this steady state and link it to relevant quantities in metrology; in section 5.5 we discuss the results obtained from our numerical simulations; and, in section 5.6 we present our findings and propose some future directions with which this scheme could be improved.

5.2 The dissipative model

Our goal is to create a highly entangled state in the lattice by preparing a completely spin-symmetric state starting with a random configuration with N atoms in M sites where we choose that in our system $N_{\uparrow} = N_{\downarrow}$ (the relevance of this choice is discussed in depth in the coming sections).

To prepare our entangled state, we take inspiration from the fact that s-wave scattering provides a natural mechanism to filter out space symmetry sectors. As we did

in section 2.3, for low temperatures we can describe the inter-atomic interaction via low-energy scattering theory. For sufficiently low temperatures, s-wave scattering is the only relevant contribution. The important point here is that scattering properties become independent of the direction, as s-waves have spherical symmetry. As s-wave collisions are space-symmetric only space-symmetric wavefunctions are affected by those.

Moreover, the fermionic wavefunction possesses a global antisymmetry under exchange of particles. This creates a direct correspondence between space and spin symmetries; i.e., if one of them is symmetric that forces the other to be antisymmetric to fulfill Fermi statistics.

Finally, we also take into account the fact that in a one-dimensional Hubbard model (see section 2.4.1) the symmetry sectors are not coupled by the tunneling terms or the onsite-interaction (we discuss this in section 5.2.1.1 and 5.2.1.2). Therefore, if we drive the system to the desired symmetry sector through some dissipative coupling, the unitary dynamics will not compete with this driving. We incorporate all these ideas while designing our dissipative driving scheme.

5.2.1 Making use of the fermionic symmetries to design our dissipator

In this section we will discuss the main ingredients required for the proposed scheme of state distillation.

First, let us assume, that we can express the open system evolution under the Born-Markov approximation¹ in a master equation of the Lindblad form [43]:

$$\dot{\rho} = \frac{d\rho}{dt} = -i [\hat{H}_0, \rho] - \frac{1}{2\hbar} \sum_m \gamma_m (\hat{J}_m^\dagger \hat{J}_m \rho + \rho \hat{J}_m^\dagger \hat{J}_m - 2\hat{J}_m \rho \hat{J}_m^\dagger). \quad (5.1)$$

¹The Born-Markov approximation was discussed in length in section 3.3 and we will revisit it later on this chapter to justify it in this particular system based on the existence of a dominant frequency scale.

Here ρ describes the density operator of the system, \hat{H}_0 is the Hamiltonian of the closed system, γ_m is the amplitude of the dissipation channel \hat{J}_m that model the dissipation process through the m -th channel. It is interesting to restate that a pure steady state solution of the evolution $\rho_\infty = |\psi_\infty\rangle\langle\psi_\infty|$ should satisfy:

1. $\hat{J}_j |\psi_\infty\rangle = 0 \quad \forall j$: it should be a dark state of the jump operators that represent the different dissipative channels.
2. $\hat{H}_0 |\psi_\infty\rangle = E_\infty |\psi_\infty\rangle$: it should be an eigenstate of the Hermitian Hamiltonian, i.e. a stationary state of the unitary evolution.

As a result, one can easily make use of the properties of the system, such as its symmetries, to prepare the desired state. As we mentioned we want to filter the space symmetries of the system, which are naturally selected by s-wave collisions (two-body losses). The jump operator associated with s-wave collisional losses is given by $\hat{c}_j \equiv \hat{a}_{j\uparrow}\hat{a}_{j\downarrow}$.

However, we aim to consider a preparation that does not require to include losses as in previous proposals (see [58]). In the coming section we will design a jump operators that acts on the same symmetry sector as s-wave collisions but preserve the particle number.

5.2.1.1 Two-site system

First, let us consider a one-dimensional two-component Hubbard model (as described in section 2.4.1) with $N = M = 2$. The choice of fermionic atoms is justified by the connection between spatial and spin symmetries as we already indicated. We consider a jump operator that in the presence of two particles per site causes one of the two species to tunnel to a neighbouring site². We have:

$$\left\{ \begin{array}{l} \hat{H}_0 = -J \sum_{\sigma} (\hat{a}_{L\sigma}^{\dagger} \hat{a}_{R\sigma} + \hat{a}_{R\sigma}^{\dagger} \hat{a}_{L\sigma}) + U \sum_{j=L,R} \hat{n}_{i\uparrow} \hat{n}_{i\downarrow} \\ \hat{J}_j \equiv (\hat{a}_{j+1\uparrow}^{\dagger} + \hat{a}_{j-1\uparrow}^{\dagger}) \hat{a}_{j\downarrow}^{\dagger} \hat{a}_{j\uparrow} \hat{a}_{j\downarrow} \end{array} \right. , \quad (5.2)$$

²We will justify this choice that might seem surprising a priori, as it is a good one-band effective model of the scheme we will propose later on.

where $\hat{n}_{i\sigma} = \hat{a}_{i\sigma}^\dagger \hat{a}_{i\sigma}$, is the number operator on site i of spin σ . Note that in the double well only one of the two directions for the operator \hat{J}_j will be non-zero ($j+1$ for L and $j-1$ for R). Let us analyze our basis states to determine which fulfill the conditions indicated:

1. From the expression of \hat{J}_j we see that all states that have no site multiply occupied, are dark to the jump operators since $\hat{J}_j \propto \hat{a}_{j\uparrow} \hat{a}_{j\downarrow}$, then, the only remaining candidates to be a steady state are the triplet $|t\rangle = \frac{1}{\sqrt{2}} (\hat{a}_{L\uparrow}^\dagger \hat{a}_{R\downarrow}^\dagger - \hat{a}_{R\uparrow}^\dagger \hat{a}_{L\downarrow}^\dagger) |vac\rangle$ and singlet $|s\rangle = \frac{1}{\sqrt{2}} (\hat{a}_{L\uparrow}^\dagger \hat{a}_{R\downarrow}^\dagger + \hat{a}_{R\uparrow}^\dagger \hat{a}_{L\downarrow}^\dagger) |vac\rangle$.
2. However, the second condition is only fulfilled by $|t\rangle$, since:

$$\hat{H}_0 |t\rangle = 0 |t\rangle \quad \text{and} \quad c_j |t\rangle = 0, \quad (5.3)$$

$$\hat{H}_0 |s\rangle = -J(|L\rangle + |R\rangle) \neq E_s |s\rangle \quad \text{with} \quad E_s \in \mathbb{R}, \quad \text{although} \quad \hat{J}_j |s\rangle = 0.$$

As a result, the steady state of the effective model proposed (for the small dimension case) is $|t\rangle$, which corresponds to a completely antisymmetric spatial state, i.e. a completely symmetric spin state. Meanwhile, the singlet state $|s\rangle$ rotates to the other two states with a doublon on site L or R , with the three of them being symmetric in space (spin-antisymmetric).

5.2.1.2 General system sizes

In the case of larger systems, with N particles and M sites, the model of the system remains unchanged:

$$\left\{ \begin{array}{l} \hat{H}_0 = -J \sum_{\langle ij \rangle, \sigma} \hat{a}_{i\sigma}^\dagger \hat{a}_{j\sigma} + U \sum_i \hat{n}_{i\uparrow} \hat{n}_{i\downarrow} \\ \hat{J}_j \equiv (\hat{a}_{j+1\uparrow}^\dagger + \hat{a}_{j-1\uparrow}^\dagger) \hat{a}_{j\downarrow}^\dagger \hat{a}_{j\uparrow} \hat{a}_{j\downarrow} \end{array} \right., \quad (5.4)$$

In the general system size, where we usually analyze the state in terms of local quantities like the site occupations, it is difficult to keep track of the symmetries. In this context, we will need to define new criteria to study if the system has been driven into the desired symmetry sector.

First, let us show that the set of completely spin-symmetric states will be steady states of the open dynamics (in general the steady state will exhibit some spatial degeneracy). A state with a completely spin-symmetric component can be written in the form:

$$|\phi\rangle = |J, J_z\rangle \otimes |\phi_{spa, A}\rangle \quad (5.5)$$

where $|J, 0\rangle$ corresponds to the spin degrees of freedom and $|\phi_{spa, A}\rangle$ to the spatial ones, here A denotes the fact that the spatial state is antisymmetric (global antisymmetry of the wavefunction is required). As far as spin is concerned, we can make use of the properties of angular momentum theories, to build a spin-symmetric state with the constraint of $N_\uparrow = N_\downarrow$. Starting from a trivial spin-symmetric state (all spins with the same z-component), we can act with operators (\hat{J}_\pm) on our state in the following way:

$$\begin{aligned} \uparrow\uparrow\uparrow\uparrow\uparrow &\xrightarrow{\hat{J}^-} \frac{1}{M}(\downarrow\uparrow\uparrow\uparrow\uparrow + \uparrow\downarrow\uparrow\uparrow\uparrow + \dots + \uparrow\uparrow\uparrow\uparrow\downarrow), \\ \left|J = \frac{N}{2}, J_z = +\frac{N}{2}\right\rangle &\xrightarrow{\hat{J}_-} \left|J = \frac{N}{2}, J_z = +\frac{N}{2} - 1\right\rangle. \end{aligned}$$

Then, by starting with a completely polarized state and acting with local operators we can build a state in the $J_z = 0$ manifold, leaving the symmetries unchanged. As a result, the state $|J, 0\rangle$, describes a spin-symmetric state in the fulfilling $N_\uparrow = N_\downarrow$.

On the other hand, we have the spatial component associated to our wavefunction $|\phi_{spa, A}\rangle$. It is important to consider how \hat{H}_0 acts on $|\phi_{spa, A}\rangle$. Let us consider the onsite energy term, which is proportional to the number operators, that is to say, operators that are symmetric under exchange of particles. Thus, any spatial-antisymmetric wavefunction $|\phi_{spa, A}\rangle$ will satisfy

$$U \sum_i^M \hat{n}_{i\uparrow} \hat{n}_{i\downarrow} |\phi_{spa, A}\rangle = 0. \quad (5.6)$$

because of symmetry. Then the only term left to be discussed now is the kinetic one, that we can express in terms of the Fourier modes, according to the following

transformations for the creation and annihilation operators

$$\begin{aligned}\hat{a}_{j\sigma} &= \frac{1}{\sqrt{N}} \sum_k e^{ikaj} \hat{f}_{k\sigma}, & \hat{f}_{k\sigma} &= \frac{1}{\sqrt{N}} \sum_j e^{-ikaj} \hat{a}_{j\sigma}, \\ \hat{a}_{j\sigma}^\dagger &= \frac{1}{\sqrt{N}} \sum_k e^{-ikaj} \hat{f}_{k\sigma}^\dagger, & \hat{f}_{k\sigma}^\dagger &= \frac{1}{\sqrt{N}} \sum_j e^{ikaj} \hat{a}_{j\sigma}^\dagger,\end{aligned}\tag{5.7}$$

where a describes the lattice spacing and the normalizing constant is chosen to fulfill $\sum_j \hat{a}_{j\sigma}^\dagger \hat{a}_{j\sigma} = \sum_k \hat{f}_{k\sigma}^\dagger \hat{f}_{k\sigma} = N$. Then, we can apply the Fourier transform to the kinetic term:

$$\begin{aligned}-J \sum_{\langle ij \rangle, \sigma}^M \hat{a}_{i\sigma}^\dagger \hat{a}_{j\sigma} &= -J/N \sum_{j, \sigma} \sum_{k, q} (e^{iaj(k-q)} \hat{f}_{k\sigma}^\dagger \hat{f}_{q\sigma} e^{iqa} + \text{h.c.}) = \\ &= -J \sum_{\sigma} \sum_k (\hat{f}_{k\sigma}^\dagger \hat{f}_{k\sigma} e^{ika} + \text{h.c.}) = -2J \sum_{k, \sigma}^M \hat{f}_{k\sigma}^\dagger \hat{f}_{k\sigma} \cos(ka).\end{aligned}\tag{5.8}$$

We recover the band structure of the lattice model $-2J \cos(ka)$ where $k \in (-\frac{\pi}{a}, \frac{\pi}{a})$, that is to say, it belongs to the first Brillouin zone. So, the energy shifting simply reflects the fact that the momentum of the particle corresponds to a given value in the lower Bloch band.

Then, any antisymmetric superposition of single-particles states, whose energies are given by Eq.(5.8), constitutes an spatial-antisymmetric state $|\phi_{spa, A}\rangle$. Moreover, this state is by construction an eigenstate of \hat{H}_0 , since, as we mentioned before, the onsite energy term vanishes for antisymmetric states.

As a result, we have only left to show that such a state is dark to the dissipation, i.e. $\hat{J}_j |\phi\rangle = 0$. But this is straightforward since $\hat{J}_j \propto \hat{a}_{j\uparrow} \hat{a}_{j\downarrow}$. Consequently, only states proportional to $\hat{a}_{j\uparrow}^\dagger \hat{a}_{j\downarrow}^\dagger$ will survive and, as no antisymmetric state can be proportional to that term since it implies multiple occupancy in a given site j , we learn that $c_j |\phi_{spa, A}\rangle = 0$.

To sum up, we have shown that:

$$\left. \begin{aligned}\hat{H}_0 |\phi\rangle &= E_\phi |\phi\rangle \\ \hat{J}_j |\phi\rangle &= 0\end{aligned}\right\}.\tag{5.9}$$

That is to say, the set of states of the form

$$|\phi\rangle = |J, 0\rangle \otimes |\phi_{spa,A}\rangle, \quad (5.10)$$

are dark to the dissipative dynamics and also eigenstates of the effective Hamiltonian. Thus, they are steady state solutions of the model shown in Eq.(5.4). The fact that this set of states is in general not unique, and so we do not drive to a pure state, will be important in the following sections. As we will show, this will affect the efficiency of our driving scheme, as the preparation time will be reduced with the increasing size of the dark manifold.

5.3 Proposed scheme

So far we have shown how for fermionic atoms in a single band the manifold of completely spin-symmetric states is dark to the dissipator given by $\hat{J}_j \equiv (\hat{a}_{j+l\uparrow}^\dagger + \hat{a}_{j-l\uparrow}^\dagger)\hat{a}_{j\downarrow}^\dagger\hat{a}_{j\uparrow}\hat{a}_{j\downarrow}$. Now, it is essential to propose how such a jump operator would be implemented. We are going to use a combination of coherent and dissipative driving to do so approximately as a stroboscopic map. Before directly simulating the process we want to show how this scheme produces a steady state with the desired properties.

Let us again consider a one-dimensional two-component Fermi gas, but now we will include the second Bloch band in our description. In this way, we can make use of interband transitions to provide the mechanism for the particle to tunnel a distance l . For the implementation we need:

1. A mechanism to target and excite the spin-symmetric states to a higher Bloch band: for this we use a state and spin-selective Raman transfer.
2. A mechanism for the excited atoms to cool down to the lower Bloch band: we do so through sympathetic cooling (see [12]) of the fermionic species which is embedded in a one-species bosonic system cooled to the BEC state.

A depiction of the proposed scheme is provided in Fig.5.1. In order to target the desired symmetry sector (symmetric under exchange in space) we will tune the

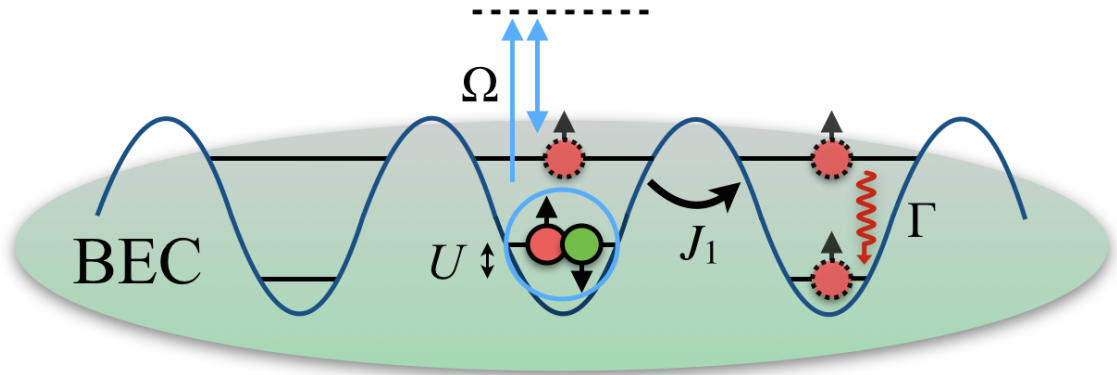


Figure 5.1: Proposed implementation combining a state- and spin-selective Raman transition between lattice bands with amplitude Ω and the coupling to a BEC reservoir with coupling ratio Γ . The transition is resonant with the doubly occupied states with onsite interaction strength U . The tunneling amplitude in the higher band is given by J_1 .

Raman transition to be resonant to the energy of a doubly-occupied site U . Then we can add a polarization-dependent term to separate the higher Bloch band so that only one of the two spin species is transferred and we can avoid the existence of double occupancies (which are in the undesired symmetry sector) in the higher band.

Once the particles are excited to the higher lattice band, they will be sympathetically cooled by a bosonic reservoir. The fermions interact via low-energy collisions with the reservoir, which has an effective $T_{BEC} = 0$ as long as $k_B T_{BEC} \ll \hbar\omega_{10}$, with ω_{10} the transition frequency between band 1 and band 0 and k_B the Boltzmann constant. The typical timescales of the cooling are $\tau_{10} \sim 10 - 100$ KHz (for a Rubidium BEC with scattering length $a \sim 100a_0$, where a_0 is the Bohr Radius, density $\rho \sim 10^{14} \text{ cm}^{-3}$ and trapping frequency $\omega \sim 2\pi \times 10^5 \text{ s}^{-1}$, see [51]). For this procedure to be efficient it is important that this decay time is at the most of the order of the tunneling in the higher band as the scheme requires the particle to displace a certain number of sites before decaying. This condition can be satisfied in the lower limit of τ_{10} .

Through sympathetic cooling, the particle will stochastically decay to the lower Bloch band either in the spin-symmetric or spin-antisymmetric sector. However, we can ensure that as soon as the particle decays to the spin-symmetric state the dynamics

will not rotate the state into a spin-antisymmetric state, and simply by iterating this process of Raman transitions and the reservoir cooling we will drive the system to the dark state manifold. Thus, with this recycling scheme, combining coherent and dissipative driving, we can distillate the desired spin state of the fermions in the optical lattice. Even more importantly, this scheme preserves the number of particles N in the lattice, a major improvement from previous proposals.

Let us discuss now the Hamiltonian describing the system. Under the tight-binding approximation the fermionic system can be modeled through the Hubbard Hamiltonian with two bands:

$$\begin{aligned} \hat{H} = & \sum_{\langle ij \rangle, \sigma, b} J_b \hat{a}_{i\sigma b}^\dagger \hat{a}_{j\sigma b} + \sum_{i, b, b'} U_{bb'} (\hat{n}_{i\uparrow b} \hat{n}_{i\downarrow b'} + \hat{n}_{i\uparrow b'} \hat{n}_{i\downarrow b}) \\ & - \Delta \sum_i \hat{n}_{i\uparrow} - \frac{\Omega}{2} \sum_i (\hat{a}_{i\uparrow 0}^\dagger \hat{a}_{i\uparrow 1} + \hat{a}_{i\uparrow 1}^\dagger \hat{a}_{i\uparrow 0}), \end{aligned} \quad (5.11)$$

where J_0 and J_1 are the tunneling amplitudes in the lower and higher lattice band respectively; U_{00} and U_{11} are the onsite interaction constants and U_{10} the interband interaction one; Δ is the constant of the polarization dependent energy shift for \uparrow -spin in band 1 and Ω is the interband transition ratio modeling the Raman transition. Simply by setting $\Delta = -(U_{10} - U_{00})$ we make the transfer to the higher band resonant for \uparrow -spin.

The only ingredient left in our description is the dissipative coupling to the condensate. We can describe the dynamics of the system coupled to the reservoir, whose density operator is ρ_{tot} , under the Born-Markov approximation, justified by the existence of a single dominant frequency which is the interband transition, ω_{10} (similarly to the approach in [54, 55]). This approximation leads to a master equation of the system reduced density operator $\rho = \text{Tr}_{\text{BEC}}[\rho_{tot}]$:

$$\dot{\rho} = \mathcal{L}\rho = -\frac{i}{\hbar} [\hat{H}, \rho] - \frac{1}{2\hbar} \sum_m \gamma_m (J_m^\dagger J_m \rho + \rho J_m^\dagger J_m - 2J_m \rho J_m^\dagger), \quad (5.12)$$

where $J_m = \hat{a}_{m\uparrow 0}^\dagger \hat{a}_{m\uparrow 1}$ represents the decay of a \uparrow -spin particle from the higher to the lower band on site m and γ_m is the decay amplitude for the m -th dissipation

channel. Numerical solutions to this evolution of the system will be discussed in further sections.

5.3.1 Stroboscopic implementation of the driving scheme

We could consider the dynamics of the system directly through Eq.(6.16) for a fixed value of the system parameters. However, a more efficient implementation can be achieved if we consider an stroboscopic change of the system parameters that exploits the fact that the timescales of the system are strongly separated with the Raman transfer being much faster than the typical decay time through the coupling to the reservoir gas:

1. Transfer to the higher band from a deep lattice:

$$|\phi_1\rangle = e^{-iHT_1} |\phi_0\rangle \quad (5.13)$$

with $\Omega T_1 = \pi$: π -pulse that allow tunnel to upper band. In this step, we increase the lattice depth preventing tunneling inside any of the two bands during the process. The parameters are as follows: $U_{00} = 10J_0$, $U_{11} = U_{00}/2$, $U_{10} = U_{00}/\sqrt{(2)}$, $\Delta = -(U_{00} - U_{10})$ (resonant condition) and $\Omega = \Delta/10$. This could also be implemented through an adiabatic swap, that will present greater robustness.

2. Delocalization in the higher band:

$$|\phi_2\rangle = e^{-iHT_2} |\phi_1\rangle \quad (5.14)$$

with $J_1 T_2 = \frac{\pi}{2}$. The parameters are then $J_0 = 1$, $J_1 = 3$, for varying values of $U_{00} = 0, J_0, 2J_0, \dots$, maintaining $U_{11} = U_{00}/2$, $U_{10} = U_{00}/\sqrt{(2)}$, $\Delta = -(U_{00} - U_{10})$ (resonant condition) and $\Omega = 0$ (no Raman coupling to upper band).

3. Decay through coupling to the reservoir:

$$|\rho_3\rangle = e^{-i\mathcal{L}T_3} |\rho_2\rangle \quad (5.15)$$

with $\gamma_m = \Gamma = J_0$, maintaining the rest of the parameters from step 2 unchanged. Here T_3 is chosen so that essentially all the population on the higher band has been removed, typical values that we consider are $T_3 \sim 10J_0 = 10\gamma_m$. Note that as the dynamics are now open we have represented the vectorized version of the density operator ρ for easier comparison with Eq.(5.13).

We can iterate this process of transfer to the higher band, delocalization and decay over time until we populate the spin-symmetric manifold. Once this occurs, as no part of the wavefunction will be couple to doubly occupied states our state will become dark.

5.4 Steady state characterization and Quantum Fisher Information

The proposed scheme aims to prepare a highly entangled state in spin, that could then be applied for quantum metrology. It is therefore essential to characterize and define a proper measure to assert whether the stationary state of the proposed open system dynamics will have an advantage for metrology.

5.4.1 Bloch Sphere picture and Ramsey spectroscopy

As we mentioned, we are interested in using our preparation scheme as an input state that can then be used for quantum enhanced measurements. A useful way to represent and characterize our state during the dynamics is through the use of an enlarged Bloch Sphere [100]. This representation is commonly used in the context of cold atom interferometry.

In particular, Ramsey spectroscopy experiments with cold atoms [6, 59] have been

performed in recent years beyond classical accessible precision and showing how quantum properties can be exploited to perform extremely precise measurements. In this context, we consider the existence of two atomic states that are the two modes (equivalent to the two arms) of the interferometer and they will be represented as the poles of the Bloch sphere. Then, a superposition of both states is prepared (equivalent to the beam-splitter in traditional interferometry) where the measurement is performed, since the state will acquire a phase ψ proportional to the quantity to be estimated. This is followed by a new mixing of the two-modes closing the interferometry loop. The key point here is the superposition state as if these states satisfies certain properties the sensitivity of the phase estimation $\Delta\psi$ can overcome classical scaling by a factor of N .

In our system, we choose the completely polarized states $|+\rangle = |\uparrow\uparrow\uparrow \dots \uparrow\rangle$ and $|-\rangle = |\downarrow\downarrow\downarrow \dots \downarrow\rangle$, that we introduced in section 5.2.1.2, to be represented by the poles of the sphere, and so, they would correspond to the two-modes of the interferometer. Thus, any state with $N_\uparrow = N_\downarrow$ corresponds to a vector in the equatorial plane and will act as the superposition state that we just described. Consequently, our scheme will prepare a state in the equatorial plane were the measurement will take place. A depiction of the initial state and the dark state manifold is provided in Fig.5.2.

5.4.2 Quantum Fisher Information

We know that for the smallest system size that one can consider ($M = N = 2$) the target state is simply the triplet state $|t\rangle = \frac{1}{\sqrt{2}} (\hat{a}_{L\uparrow}^\dagger \hat{a}_{R\downarrow}^\dagger - \hat{a}_{R\uparrow}^\dagger \hat{a}_{L\downarrow}^\dagger) |vac\rangle$ (see section 5.2.1.1); however, increasing the system size will enlarge the dark-state manifold and so our steady state will not be unique anymore. More specifically, as the system size increases the steady state will present a mixture in the motional degrees of freedom while it remains pure in the spin degrees of freedom (we will analyze this in depth in section 5.5.5). As a result of the lack of uniqueness of our steady state it is difficult to rely on measures such as the state overlap $\langle \phi_{prepared} | \psi_{target} \rangle$ or more generally the state fidelity [100] $F_{\psi,\phi} = \sqrt{\langle \psi_{target} | \rho_{prepared} | \psi_{target} \rangle}$ to determine the success of our preparation scheme. This, together with the fact that we are interested in determining the usefulness of the prepared state, make us introduce the concept of

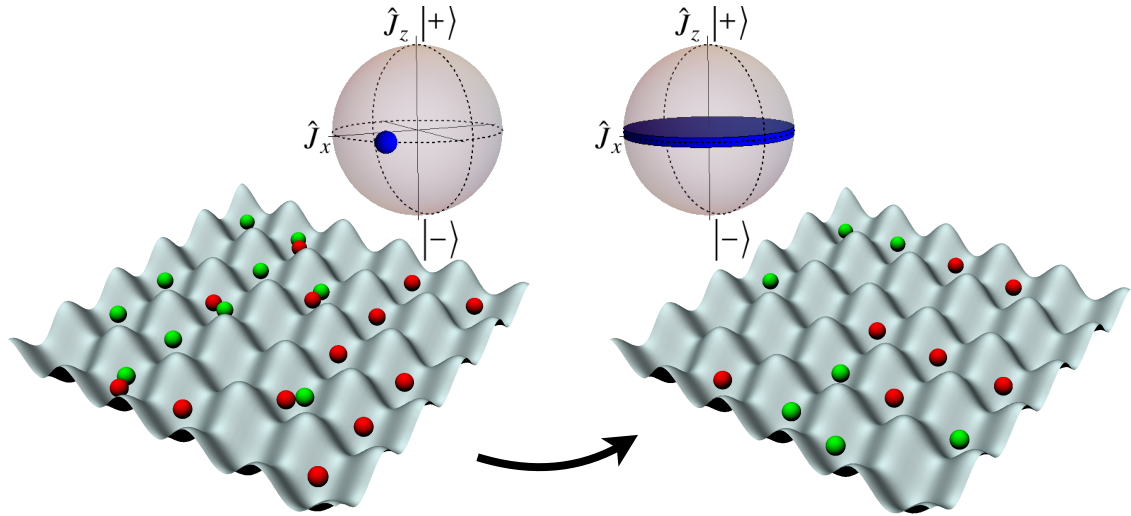


Figure 5.2: Initial (random) state and target manifold configurations with $N_{\uparrow} = N_{\downarrow}$, represented both in the lattice and in the generalized Bloch sphere. The system is driven to a completely spin symmetric state living in the equatorial plane.

Quantum Fisher Information (QFI).

In this section, we present the notion of Quantum Fisher Information [116, 117, 118] denoted as F_Q . This quantity arises from the context of Quantum Estimation Theory. In order to provide a definition for it, the simplest way is to consider the more general concept of Fisher information F .

Let us consider a given state, described by a density operator ρ over which we perform a measurement generated by \hat{G} , so that the state transforms as $\rho(\theta) = e^{-i\theta\hat{G}}\rho e^{i\theta\hat{G}}$ with θ the phase shift that we would like to measure. We can define an estimator $\theta_{est}(\vec{\mu})$ which is a function of the outcomes $\vec{\mu} = \mu_1, \dots, \mu_m$ with m the number of measurements performed. The error associated with this estimator is subject to the Cramer-Rao bound [119, 120]

$$\Delta\theta_{est} \geq 1/\sqrt{mF}, \quad (5.16)$$

where $\Delta\theta_{est}$ is the variance of our estimator. We immediately can infer that a higher

Fisher information would reduce the variance of our estimator and so, it is related to the sensitivity of the state. The classical Fisher Information is given by:

$$F = \sum_{\mu_i} \frac{1}{p(\mu_i|\theta)} \left(\frac{\partial p(\mu_i|\theta)}{\partial \theta} \right)^2, \quad (5.17)$$

with $p(\mu_i|\theta)$ the conditional probability of measuring the value μ_i with the phase shift produced by the transformation being θ . Each measurement is, in fact, a positive operator valued measurement (POVM) with an associated operator \hat{E}_{μ_i} ; thus, the conditional probabilities are related to the Born rule $p(\mu_i|\theta) = \text{Tr}(\rho(\theta)\hat{E}_{\mu_i})$.

By maximizing F over the total set of POVMs we obtain³ the QFI F_Q :

$$F_Q[\rho, \hat{G}] = 2 \sum_{k,k'} \frac{(\alpha_k - \alpha_{k'})^2}{\alpha_k + \alpha_{k'}} |\langle k | \hat{G} | k' \rangle|^2, \quad (5.18)$$

with $\rho = \sum_k \alpha_k |k\rangle \langle k|$ and the sum only including terms that fulfill $\alpha_k + \alpha_{k'} > 0$. Then, we can restate the Cramer-Rao bound as:

$$\Delta\varphi \geq 1/\sqrt{mF} \geq 1/\sqrt{mF_Q}. \quad (5.19)$$

From Eq.(5.18) we can make two observations: firstly, computing F_Q has reduced to computing matrix elements $\langle k | \hat{G} | k' \rangle$ of the generator of the measurement we want to perform; secondly, this expression requires the diagonalisation of the density operator which quickly becomes an expensive computation to perform (it scales as the square of the size of our Hilbert space). Consequently, the system sizes for which the expression in Eq.(5.18) can be computed are rather small due to the exponential growth of the Hilbert space.

Now, to make this computation efficient in our case it is important to consider which type of transformations will take place in our system. The state preparation we propose will then be used in an interferometry scheme, as we discussed in section 5.4.1. In this kind of two-mode interferometers we can consider our transformations as rotations along the generalized Bloch Sphere.

³A careful derivation of the QFI expression from Eq.(5.17) can be found in [121, 117].

If we impose again the condition of $N_\uparrow = N_\downarrow$ (or, equivalently, that our state lies in the equator of the Bloch Sphere with $J_z = 0$) a possible transformation would be a coherent spin-flip from the XY-plane (a tilt of the manifold along the most sensitive direction), for which the generator is a collective spin operator

$$\hat{J}_x = \frac{1}{2} \sum_l (c_{l\uparrow}^\dagger c_{l\downarrow} + \text{h.c.}). \quad (5.20)$$

Hence, in our case

$$F_Q[\rho, \hat{G}] = 2 \sum_{k,k'} \frac{(\alpha_k - \alpha_{k'})^2}{\alpha_k + \alpha_{k'}} |\langle k | \hat{J}_x | k' \rangle|^2. \quad (5.21)$$

We can relate this to the system size scaling in the metrological schemes. Classical states of atoms possess a sensitivity on the phase estimation scaling with $\Delta\theta_{est} \geq 1/\sqrt{mN}$ which corresponds to the Standard Quantum Limit (SQL). However, these can be overcome by the introduction of entanglement in the system up to the Heisenberg scaling [112, 3] with $\Delta\theta_{est} \geq 1/\sqrt{m}N$. Thus, affecting the scaling of QFI [122], from $F_Q \sim N$ for the SQL to $F_Q \sim N^2$ for Heisenberg scaling.

5.4.3 Reduction to the pure state expression for the QFI

As we mentioned computing Eq.(5.18) requires the diagonalisation of the density operator that is computationally unaffordable for many system sizes. However, if the input state is pure $\rho = |\psi\rangle\langle\psi|$ ($\alpha_k = 0 \forall k \neq \psi$), the expression becomes rather simple:

$$\begin{aligned} F_Q &= 2 \sum_{k,k'} \frac{(\alpha_k - \alpha_{k'})^2}{\alpha_k + \alpha_{k'}} |\langle k | \hat{G} | k' \rangle|^2 = \\ &= 2 \sum_{k=\psi, k' \neq k} |\langle k | \hat{G} | k' \rangle|^2 + 2 \sum_{k'=\psi, k \neq k'} |\langle k | \hat{G} | k' \rangle|^2 = \\ &= 4 \sum_{k' \neq \psi} |\langle \psi | \hat{G} | k' \rangle|^2 = 4 \sum_{k' \neq \psi} \langle \psi | \hat{G} | k' \rangle \langle k' | \hat{G} | \psi \rangle = \\ &= 4 \langle \psi | \hat{G} | (I - |\psi\rangle\langle\psi|) | \hat{G} | \psi \rangle = 4 \left(\langle \hat{G}^2 \rangle - \langle \hat{G} \rangle^2 \right) = 4\Delta\hat{G}. \end{aligned} \quad (5.22)$$

There we made use of the identity $I = \sum_{k'} |k'\rangle \langle k'|$. Then, in the case of having a pure state we would only require to compute the expectation value of the variance of an operator ($F_Q = 4\Delta\hat{J}_x$). This is not only a much simpler procedure but also it allows us to exploit the better scaling with system size of quantum trajectories (scaling with the size of the Hilbert space and not the square of it).

This property might seem difficult to exploit as, in general, we will not drive our system to a pure steady state or be pure during the time evolution. Nevertheless, we show that for $N_\uparrow = N_\downarrow$ any rotation generated by \hat{J}_x will project our system out of the $\hat{J}_z = 0$ manifold and in this case, we obtain an expression as simple as Eq.5.22 even in the case of mixed states.

Consider the state of the system described by $\rho = \sum_k \alpha_k |k\rangle \langle k|$, where $\{|k\rangle\}$ forms a complete basis in the Hilbert space \mathcal{H} . Since the order of our basis is arbitrary we can choose it so that $\alpha_k > 0$ for $k < k_0$ and $\alpha_k = 0$ for $k \geq k_0$. From the expression of F_Q :

$$F_Q = 2 \sum_{k,k'} \frac{(\alpha_k - \alpha_{k'})^2}{\alpha_k + \alpha_{k'}} |\langle k | \hat{G} | k' \rangle|^2, \quad (5.23)$$

we can distinguish three different situations:

1. $k, k' \geq k_0$ which is automatically eliminated as we sum over states which satisfy $\alpha_k + \alpha_{k'} > 0$;
2. $k, k' < k_0$ which vanishes in our case, as we explain below;
3. $k \geq k_0, k' < k_0$ or $k' \geq k_0, k < k_0$ which is the one that can be reduced to the pure state expression as we will show now.

First, we have to show that 2. does not contribute to the F_Q in our specific model. As we impose the condition of $N_\uparrow = N_\downarrow$ and we restrict our dynamics to the equator of the Bloch sphere we know that any state contributing to ρ (corresponding to $k < k_0$) has a well-defined number of each spin $N_\uparrow^{[k]} = N_\downarrow^{[k]} = N/2$ with N the total particle number. Then, if both k, k' belong to the equator as the generator $\hat{J}_x = \hat{J}_+ + \hat{J}_-$ does not conserve the spin number, any term of the form $|\langle k | \hat{J}_\pm | k' \rangle|$ will vanish if both k and k' have the same N_\uparrow and N_\downarrow .

Then, the only terms left to consider are the ones in 3. corresponding to $k \geq k_0, k' < k_0$ or $k' \geq k_0, k < k_0$:

$$\begin{aligned}
 F_Q &= 2 \sum_{k,k'} \frac{(\alpha_k - \alpha_{k'})^2}{\alpha_k + \alpha_{k'}} |\langle k | \hat{J}_x | k' \rangle|^2 = \\
 &= 2 \left(\sum_{\substack{k,k' \\ k < k_0}} \alpha_k |\langle k | \hat{J}_x | k' \rangle|^2 + \sum_{\substack{k,k' \\ k' < k_0}} \alpha_{k'} |\langle k | \hat{J}_x | k' \rangle|^2 \right) = \\
 &= 2 \left(\sum_{\substack{k,k' \\ k < k_0}} \alpha_k |\langle k | \hat{J}_x | k' \rangle|^2 + \sum_{\substack{k',k \\ k' < k_0}} \alpha_k |\langle k' | \hat{J}_x | k \rangle|^2 \right) = \tag{5.24} \\
 &= 4 \sum_{\substack{k,k' \\ k < k_0}} \alpha_k |\langle k | \hat{J}_x | k' \rangle|^2 = 4 \sum_{\substack{k,k' \\ k < k_0}} \alpha_k \langle k | \hat{J}_x | k' \rangle \langle k' | \hat{J}_x | k \rangle = \\
 &= 4 \text{Tr} \left(\hat{J}_x \rho \hat{J}_x \right) = 4 \text{Tr} \left(\rho \hat{J}_x^2 \right).
 \end{aligned}$$

The expression is similar to the pure state case for the choice of the generator \hat{J}_x , but misses the contribution of the $\langle \hat{J}_x \rangle^2$ term as this is zero for any state on the equator of the Bloch sphere.

As an example of this, we show in Fig.5.3 the ratio between $\text{Tr}(\rho \hat{J}_x^2)$ and the QFI computed from the complete expression given by Eq.(5.21). We compare both expressions for different example states with mixtures along or outside the equator. The results show clearly how mixedness along the equator does not prevent the F_Q from saturating the pure state expression $4(\Delta \hat{G})^2$.

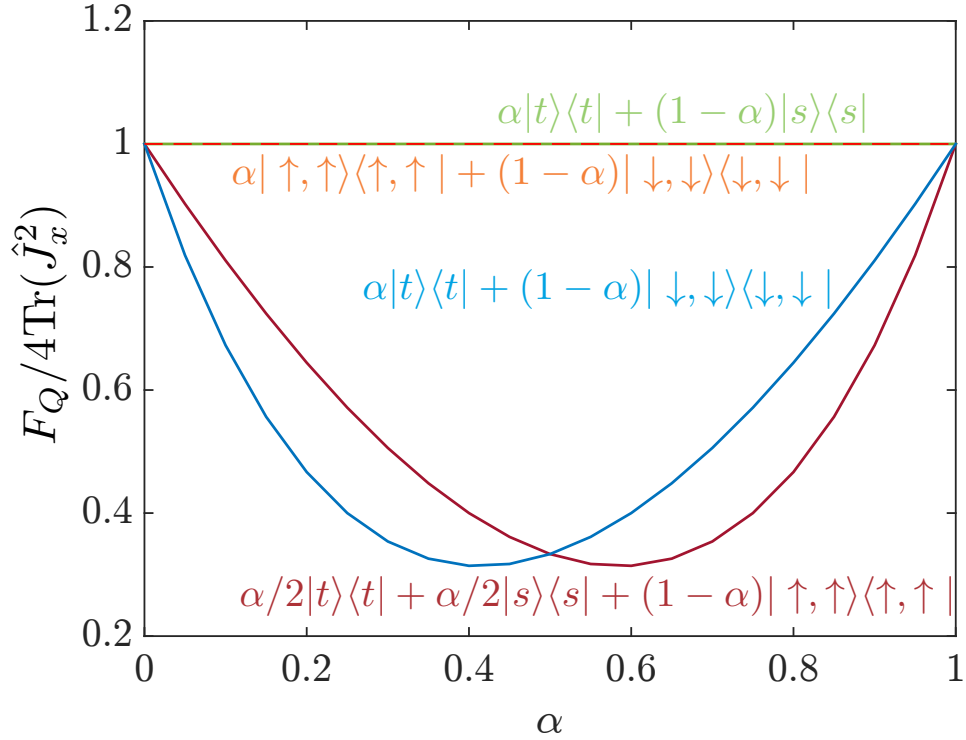


Figure 5.3: Ratio between QFI for a mixed and pure state for different mixtures of states inside and outside the equatorial plane ($N_\uparrow = N_\downarrow$).

5.4.4 Relation between angular momentum and QFI

We already mentioned that if the state prepared scales beyond classical sensitivity then $F_Q \sim N^2$. Making use of angular momentum theory we can predict the saturation value for $\text{Tr}(\rho \hat{J}_x^2)$ and how it will scale with the system size N . Given our generator:

$$\hat{J}_x = \frac{1}{2} \sum_l (\hat{a}_{l\uparrow}^\dagger \hat{a}_{l\downarrow} + \text{h.c.}). \quad (5.25)$$

As we already mentioned in section 5.2.1.2, we can define the spin component of the completely spin-symmetric state wavefunction as:

$$|J, J_z\rangle \rightarrow |J, 0\rangle \quad (J_z = 0). \quad (5.26)$$

Therefore, it is only left to calculate:

$$\langle J, 0 | \hat{J}_x^2 | J, 0 \rangle = \langle J, 0 | \left(\frac{1}{2} (\hat{J}_+ + \hat{J}_-) \right)^2 | J, 0 \rangle, \quad (5.27)$$

with the angular momentum eigenstates satisfying:

$$\left. \begin{aligned} \hat{J}^2 | J, 0 \rangle &= J(J+1) | J, 0 \rangle \\ \hat{J}_z | J, 0 \rangle &= J_z | J, 0 \rangle \\ \hat{J}_\pm | J, 0 \rangle &= \sqrt{J(J+1)} | J, 0 \rangle \end{aligned} \right\}. \quad (5.28)$$

So,

$$\begin{aligned} \langle J, 0 | \left(\frac{1}{2} (J_+ + J_-) \right)^2 | J, 0 \rangle &= \frac{1}{4} (\langle J, 0 | J_+ J_- | J, 0 \rangle + \langle J, 0 | J_- J_+ | J, 0 \rangle) + \\ &+ \frac{1}{4} (\langle J, 0 | J_+^2 | J, 0 \rangle + \langle J, 0 | J_-^2 | J, 0 \rangle) = \frac{1}{4} (\langle J, 0 | J_+ J_- | J, 0 \rangle + \langle J, 0 | J_- J_+ | J, 0 \rangle) = \\ &= \frac{1}{4} (\langle J, 0 | J(J+1) | J, 0 \rangle \langle J, 0 | J(J+1) | J, 0 \rangle) = \frac{1}{2} J(J+1). \end{aligned} \quad (5.29)$$

For N spin- $\frac{1}{2}$ particles, we have $J = N/2$:

$$\Delta J_x^2 |_{J_z=0} = \langle J, 0 | J_x^2 | J, 0 \rangle = \frac{1}{2} J(J+1) = \frac{N}{4} \left(\frac{N}{2} + 1 \right). \quad (5.30)$$

Finally, we obtain:

$$F_Q = N \left(\frac{N}{2} + 1 \right). \quad (5.31)$$

So we can conclude that if we successfully drive the system to a completely spin-symmetric state, we will obtain a sensitivity in our phase estimation scaling with N^2 and so, our system will show a sensitivity beyond the SQL.

5.5 Numerical results

In this section, we will describe the results we obtained from our numerical simulations of the open system dynamics making use of the Monte Carlo Wavefunction Method (see section 3.3.2). The main reason for the choice of this method is the fact that we do not require the computational cost associated with calculating the density operator, whose scaling is the square of the dimension of the Hilbert space. This method, however, requires averaging over stochastic trajectories of pure states.

We will discuss different regimes and dependences with system parameters. In particular, we will focus on the effect of the onsite interaction on the cooling step, how the filling factor affects the efficiency of the driving process and also the robustness of the method against some experimental imperfections. Finally, we will analyze the purity of the state during the process and how it affects its efficiency.

5.5.1 Dependence on the onsite interaction

As we discussed in section 5.3.1, we will stroboscopically modify some of the system parameters during the preparation scheme. In particular, we will start with a depth lattice and a large onsite interaction compared to J_0 . However, during the delocalizing and cooling steps the lattice will be shallower and the interaction energy smaller. The first study we address consist in analyzing how this onsite interaction – small but in principle finite – affects the driving of the system during the cooling step.

In Fig.5.4 we present the QFI evolution as the stroboscopic driving is iterated over time. We present the values for a varying onsite interaction U_{00} on the cooling step while maintaining it fixed at $U_{00} = 10J_0$ during the driving to the higher Bloch band. We see that increasing the value of the onsite interaction decreases the speed at which the system approaches the steady state but only in a distinguishable manner when reaching values of the order of $U_{00} \sim 3J_0$. The main message to extract from this analysis is that, as long as we remain in the moderate onsite interaction regime, small differences in the value of U_{00} will have small impact in the timescales of the drive or in the steady value obtained (see inset of Fig.5.4). Then, we can choose an intermediate value that in our case it will be $U_{00} = 2J_0$ (observing high values of

F_Q at rather short times) and assume that the system is quite robust if the value is slightly different.

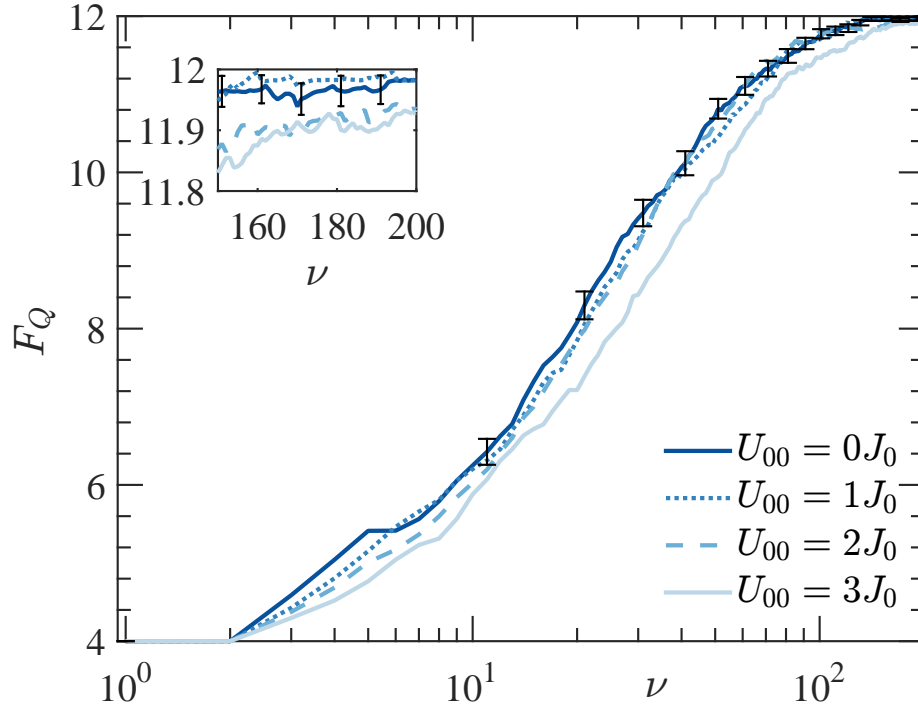


Figure 5.4: (a) Evolution of the QFI as the process of excitation to the higher band and decay is iterated ν times for a system with $N = 4$, $M = 6$, $J_1 = 3J_0$, $U_{00} = 2J_0$ for the cooling step ($U_{00} = 10J_0$ for the transfer to the higher band), $U_{10} = U_{00}/\sqrt{2}$, $\Delta = U_{10} - U_{00}$, $\Omega = \Delta/10$, $\Gamma = J_0$. Here, the time per iteration $\tau_\nu = \Pi/\Omega + (10\gamma)^{-1} \sim (10/J_0)$. Every line corresponds to the average over 100 trajectories, with associated errorbars included only for one curve as they are comparable for the rest. We observe that QFI approaches its maximum value $F_Q = 4\Delta\hat{J}_x = N(N/2 + 1)$. Varying the value of the onsite interaction during the cooling process affects the efficiency of the process but differences are rather small before reaching $U_{00} = 3J_0$ where we observe that the timescales at which we reach the steady state become slower. Inset: same as (a) for the last 50 iterations of the process, here we observe that all the saturating values are close to the maximum F_Q but are slightly reduced for non-zero values of U_{00} .

5.5.2 Filling factor dependence of the dissipative driving

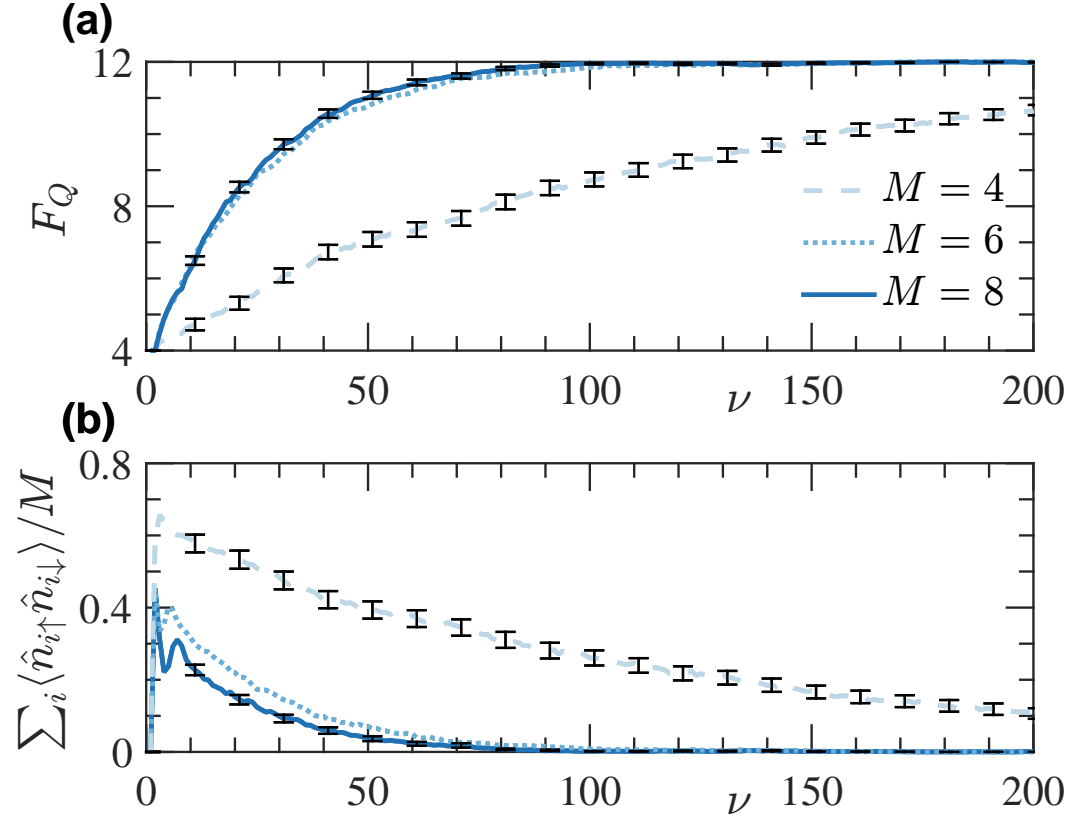


Figure 5.5: (a) Evolution of the QFI as the process of excitation and decay is iterated ν times for a system with $N = 4$, $J_1 = 3J_0$, $U_{00} = 2J_0$ for the cooling step ($U_{00} = 10J_0$ for the transfer to the higher band), $U_{10} = U_{00}/\sqrt{2}$, $\Delta = U_{10} - U_{00}$, $\Omega = \Delta/10$, $\Gamma = J_0$. Here, the time per iteration $\tau_\nu = \Pi/\Omega + (10\gamma)^{-1} \sim (10/J_0)$. Every line corresponds to an average over 500 trajectories with associated errorbars (errorbars for $M = 6$ are similar to the case of $M = 8$ and are not displayed for better visualization). The QFI saturates to the maximum possible value given by $F_Q = 4\Delta\hat{J}_x = N(N/2 + 1)$. Commensurate filling effects reduce the efficiency of the process as doublons are more likely to form during decay from higher band when the occupation in the lower band is higher. (b) Same as (a) but analyzing the double-occupancy in the lower band $\sum_i \langle \hat{n}_{i\uparrow} \hat{n}_{i\downarrow} \rangle / M$.

The second analysis that we will perform is related to the filling factor. A priori, this is expected to have a big impact in the process. On the one hand, we know that any filling factor corresponding to more than one particle per site would force

any configuration to have at least a doubly-occupied site (making it impossible for the system to reach a completely spin-symmetric state). Consequently, we will focus on filling factors $n \leq 1$, with $n = \sum_i \langle \hat{n}_{i\uparrow 0} \rangle / M$. On the other hand, it is clear that low fillings will immediately provide low multiply-occupancy population, however, it will be more difficult for particles to entangle to each other and for triplets in that case and so the F_Q might saturate slower. It is also important to consider that our sensitivity scales with N and so, it is positive to maintain n relatively high.

In Fig.5.5 we study the influence of the filling factor on the efficiency of our scheme. As predicted, for a fixed number of atoms increasing the lattice length has a positive effect on the timescales although it will not affect the saturation values.

This effect is specially dramatic in the case of $N = M$ (commensurate filling) where we observe a much slower growth towards the steady state, and so, to the saturation of F_Q that occurs outside the simulated times. This is better understood in section 5.5.5 where we indicate the fact that the steady state becomes pure for the case of $N = M$. However, we can understand it simply by considering the fact that when the atom decays from the higher Bloch band in the case of unit filling, the probability for the site to be already occupied by another atom is higher and so is the probability of creating a doublon after decaying. Consequently, the target region in the Hilbert space becomes narrower and our driving slower. Meanwhile, for $N < M$ the symmetry sector we target is larger and the driving becomes more efficient.

We can observe similar signatures if we analyze the multiple occupancies in the lattice (Fig.5.5b). As the system is driven to the completely-symmetric state all the population of doublons disappears, this decrease is slower again in the case of commensurate filling as the driving becomes less efficient.

We can conclude from this analysis that filling factor $n \lesssim 1$ are the most efficient as they provide the best trade-off between preparation timescales and sensitivity (which is proportional to N).

5.5.3 Spatial inhomogeneities: magnetic field gradient

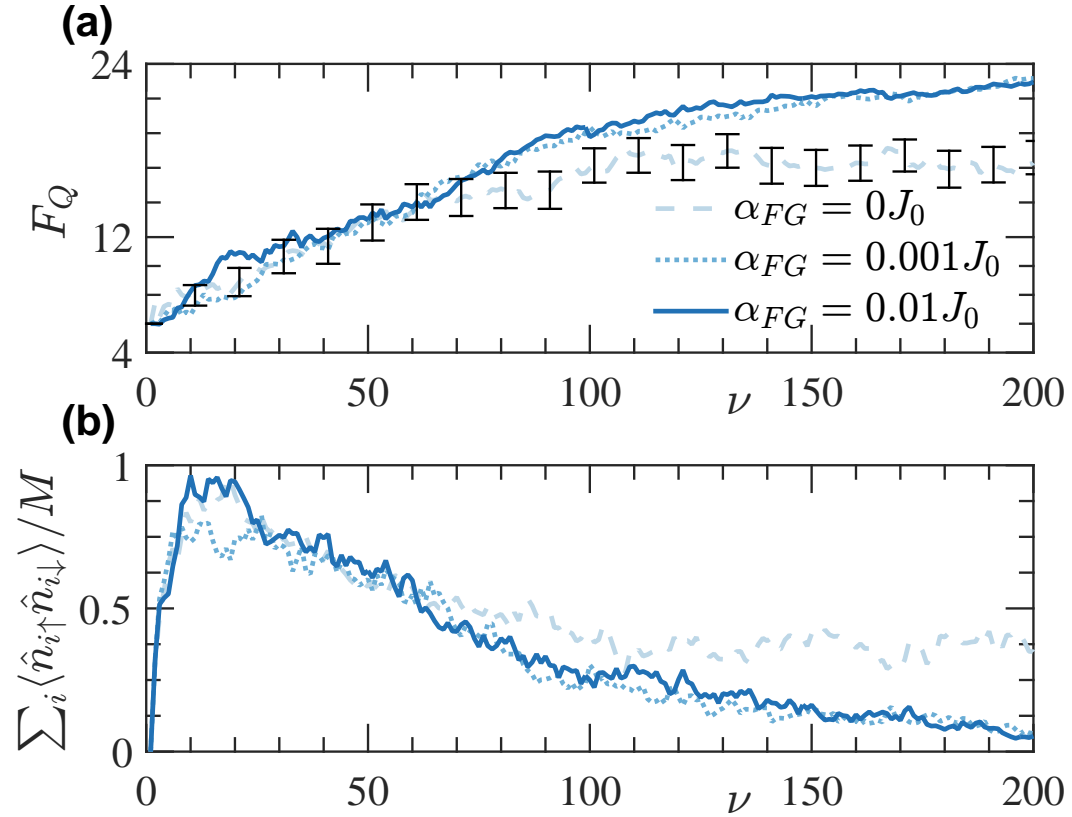


Figure 5.6: (a) Evolution of the QFI as the process of excitation and decay is iterated ν times for a system with $M = N = 6$, $J_1 = 3J_0$, $U_{00} = 2J_0$ for the cooling step ($U_{00} = 10J_0$ for the transfer to the higher band), $U_{10} = U_{00}/\sqrt{2}$, $\Delta = U_{10} - U_{00}$, $\Omega = \Delta/10$, $\Gamma = J_0$ in the presence of a local magnetic field gradient of amplitude α_{FG} . Here, the time per iteration $\tau_\nu = \Pi/\Omega + (10\gamma)^{-1} \sim (10/J_0)$. Every line corresponds to the average over 200 trajectories with the corresponding errorbars. We observe how the QFI increases even in the presence of a small field gradient only failing to saturate for the case of $\alpha_{FG} = 0.01J_0$. (b) Same as (a) for $\sum_i \langle \hat{n}_{i\uparrow} \hat{n}_{i\downarrow} \rangle / M$. The scheme is robust to small values of the gradient ($\alpha_{FG} = 0.001J_0$). All errorbars are of the order of the ones shown, the rest have been removed to allow for better visualization of the profiles.

It is essential to test the robustness of the method against spatial imperfections which can couple the two spin-symmetry sectors. For example, space inhomogeneity could lead to a coupling of the symmetric and antisymmetric states which is undesired.

In this section, we analyze the robustness of the driving scheme against spatial imperfections in the system. In particular, we consider the presence of a field gradient in the lattice of the form $\sum_{i,b}^M \epsilon_{i\uparrow b} \hat{n}_{i\uparrow b}$ where the local energy shift is given by $\epsilon_{i\uparrow b} = \alpha_{FG}(i - M/2)$. Note that in the results discussed here we only include a field gradient of this form, however, different profiles of the magnetic field were investigated and the results were qualitatively equivalent to those included here.

In Fig.5.6 we present the QFI and double occupancies profiles in the presence of a magnetic field gradient with varying local strength α_{FG} , small field gradient values do not affect the profiles (differences within error intervals). However, if the gradient per site is of the order of $\alpha_{FG} = 0.01J_0$ after a transient time, both quantities remain approximately constant. This due to the competing effects of our driving scheme with the symmetry recombination that the spatial imperfection produces.

It is important to understand what realistic values for α_{FG} would be in an experimental implementation. Thus, we can determine if the scheme is robust or not in realistic conditions. In order to do so, let us consider that our spin states \uparrow, \downarrow belong to the 1S_0 manifold of ^{87}Sr . This choice is related with the fact that, in the ground state manifold, both the orbital angular momentum and the electron spin are zero. Thus, only nuclear spin contributes, which scales with μ_N , so-called nuclear magneton, instead of the Bohr magneton $\mu_B \sim 1000\mu_N$. As a result, with this choice we immediately obtain a three order of magnitude advantage against uncontrolled magnetic fields.

We can estimate the field gradient tolerance between neighbour sites as $\Delta\epsilon_{i,i+1} = \mu_N m_I \alpha_{FG} \sim 0.001J_0$, where m_I is the angular momentum projection of the chosen hyperfine states (we propose to use 9/2 and 7/2). Thus, the field gradient should satisfy $\alpha_{FG} \lesssim 500 \text{ mG/mm}$, for a typical lattice distance of $a \sim \mu\text{m}$ this will correspond to $\alpha_{FG} \lesssim 0.5 \text{ mG/site}$, a value that is currently accessible in most cold gas experiments.

5.5.4 Average steady values

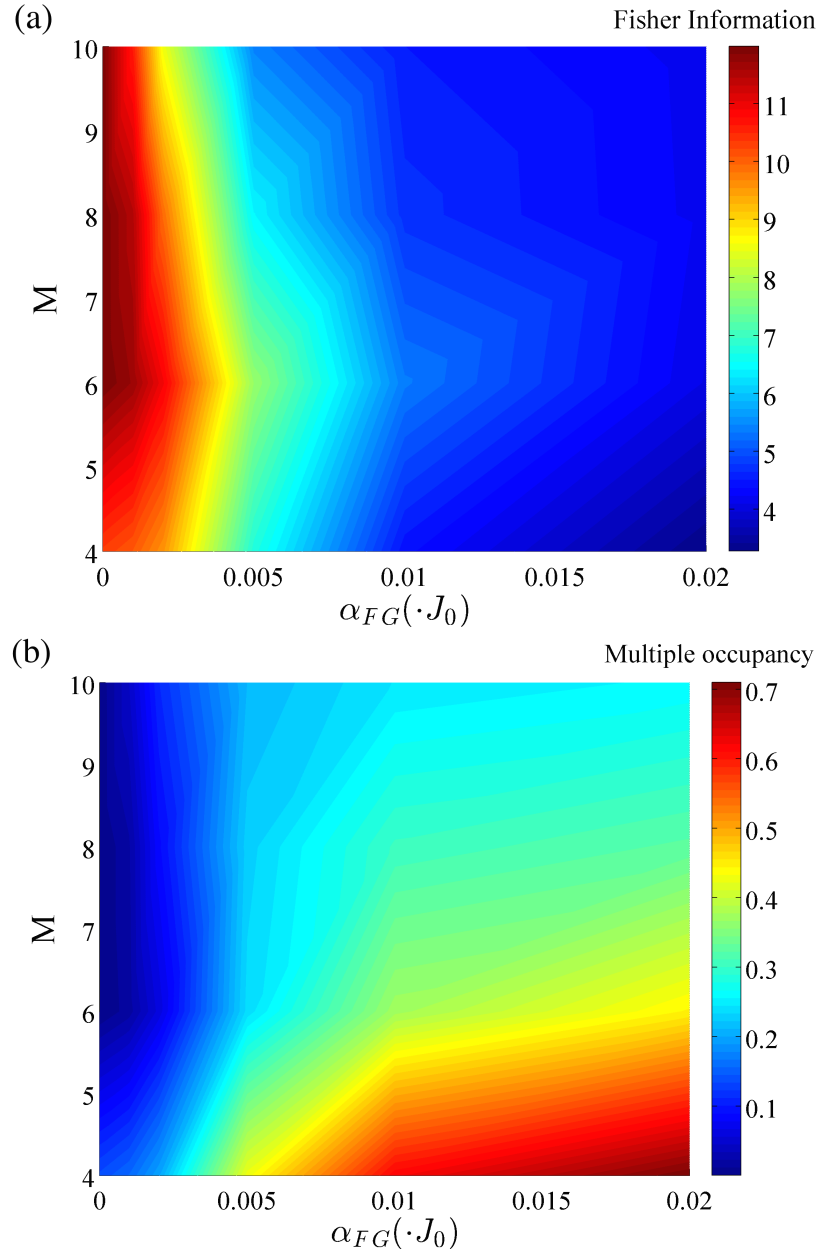


Figure 5.7: (a) QFI averaged over the final 50 iterations of the loop process, when 200 loops were performed; (b) Multiple occupancy proportion in the final state of the system averaged over the final 50 iterations of the loop process. The system size is $N = 4$, different sizes of the lattice and values of the field gradient are explored. The results correspond to the average of 500 trajectories. The result correspond to a system with $J_1 = 3J_0$, $U_{00} = 2J_0$ for the cooling step ($U_{00} = 10J_0$ for the transfer to the higher band), $U_{10} = U_{00}/\sqrt{2}$, $\Delta = U_{10} - U_{00}$, $\Omega = \Delta/10$, $\Gamma = J_0$ in the presence of a local magnetic field gradient of amplitude α_{FG} .

An alternative approach to the previous studies is to consider a fixed number of iterations and study how the final average value of the interesting quantities: the QFI that reflects the utility of the state for metrology and the multiple occupancy that reflex the presence of the undesired symmetry sector,; and how the filling factor and the spatial imperfections such as the field gradient affect them.

In Fig.5.7, we include both the effects of the lattice size and the field gradient on the average final state quantities. On the one hand, we observe that commensurate filling reduces the efficiency of the process and thus for the timescales considered, neither the QFI saturates nor does the multiple occupancy vanish completely. On the other hand, as we increase the field gradient the saturating value of QFI decreases considerably. It is important to remember that for the proposed realization with ^{87}Sr , typical values of the field gradient will remain on the left part of the diagram. We can easily observe how for the case of $M = 6$ that corresponds to the already mentioned $n \lesssim 1$ regime the results are more robust to the presence of the field gradient as the driving has its maximum efficiency with this filling factor.

5.5.5 State purity analysis

When analyzing the efficiency of the dissipative driving in section 5.5.2, we observed that commensurate filling has a detrimental effect on the timescales of the preparation; this can be understood by the fact that higher filling increases the probability of doubly occupied sites in the lattice. However, this is not the only reason why the case $N = M$ is particularly interesting. Specifically, in this section we identified that the timescales of the state distillation are also affected by the purity of the target state.

In Fig.5.8 we compare the overall purity with the spin purity for two filling factors. Due to the choice of an initial random configuration fixing $N_{\uparrow} = N_{\downarrow}$, the initial state is pure in spin but has a high mixture in the motional degrees of freedom. Away from half filling, the overall purity remains almost unchanged and highly mixed for the motional modes, while the spin state becomes rapidly pure as the dynamics converge towards the steady state. Nevertheless, in commensurate filling where the possible

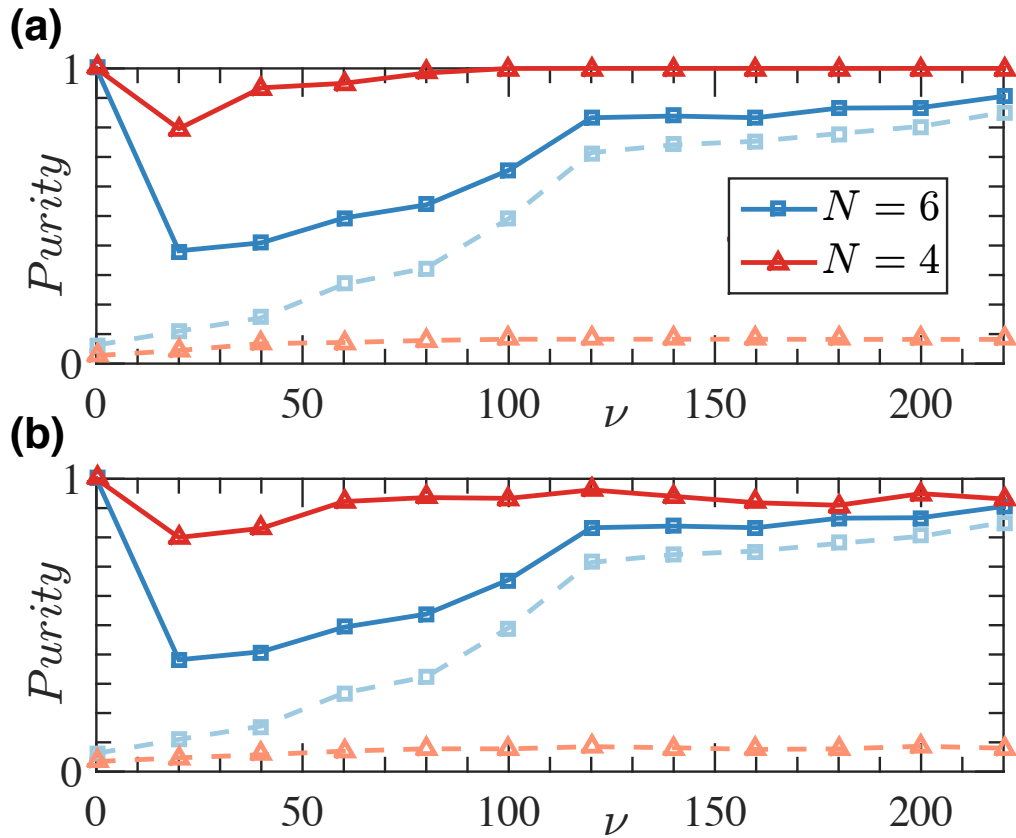


Figure 5.8: (a) Purity of the density operator (dashed lines) and purity of the reduced density operator in spin (solid lines) as the process of excitation and decay is iterated ν times for a system with $M = 6$, $J_1 = 3J_0$, $U_{00} = 2J_0$, $U_{10} = U_{00}/\sqrt{2}$, $\Delta = U_{10} - U_{00}$, $\Omega = \Delta/10$, $\Gamma = J_0$. Here, the time per iteration $\tau_\nu \sim 3 - 4J_0$. Every line correspond to the average over 50 trajectories. After starting from a random configuration the spin state becomes pure as the system reaches its steady state, while the overall state remains highly mixed due to the coupling to different motional modes. Only in the case of commensurate filling were the accessible motional modes for a single spin state are reduced, we observe an increase in the overall purity. (b) Same as (a) including a field gradient term ($\alpha_{FG} = 0.01J_0$), the presence of the field gradient limits the purity in spin of the steady state in a similar manner to the QFI, as the target state is not completely saturated. Apart from this the effect of the field gradient is quite small in the evolution of the purity.

motional modes are fewer we observe both the spin and the overall state to converge towards a pure state. This provides another reason for the driving to be less efficient as the target manifold narrows down. Moreover, the presence of the field gradient (Fig.5.8b) does not affect in great degree the purity profiles, even though it prevents the steady state to become completely pure and it remains mixed both in the global and the spin purity. Note that this effect is small since we are considering a large field gradient (one order of magnitude higher than the tolerated value for the proposed setup with ^{87}Sr).

5.6 Conclusion

In this chapter, we have proposed an scheme, based on coherent and dissipative driving, that filters the spin symmetry for cold fermions in an optical lattice. A completely spin-symmetric state is prepared based on a combination of state-selective Raman transfer and sympathetic cooling with a bosonic reservoir gas. It is important to mention again that previous proposals required collisional losses in order to prepare the state and we have overcome this requirement with the current proposal.

Moreover, we applied the notion of Quantum Fisher Information and analyzed the sensitivity of the prepared state in an interferometric scheme, identifying the parameter regimes where the entanglement generated in the state will produce an advantage over classical states gaining a factor of N in the best scenarios. We have studied the robustness of the state against system imperfections such as a magnetic field gradient. We have shown that for realistic experimental parameters, we are able to efficiently drive the system to the desired symmetry sector.

On the other hand, it is important to consider that we have only included relatively small system sizes and so it is relevant to estimate the scaling of the scheme with the system size towards experimental particle numbers. This is an ongoing work where we make use of density matrix renormalization group (DMRG) techniques, in particular we compute the time evolution of the system through the Time-Dependent Variational Principle (TDVP) technique [123]. It is most efficient to then to simulate the effective one-band model described by Eq.(5.4), which will help us to confirm

the scaling of the timescales with N .

Finally, another possible improvement of the scheme is related to the inclusion of the reservoir gas which poses certain experimental complications. We are currently exploring the possibility of designing a full-optical scheme where we also optically generate the decay from the higher Bloch band using Raman sideband cooling [124]. This method, however, could induce light-assisted collisions in the system if the atom decays to an already occupied site and so we could lose a certain portion of our population with this procedure. Alternatively, we also consider the possibility of driving the system to metastable states. In this case the delocalization would take place in the atoms in the lower band and not by the excited atom. We consider the latter as the most promising future direction for implementation.

Chapter 6

Particle statistics and dynamics with loss of ultracold atoms in optical lattices

6.1 Introduction

In this chapter, we include and discuss in depth the findings that we published in [125] related to the role of particle statistics in dynamics with atom losses in optical lattices.

Current technology in quantum gas microscopes [126, 12, 127] has allowed us to study cold atomic systems, both with bosonic and fermionic atoms, in low dimensions. In 1D, despite the different particle statistics, both systems share many of their dynamical and equilibrium properties as we can formally describe through a Jordan-Wigner transformation [83]. In this chapter, we investigate to what extent the addition of dissipation to the system can produce measurable differences between spinless fermions and hard-core bosons (HCBs) which under most circumstances have identical local properties in 1D in the closed system scenario. In particular, we investigate the role of particle loss in distinguishing the particle exchange statistics, identifying deterministic and probabilistic signatures of dynamical differences in terms of local quantities that are accessible with quantum gas microscopes.

Experiments with cold atoms involving optical lattices were originally focused on the engineering of Hamiltonian dynamics in closed systems focusing towards quantum simulation problems [1, 128]. However, an important aspect of the system is that we have access to the same level of microscopic understanding for most of the dominant forms of dissipation that occur naturally in experiments, developing models which can be derived from first principles under well-controlled approximations. In this chapter we focus on two forms of dissipation, single atom loss [129] and dephasing due to inelastic light-scattering [130, 131]. We study these sources of dissipation aiming not only to improve the realistic description of experimental conditions but also to use them (i) in probing many-body states and their dynamics [132, 133], (ii) in the controlled preparation of interesting many-body states [132, 134], and (iii) in understanding how signatures of fundamental effects from closed systems (e.g., many-body localization (MBL)) survive in the presence of coupling to an environment [135, 136, 137, 138, 139].

Furthermore, we make use particle-number conservation in tensor-network-based numerical methods (see section 4.1.6) to efficiently compute the dynamics of example systems for typical experimental sizes and parameter scales in the presence of loss. We include deterministic forms of dissipation when losses are produced on demand and also we employ a quantum trajectory approach [46, 47, 92] to determine features of HCBs and spinless fermions that survive in the presence of stochastic losses and, potentially, with other sources of dissipation.

This chapter is structured as follows: in Sec.6.2 we discuss the similarities in the theoretical description of spinless fermions and HCBs in one dimension, formalizing it through a Jordan-Wigner transformation. In Sec.6.3 we include the analysis of the differences for the two particle statistics in the context of losses being induced on demand in an experiment. In Sec.6.4 we investigate how the previous results are modified when the losses occur in an stochastic scenario and how realistic imperfections could affect our ability to distinguish particle statistics via local measurements. Finally, in Sec.5.6 we discuss our findings and point out some future directions opened by our work.

6.2 Similarities of spinless fermions and hard-core bosons

As mentioned, in this chapter we investigate the dynamics of spinless fermions and HCBs allowed to move in one direction while tightly confined in the other two directions. In chapter 2, we discussed that the study of one-dimensional (1D) systems is one of the essential ingredients for the current theoretical understanding of ultracold atoms; this is due to the fact that many of our numerical tools can simulate comparable system sizes, parameter regimes and timescales to experiments in 1D, while this remains in many cases inaccessible for higher dimensional systems.

These systems, where fermions and bosons behave similarly [140], have been realized with cold bosonic atoms in strongly confined 1D tubes [141], and in lattices [8, 142], and the consequences can be seen clearly, even for just two atoms, in quantum gas microscope experiments [143].

This similarity between HCB and fermions on a lattice can be formally addressed using a Jordan-Wigner transformation to spin operators [83] (for a full description of the Jordan-Wigner transformation, see section 2.4.1.1). Note that other general Bose-Fermi maps exist [140], for example in the case of contact interaction [144].

As a starting point, we can obtain the Hamiltonian describing HCBs in one-dimension as a limiting case of the Bose Hubbard model we discussed in section 2.4.2 ($\hbar \equiv 1$)

$$\hat{H} = -J \sum_i^{M-1} (\hat{b}_i^\dagger \hat{b}_{i+1} + \text{h.c.}) + \frac{U}{2} \sum_i^M (\hat{n}_{b,i} (\hat{n}_{b,i} - 1)) , \quad (6.1)$$

where the operator $\hat{b}_i^{(\dagger)}$ annihilates (creates) a bosonic particle on site i , $\hat{n}_{b,i} = \hat{b}_i^\dagger \hat{b}_i$ is the bosonic number operator of the site $i \in [1, M]$, M is the lattice system size, J is the tunneling amplitude in the lattice and U is the on-site interaction. The bosonic

operators obey the following commutation rules¹,

$$[\hat{b}_i^{(\dagger)}, \hat{b}_j^{(\dagger)}] = 0; [\hat{b}_i, \hat{b}_j^\dagger] = \delta_{i,j}. \quad (6.2)$$

If we consider the case of $U \rightarrow \infty$ then for low energies, the probability of configurations with several atoms on a single site is negligible and so we can add the constraint of $\hat{n}_{b,i} \in [0, 1]$ or $\hat{b}_i^2 \equiv 0$, hence, representing HCBs with this model.

After imposing these constraints we are left with a tight-binding model of the form

$$\hat{H} = -J \sum_i^{M-1} (\hat{b}_i^\dagger \hat{b}_{i+1} + \text{h.c.}), \quad \hat{b}_i^2 \equiv 0, \quad (6.3)$$

where the only contribution is related to the tunneling to neighbouring sites.

Similarly, for spinless fermions in the lowest Bloch band of the optical lattice, the system is well described as well by a tight-binding Hamiltonian,

$$\hat{H} = -J \sum_i^{M-1} (\hat{a}_i^\dagger \hat{a}_{i+1} + \text{h.c.}), \quad (6.4)$$

where the operator $\hat{a}_i^{(\dagger)}$ annihilates (creates) a fermionic particle on the site i with $\hat{n}_{a,i} = \hat{a}_i^\dagger \hat{a}_i \in [0, 1]$ is the fermionic number operator of the site i , and J is the tunneling amplitude in the lattice. The fermionic operators obey the usual anticommutation rules,

$$\{\hat{a}_i^{(\dagger)}, \hat{a}_j^{(\dagger)}\} = 0; \{\hat{a}_i, \hat{a}_j^\dagger\} = \delta_{i,j}. \quad (6.5)$$

As we mentioned before the similarity between HCB and spinless fermions can be formalized via a Jordan-Wigner transformation for both particle types into spin operators.

On the one hand, for bosons the mapping is rather simple since we have a direct

¹Note that in the literature the commutation relations of HCBs are usually given by $[b_i, b_j^\dagger] = (1 - 2n_i)\delta_{ij}$. However, we choose to use the standard bosonic ones adding the limit of infinite interactions (implying $\hat{b}_i^2 \equiv 0$) since they are computationally equivalent and we will explore the limit of large but finite interaction in bosons.

correspondence between a site with occupation 0 or 1 and the two states of a spin-1/2 particle. The local states and the operators are obtained by a direct replacement:

$$\begin{aligned} |1\rangle, |0\rangle &\rightarrow |\uparrow\rangle, |\downarrow\rangle, \\ b_i, b_i^\dagger &\rightarrow \sigma_{b,i}^-, \sigma_{b,i}^+, \end{aligned} \quad (6.6)$$

where the spin states associated with each lattice site denote presence ($|\uparrow\rangle$) or absence ($|\downarrow\rangle$) of a particle on that site. This direct replacement is possible since both spin and bosonic operators satisfy the same commutation rules (Eq.(6.2)). Hence, the transformed Hamiltonian from Eq.(6.3) is given by

$$\hat{H} = -J \sum_i^{M-1} \left(\hat{\sigma}_{b,i}^+ \hat{\sigma}_{b,i+1}^- + \text{h.c.} \right), \quad (6.7)$$

On the other hand, the same mapping for fermions is not trivial. In order to explain it, we have to consider, as we explained in section 2.4.1.1, that any fermionic state in second quantisation requires an order convention that we choose to be the natural lattice site ordering, where we describe a state with full occupation in the lattice in the following form

$$\hat{a}_1^\dagger \hat{a}_2^\dagger \dots \hat{a}_M^\dagger |vac\rangle. \quad (6.8)$$

This ordering choice is arbitrary but it is the simplest for bookkeeping when operators are applied on the state. From this ordering we infer that when applying any operator acting on site l to the state, this operator will need to anticommute with any other operator on sites 1 to $l-1$ in the state description. And so, expressing this in terms of spin operators (with bosonic commutation rules) requires the addition of a string operator to account for anti-commutation of the applied operator. The transformation is defined as

$$\hat{a}_l^{(\dagger)} = \exp\left(\mp i\pi \sum_{j<l} \hat{\sigma}_{a,j}^+ \hat{\sigma}_{a,j}\right) \hat{\sigma}_{a,l}^{-(+)}; \quad \hat{\sigma}_{a,l}^{-(+)} = \exp\left(\pm i\pi \sum_{j<l} \hat{a}_j^\dagger \hat{a}_j\right) \hat{a}_l^{(\dagger)}, \quad (6.9)$$

implying that

$$\begin{aligned} |1\rangle, |0\rangle &\rightarrow |\uparrow\rangle, |\downarrow\rangle, \\ \hat{a}_l^{(\dagger)} &\rightarrow (-1)^{\theta_l} \hat{\sigma}_{a,l}^{-(+)}, \end{aligned} \quad (6.10)$$

with the phase factor $\theta_l = \sum_{i<l} \hat{\sigma}_{a,j}^+ \hat{\sigma}_{a,j} = \sum_{i<l} \hat{n}_{a,i}$ accounting for any anticommutation of fermionic operators. One can immediately observe that both transformations in Eq.(6.6) and (6.10), are different. Nevertheless, in the transformed Hamiltonian all phases θ_l vanish for fermions and we obtain the same expression as (6.7):

$$\hat{H} = -J \sum_i^{M-1} \left(\hat{\sigma}_{a,i}^+ \hat{\sigma}_{a,i+1}^- + \text{h.c.} \right), \quad (6.11)$$

We can explicitly observe how the phases vanish considering the hopping terms in (6.10):

$$\hat{a}_l^\dagger \hat{a}_{l+1} \rightarrow (-1)^{(\sum_{i<l} \hat{n}_{a,i})} \hat{\sigma}_{a,l}^+ (-1)^{(\sum_{i<l} \hat{n}_{a,i})} \hat{\sigma}_{a,l+1}^- = \quad (6.12)$$

$$= \underbrace{(-1)^{(\sum_{i<l} 2\hat{n}_{a,i})}}_1 (-1)^{\hat{n}_{a,l}} \hat{\sigma}_{a,l}^+ \hat{\sigma}_{a,l+1}^- = \hat{\sigma}_{a,l}^+ \hat{\sigma}_{a,l+1}^-, \quad (6.13)$$

since we require initially $\hat{n}_{a,l} = 0$ for the element to be non-zero as fermionic commutation rules impose $(\hat{a}_l^\dagger)^2 \equiv 0$, that is to say, that only one particle can occupy a lattice site. And so, Hamiltonians including only first-neighbour tunneling are identical in 1D.

In general, any term that is quadratic in $\hat{a}_l, \hat{a}_l^\dagger$ or a combination of both will have no fermionic phase since it will be proportional to $(-1)^{(\sum_{i<l} 2\hat{n}_{a,i})} = 1$. For example, the local density is proportional to a product of two operators $\hat{n}_{a,i} = \hat{a}_i^\dagger \hat{a}_i$, thus any phase that arises from the commutation will cancel and $\hat{n}_{a,i} = \hat{\sigma}_i^+ \hat{\sigma}_i^-$. Similarly, for a nearest-neighbour offsite interaction $\propto \hat{n}_{a,l} \hat{n}_{a,l+1}$ where again all phases would cancel as the terms are proportional to the local densities (quadratic operators in $\hat{a}_l, \hat{a}_l^\dagger$).

As a result, in these local models, the densities and energy eigenvalues will be identical, and local correlations – both for the eigenstates and out-of-equilibrium

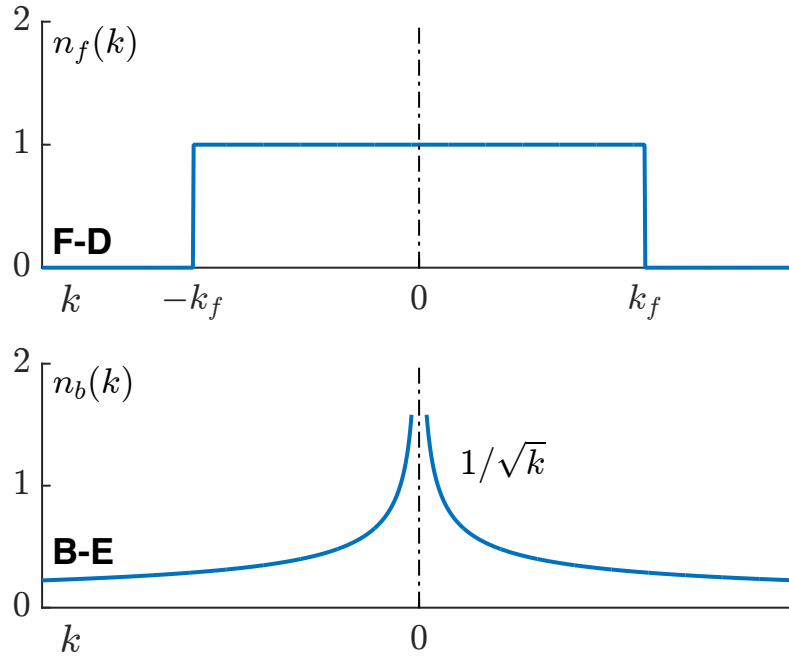


Figure 6.1: Momentum distribution schematic of the one-dimensional ground state of spinless fermions (top), governed by Fermi-Dirac statistics and hardcore bosons (bottom) given by Bose-Einstein distribution in the thermodynamic limit.

dynamics induced by changing local trap quantities – will be equal as well. Note that differences exist – already in 1D – in the momentum distribution of both fermions and HCBs, governed by Fermi-Dirac and Bose-Einstein statistics respectively [145]. As a result, the momentum distribution of the ground state will be different [146]: a flat distribution with a sharp drop in the Fermi energy for fermions and a peak around zero momentum for bosons as depicted in Fig.6.1.

The momentum distribution can be accessed with time-of-flight type measurements. However, we expect that even a few loss events will lead to distinguishable behaviour between fermions and HCBs when simply measuring local quantities. And so, our approach is to introduce these dissipative terms that could disturb the dynamics producing relevant differences in the behaviour and that would not appear in the closed system.

The dissipative channel we consider in subsequent sections is single-particle loss

which is proportional to

$$\hat{a}_l = (-1)^{(\sum_{i<l} \hat{n}_{a,i})} \hat{\sigma}^-, \quad (6.14)$$

where the string operator does not vanish. From the form of Eq.(6.14), we can infer that a loss event generates differences in local quantities due to the different exchange symmetries in the many-body wavefunction. Moreover, we will be able to observe differences in quantities that were identical in the closed system dynamics such as density distributions, which are accessible with current experimental techniques in quantum gas microscopes [29, 30, 31, 32, 33, 34]. And so, as we show in the following sections, particle loss will allow us to probe closed system properties as it is the case of bosonic or fermionic particle statistics.

6.2.1 Tensor network representation of loss operators

Before presenting the results, it is important to highlight that the numerical results that we will present in the coming sections aim to describe relevant system sizes for the current experiments [29, 30, 31, 32, 33, 34] that are of the order of tens of sites. In general, exact-diagonalization methods do not allow us to reach these sizes and so it is essential to make use of tensor-network techniques [35, 42, 147], that we introduced in chapter 4. Usually, when dealing with dissipative dynamics there are two major approaches. On the one hand, it is possible to map the density operator describing the state of the open system ρ to a matrix product operator [98, 97]. Another possibility is to make use of quantum trajectories [46, 47, 92](see subsection 3.3.2), which transforms the dynamics of the density operator into an stochastic sampling of pure-state evolutions that are described through matrix product states. In the results that we will present in this chapter we make use of the latter method. In this formalism, we apply the time-evolving block decimation (TEBD) [39] (see subsection 4.3) in order to compute the time evolution of one-dimensional many-body systems.

One of the bottlenecks that the simulation through tensor networks faces when describing our particular system is that fermionic losses as we discussed in section 6.2 are non-local. Due to the presence of a string operator proportional to $N_{<i} = (-1)^{\sum_{k<i} \hat{n}_{a,k}}$, this non-local quantity cannot be easily expressed in terms of a local tensor similar to the ones we apply in TEBD to compute time evolution.

Consequently, it would require an expression in terms of a MPO, which would in general be exponentially coupled. Alternatively, this operator can be expressed as a local operator if we split our state representation into parity conserving sectors (see section 4.1.6). In addition, expressing our state in terms of symmetry conserving algorithms [105, 40] helps to optimize our time evolution calculations of pure states through TEBD.

More specifically, in our tensor network every local tensor A^{d_i} – with the notation of section 4.1 – gathers together any state with particular population to the left or the right of a given site i . Since this quantum number is encoded in our tensor description, the value of the string operator $N_{<i} = \pm 1$ becomes trivial as we know the specific value. As a result, we simply need to apply the annihilation operator \hat{a}_i , that is represented as a local operator in terms of our MPS structure, multiplied by a phase that is known for each part of the tensor. In this way, the losses in the system can be modeled in an affordable way.

Note that all other terms appearing in the dynamics [Eq.(6.3), Eq.(6.4) and Eq.(6.16)], both in the unitary and the dissipative part, are either proportional to $\hat{n}_{a,i} = \hat{a}_i^\dagger \hat{a}_i$, or proportional to $\hat{a}_i^\dagger \hat{a}_{i\pm 1}$, with all string operators evaluating to one as discussed in Sec.6.2. Thus, the only non-local phase arises from the loss term that we have already discussed. As a result, we can apply standard TEBD algorithms to compute the time evolution and study the dissipative dynamics through quantum trajectories efficiently as all our terms become local.

Below we will first use these techniques to compute the dynamics resulting from loss on demand at a particular site and a particular time. We then follow this by simulating a master equation that describes loss processes that occur at random during the dynamics.

6.3 Differences in the presence of deterministic losses

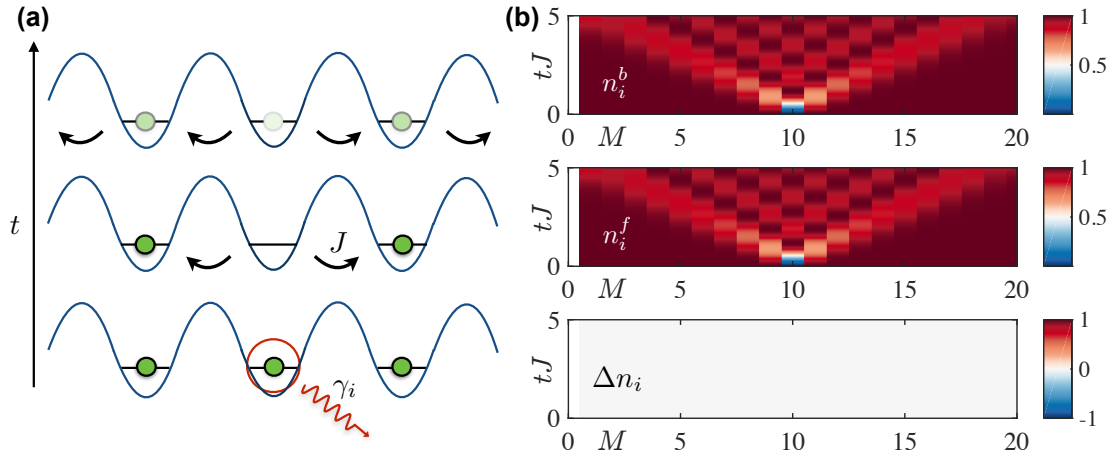


Figure 6.2: (a) Diagram of a loss event in an optical lattice on site i with probability γ_i . The density hole created will propagate through normal tunneling processes and will delocalize over time; (b) Evolution of the particle density for bosons \hat{n}_i^b , fermions \hat{n}_i^f and the normalized difference of these, Δn_i , as a function of time. In this case, loss occurs on site $i = 10$ on a lattice with $M = 20$ from an initial product state with a single particle on each site, so a single sign is applied to the fermionic wavefunction for all basis states and both profiles remain identical, i.e. $\Delta n_i = 0$. Diagram taken from [125].

In this section, we study the dynamics of the system when we induce the loss of a particle and the differences that this event produce between fermions and HCBs. Fig.6.2 shows a schematic view of the type of processes we will study. We investigate the density profiles after a deterministic loss event. In the case of the diagram we choose the loss to occur in the middle site at $t = 0$, beginning from an initial product state with one atom on every lattice site. Because of the simple initial state and the single loss process, the density distributions for bosons and fermions as a function of time are identical, i.e., the normalized difference,

$$\Delta n_i = \frac{n_i^b - n_i^f}{n_i^b + n_i^f}, \quad (6.15)$$

where $n_i^b = \langle \hat{n}_{b,i} \rangle$ and $n_i^f = \langle \hat{n}_{a,i} \rangle$, is zero in this case. Note that for the case of vanishing densities $n_i^b + n_i^f = 0$, which happen only in certain initial states, we set

the normalized difference to $\Delta n_i = 0$. The vanishing of Δn_i is due to the fact that $(-1)^{(\sum_{i<l} \hat{n}_{a,i})} = \pm 1$ when we consider a well-defined number of particles to the left as it is the case of a product state with unit-filling. As a result a global phase is applied to the fermionic wavefunction with no effect on the density distributions. However, a second loss event in the system would not be identical anymore since the delocalization of the first hole, propagating in a light-cone, would produce parts of the wavefunction to get different phase factors. This will be the idea we will exploit in the following results.

In the following, we will study and identify differences between HCB and spinless fermions, focusing particularly on Δn_i when we induce losses on demand. This could be achieved in a quantum gas microscope in different ways. Here we include two methods that have been experimentally realized:

1. Single-site addressing [127]: the loss will be produced by a sequential change of the lattice depth that will first increase, freezing the dynamics of the system. After this, a single site will be addressed with an auxiliary laser field modifying the internal state of the atom which is then removed from the lattice with a beam resonant to the new internal state. Finally, the lattice depth will be decreased and the dynamics will continue.
2. Electron beam [126]: the loss is now produced by collisional ionization of the neutral atoms by an electron beam focused on a lattice site. The ions generated in the given site are guided out of the system using an electric field.

Now, that we have provided means to induce losses deterministically, we compute the time evolution of spinless fermions and hard-core bosons governed by the Hamiltonians in Eq.(6.3) and Eq.(6.4). We first consider the atoms to be in a product state and induce a loss at $t = 0$ on site $M_0 = M/2$. This first loss event, as we discussed before (see Fig.6.2), will produce no difference between particle statistics as the fermionic state will get a single global phase from the application of the annihilation operator since $N_{<M/2} = \pm 1$. Then, after a certain evolution time $t = \tau_0$ a second loss is induced on site $M_0 - \delta_M$, with δ_M a chosen lattice distance.

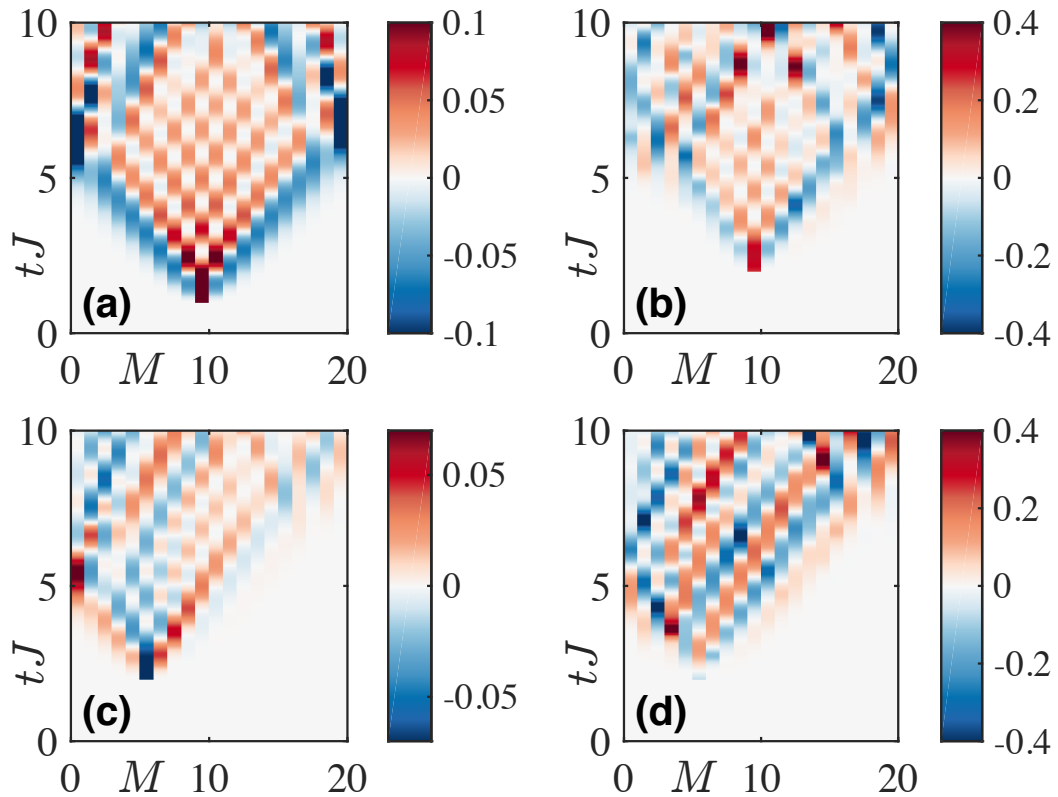


Figure 6.3: (a) Evolution of the difference in density distribution Δn_i after inducing a loss at $t = 0$ on site $M_0 = M/2$ and a second loss is induced on site $M_0 - \delta_M$ for a system with $M = 20$, $n_0 = 1$, $D = 100$, $dt = 0.001$, $J = 1$, $\tau_0 = 1$, $\delta_M = 0$; (b) Same as (a) with $\tau_0 = 2$ and $n_0 = 0.5$; (c) Same as (a) with $\tau_0 = 2$ and $\delta_M = 4$; (d) Same as (a) with $\tau_0 = 2$, $n_0 = 0.5$ and $\delta_M = 4$. These calculations are performed beginning from a product state with the corresponding densities indicated above: a single particle on each lattice site ($n_0 = 1$) or every odd site ($n_0 = 0.5$).

In Fig.6.3, we present the difference in density distribution Δn_i after computing time evolutions of the kind we just described for different initial times and different filling factors. In particular, we will start both with a configuration consisting of a single atom per site with $n_0 = 1$ (an eigenstate of \hat{H} , and so, stationary) and a charge-density wave state (CDW), with only odd sites occupied initially, i.e. $n_0 = 0.5$. The CDW will exhibit evolution in the density distributions regardless of the presence of losses while the unit-filling will allow us to investigate the interplay of the two losses in the simpler scenario. For the first configuration, differences only appear in the dynamics after the second loss, as described above, since only after the

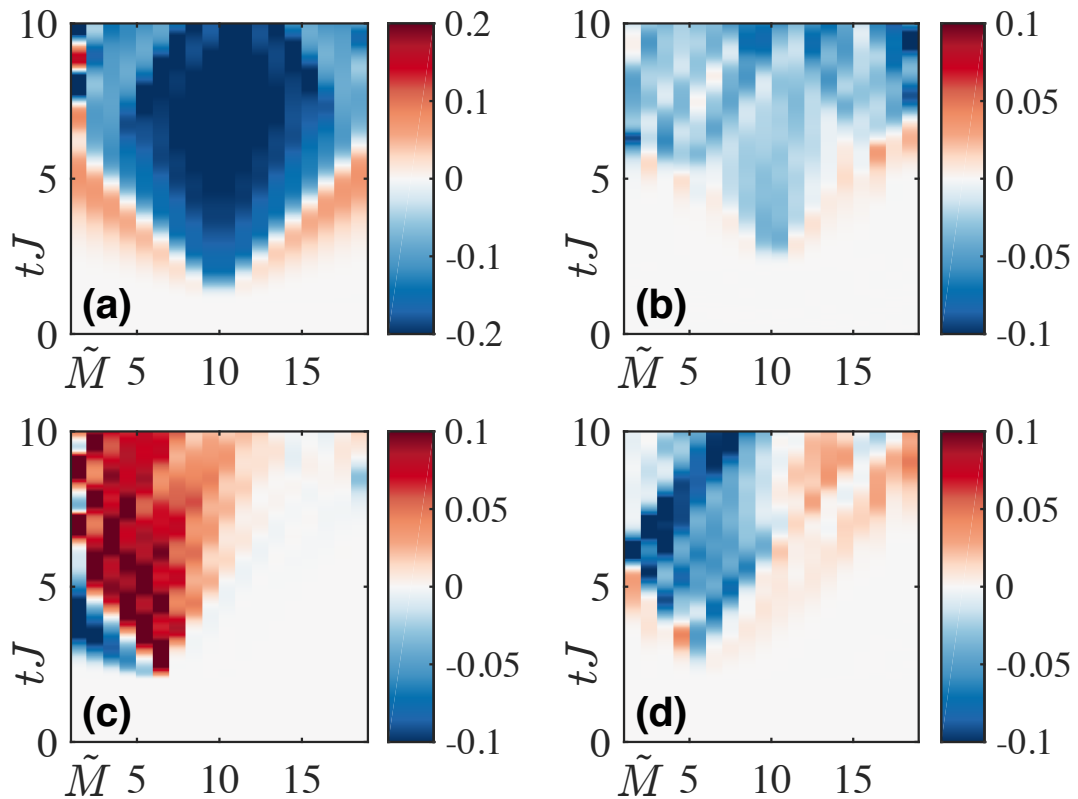


Figure 6.4: (a) Evolution of the weighted difference in the entanglement entropy ΔS at every lattice bipartition $\tilde{M} \in [1, M - 1]$ for a system with $M = 20$, $n_0 = 1$, $D = 100$, $dt = 0.001$, $J = 1$, $\tau_0 = 1$, $\delta_M = 0$; (b) Same as (a) with $\tau_0 = 2$ and $n_0 = 0.5$; (c) Same as (a) with $\tau_0 = 2$ and $\delta_M = 4$; (d) Same as (a) with $\tau_0 = 2$, $n_0 = 0.5$ and $\delta_M = 4$. These calculations are performed beginning from a product state with the corresponding densities indicated above: a single particle on each lattice site ($n_0 = 1$) or every odd site ($n_0 = 0.5$).

delocalization of the initial hole we obtain a superposition of different numbers of particles to the left of any given site, and so the effect of the phase is non-trivial for fermions. Consequently, spinless fermions and HCBs exhibit density distributions that start to differ ballistically in a well-defined light cone. This is reminiscent of the spreading of correlation functions we expect in this system [148]. In the unit-filling regime (Fig.6.3a and Fig.6.3c), we observe that only losses near the location of the first loss ($\delta_M \sim 0$), i.e. where the population is not still deeply in the unit-filling Mott phase, lead to a significant difference between bosons and fermions, as it is only in this case that the effects of the string operator are non-trivial. In this way, the

light-cone defined by the spreading of the first loss marks the area where a second loss event would produce a clear distinction between particle statistics. In the case of half-filling (Fig.6.3b and Fig.6.3d), as the particles are allowed to quickly delocalize, we observe greater differences and the relevance of the position where the second loss occurs disappears rapidly due to the richer dynamics.

Similarly, we can study the effect that the losses produce in other quantities such as the Von Neumann Entropy of entanglement between two partitions of the system (see section 4.1.4). In Fig.6.4, we present the weighted difference in the entanglement entropy $\Delta S = \frac{S_{vN}^b - S_{vN}^f}{S_{vN}^b + S_{vN}^f}$, where $S_{vN}^{b/f} = -\text{tr}(\rho^{b/f} \ln \rho^{b/f})$ at every bipartition of both the bosonic and fermionic systems. The entropy² is an interesting indicator theoretically as it provides information about the evolution of the system entanglement. We can observe that the non-local phase associated with the fermionic loss permits a faster spreading of the entanglement along the system while we observe bosonic entanglement being higher (red areas) around the location of the loss. The higher mobility in the case of half-filling (Fig.6.4b and Fig.6.4d) causes the S_{vN} to be larger for both particle statistics, consequently the weighted differences we observe are smaller for the case of CDW. As before, losses that occur near the boundary of the lattice (Fig.6.4c,d) lead to a smaller observable difference as the fermionic state is closer to a product state.

Note that now lattice configurations away from unit filling (compare Fig.6.4a and Fig.6.4b) exhibit smaller differences between fermions and bosons. This is due to the fact that the higher mobility in the lattice contributes to overall higher values of S_{vN} for both species and we are representing normalized differences.

²Other measures of entanglement entropy, such as Renyi Entropies, can be directly measured in quantum gas microscope experiments for both fermions and HCBs [149, 150, 151]

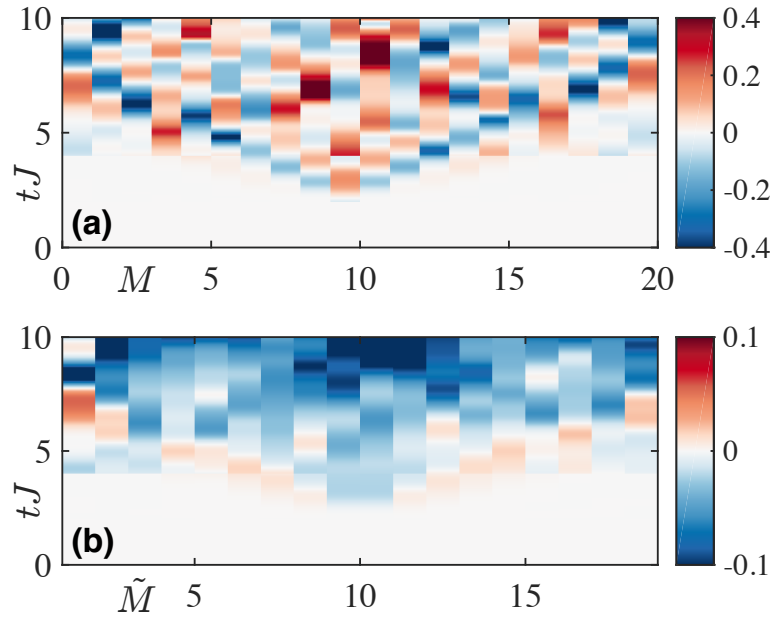


Figure 6.5: (a) Evolution of the difference in density distribution Δn_i for a system with $M = 20$, $n_0 = 0.5$, $D = 128$, $dt = 0.001$, $J = 1$, $\delta_M = 0$ with no loss at $t = 0$, a first loss is induced at $t = \tau_0 = 2$ and a second loss occurs at $t = \tau_1 = 2\tau_0$; (b) Same as (a) for the ΔS . In contrast with the case of the first loss induced in the product state, differences between bosons and fermions are observed from the first loss event.

For completeness, in Fig.6.5 we analyze the impact of dynamics prior to the first loss event, presenting weighted difference of both density distribution Δn_i and ΔS entropies in the case of losses with $t > 0$. The profiles differ from the time of the initial loss due to the initial coherent dynamics prior to the loss (the state no longer has a well-defined particle number to the left). However, we do not observe significant qualitative differences in the behaviour, and we consider the behaviour included in Fig.6.3 and 6.4 is quite general.

With the results provided we conclude that by inducing losses on demand we can probe properties of the closed system such as the intrinsic particle statistics in a robust way. Moreover, we have identified relevant observables that are experimentally accessible and theoretically relevant, and which exhibit clear behaviours which we can identify and describe.

6.4 Differences in the presence of stochastic losses

While experimental techniques allow for particle losses to be engineered on demand, natural stochastic particle losses are an inherent form of dissipation in current optical lattice experiments that can impact the behaviour of the system. These losses are produced, e.g. by collisions with background gas and photon scattering bursts [135]. Moreover, on similar timescales to the ones of loss rate we expect to observe inelastic light-scattering with the laser field leading to dephasing [130, 152, 131, 135]. Despite the fact that these events occur at random, we have a good theoretical description based on the Born-Markov Approximation (section 3.3). As a result, the dynamics of the system in the presence of particle losses can be described via a master equation for the evolution of the system density operator ρ_{tot} .

On the microscopic level, we can justify the use of the Born-Markov approximation based on the fact that we have a large separation of energy scales with dominant frequency scales associated with the energy of the single-particle loss event and by the photon frequency for dephasing due to light scattering (see section 3.3). The resulting equation is given by:

$$\begin{aligned} \frac{d\rho}{dt} = & -i [\hat{H}, \rho] - \frac{1}{2} \sum_{m,\alpha}^M \gamma_{\alpha,m} (\hat{J}_{\alpha,m}^\dagger \hat{J}_{\alpha,m} \rho \\ & + \rho \hat{J}_{\alpha,m}^\dagger \hat{J}_{\alpha,m} - 2\hat{J}_{\alpha,m} \rho \hat{J}_{\alpha,m}^\dagger), \end{aligned} \quad (6.16)$$

where $\alpha \in \{l, d\}$ is an index summing over the separate terms for dephasing and loss, $\hat{J}_{l,m} = \hat{a}_m(\hat{b}_m)$ represents the loss of a fermion (boson) on site m , $\hat{J}_{d,m} = \hat{n}_{a,m}(\hat{n}_{b,m})$ describes the dephasing process and $\gamma_{l/d,m}$ is the decay amplitude for the m -th dissipation channel that will be different for dephasing and loss processes.

With the inclusion of both stochastic losses and dephasing we investigate if the differences that we observed in the deterministic case persist in a more general

scenario or if we can find other relevant local observables that will exhibit dynamics that are dependent on particle statistics. Furthermore, we will consider the fact that in experiments the onsite interaction (so far we assumed $U \rightarrow \infty$) will be very large but finite. This is important since for finite interaction strengths between bosons, a perturbation theory expansion dictates the appearance, in second order, of an offsite nearest-neighbour interactions of the form $\sum_{\langle ij \rangle} V \hat{n}_i \hat{n}_j$ with $V \propto J^2/U$ and U the onsite interaction that we will consider as finite when including this term. We note that this can also arise, e.g., due to direct dipole-dipole interactions between atoms on neighbouring lattice sites [153], which allow for larger V values, including up to $V \approx J$, which we will use in some of the calculations below.

6.4.1 Closed system dynamics

We investigate in this section a variety of local and lattice-averaged quantities. It is important to first study these in the closed system to obtain a good measure for comparing the open system profiles. These quantities should be identical for both particle statistics in the absence of losses as we discuss in section 6.2. The quantities we will study in this section are: (i) the local densities \hat{n}_i ; (ii) the density fluctuations $\sigma_{n_i} = \langle \hat{n}_i^2 \rangle - \langle \hat{n}_i \rangle^2$; (iii) the odd-even density imbalance, a common quantity in the study of MBL systems (see chapter 7), given by the expression

$$\mathcal{I} = \frac{n^o - n^e}{n^o + n^e}, \quad (6.17)$$

where $n^{o/e} = \sum_{i \in \text{odd/even}}^M \langle \hat{n}_i \rangle$.

In Fig.6.6 we present the dynamical profiles of both the density in the central lattice site and the imbalance. Both quantities are identical, within numerical precision, for both fermionic and bosonic evolution (see Inset in Fig.6.6 a). In Fig.6.6 a, we observe that the density oscillates around the average density $n_{steady} = n_T/M$ with fluctuations of decreasing amplitude. However, these oscillations remain relevant for all the simulation time. As a highly-oscillating quantity it will be interesting to study if the presence of losses increases or decreases this amplitude and in which way it

affects differently bosons and fermions. We will analyze these fluctuations in detail later in subsection 6.4.3.

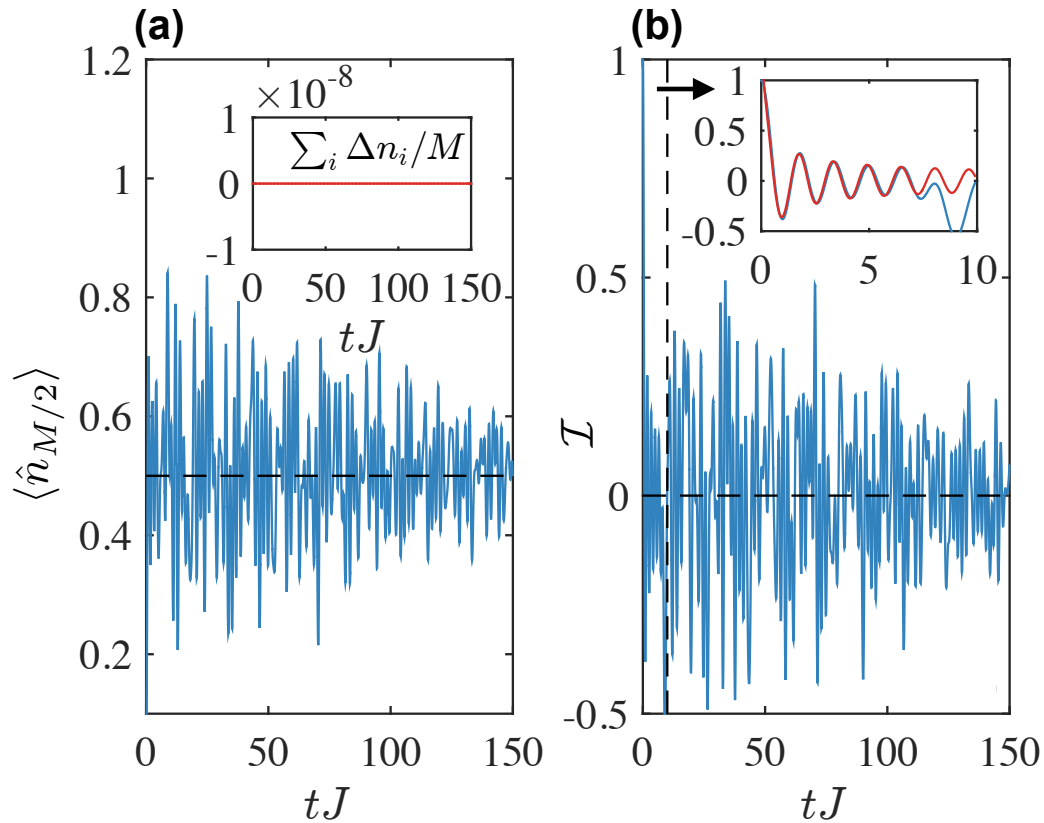


Figure 6.6: (a) Closed system evolution of the middle site density $\langle \hat{n}_{M/2} \rangle$ for a system with $M = 16$, $n_0 = 0.5$, $J = 1$, $\gamma_l = 0$, $\gamma_d = 0$; numerical parameters are $dt = 0.001$ and $D = 150$. In the absence of loss both fermionic and bosonic results are identical, fluctuating around n_0 . Inset: averaged density difference between fermions and bosons, as predicted this quantity is zero; (b) Same as (a) for the imbalance \mathcal{I} . Again, fermions and bosons show the same profile, fluctuating around zero as expected for a non-disordered system. Inset: short-time imbalance (blue) compared with the analytical result (red) that can be derived for free fermions. Note that the disagreement occurs at time $\sim M/2J$ that corresponds to the time required by an excitation to travel through the whole lattice, which is a finite-size effect.

Regarding the imbalance (Fig.6.6 b) we obtain a similar profile with long-lived fluctuations around the expected value of $\mathcal{I} = 0$ since the system is not disordered. Note, that for the case of the imbalance we can obtain analytical results for free fermions (see [154]) that should agree with our profile before the first revival occurs.

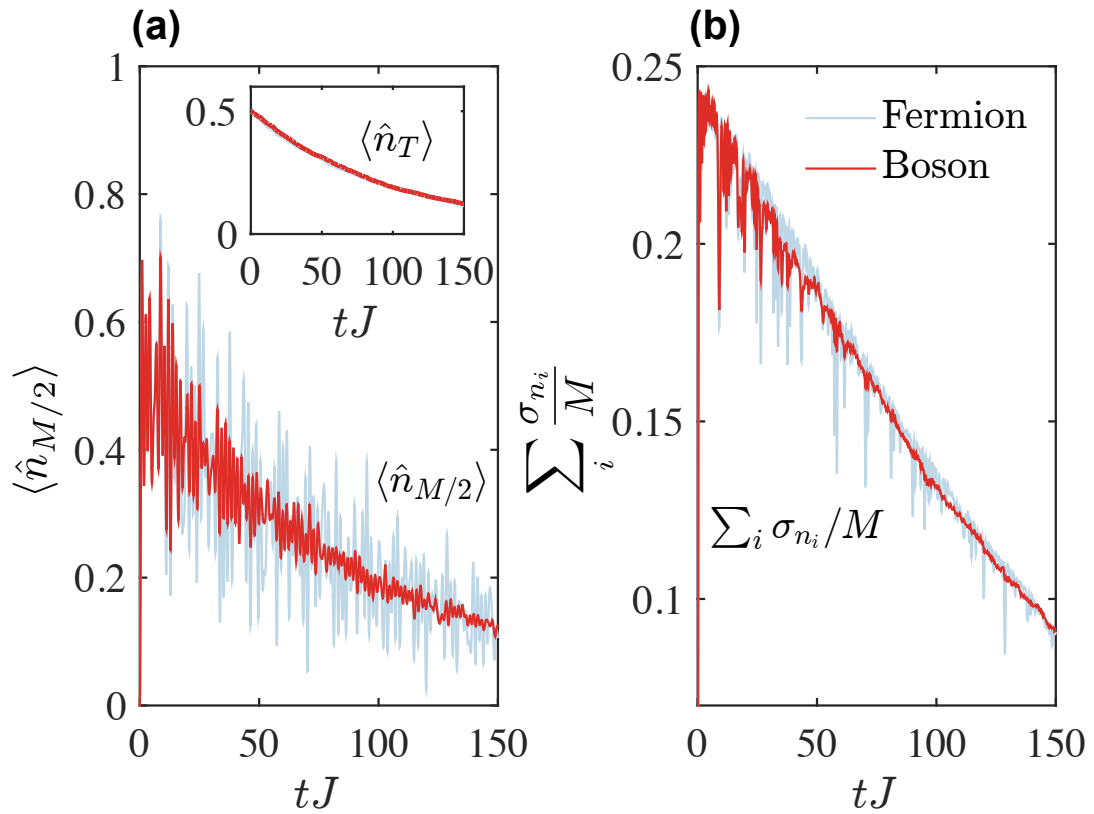


Figure 6.7: (a) Comparison of bosonic and fermionic evolution of the middle site density $\langle \hat{n}_{M/2} \rangle$ for a system with $M = 16$, $n_0 = 0.5$, $J = 1$, $\gamma_l = 0.01$, $\gamma_d = 0$; numerical parameters are $dt = 0.001$ and $D = 200$. The inset shows the total particle number $\langle \hat{n}_T \rangle$ to provide some guidance over the evolution of the total occupation in the lattice as losses occur. (b) Same as (a) for the normalized total density fluctuations $\sum_i \sigma_{n_i} / M$. These calculations are performed beginning from a charge density wave at half-filling, with a particle on each even-numbered site.

Since the typical time for an excitation to cover the whole lattice twice is given by $t \sim M/2J$, the profile can be compared for short times to the analytical solution given by $\mathcal{I} \propto J_0(4Jt)$ where J_0 denotes the zeroth-order Bessel function. We include the comparison in the inset of Fig.6.6 b, observing a good agreement before the finite-lattice effects become relevant.

We will revisit all these quantities later on, analyzing how they vary in the presence of dissipation and in which way different particle statistics plays a role in the different profiles.

6.4.2 Stochastic losses and the distinction of fermions and HCBs

In this subsection, we compute the dissipative dynamics in the presence of both losses (with amplitude γ_l) and dephasing (with amplitude γ_d), again for the initial charge-density wave, with one particle in every second lattice site. We focus our interest again on quantities related to local densities that can be measured in quantum gas microscopes as shown in Subsection 6.4.1, with the aim of comparing with those results.

In Fig.6.7, we consider the evolution of local densities, spatially-averaged density fluctuations and total particle numbers for both fermions and bosons. In Fig.6.7a we present the local density on the middle of the lattice $\langle \hat{n}_{M/2} \rangle$, these results can be compared to the ones obtained in Fig.6.6a. We observe that the fluctuations in both species persist over the simulation time. However, bosonic fluctuations get considerably more damped over time than in the case of fermions where they retain a similar amplitude over the studied times (longer study in subsection 6.4.3). In both cases, the average value decrease over time as particles are removed from the lattice. We include the total particle number $\langle \hat{n}_T \rangle$ as an inset in Fig.6.7a to indicate the typical densities at longer times. The total particle number is identical for bosons and fermions since both are subject to the same dissipation amplitude γ_l . We can conclude that after a transient time, fermions exhibit larger fluctuations, which we could in principle detect despite the fact that the total particle number and the average density coincides with that for bosonic particles.

In Fig.6.7b, we present the lattice-averaged fluctuations $\sum_i \sigma_{n_i} = \sum_i (\langle \hat{n}_i^2 \rangle - \langle \hat{n}_i \rangle^2)$. Despite the fact that again fermions exhibit higher fluctuations than bosons, the difference is smaller. The differences involve decreased fluctuations associated with revivals of the CDW correlations after these are reflected by the boundaries. We observe that these persist longer in time for the fermions. Hence, the distinction here relies on boundary effects, which are dependent on system size. Also, these drops are quite sharp in time and so they might be difficult to measure them reliably in an experiment. We can conclude that local densities exhibit clear differences in

the fermionic and bosonic profiles while lattice-averaged quantities like the lattice-averaged fluctuations seem to remain closer to each other.

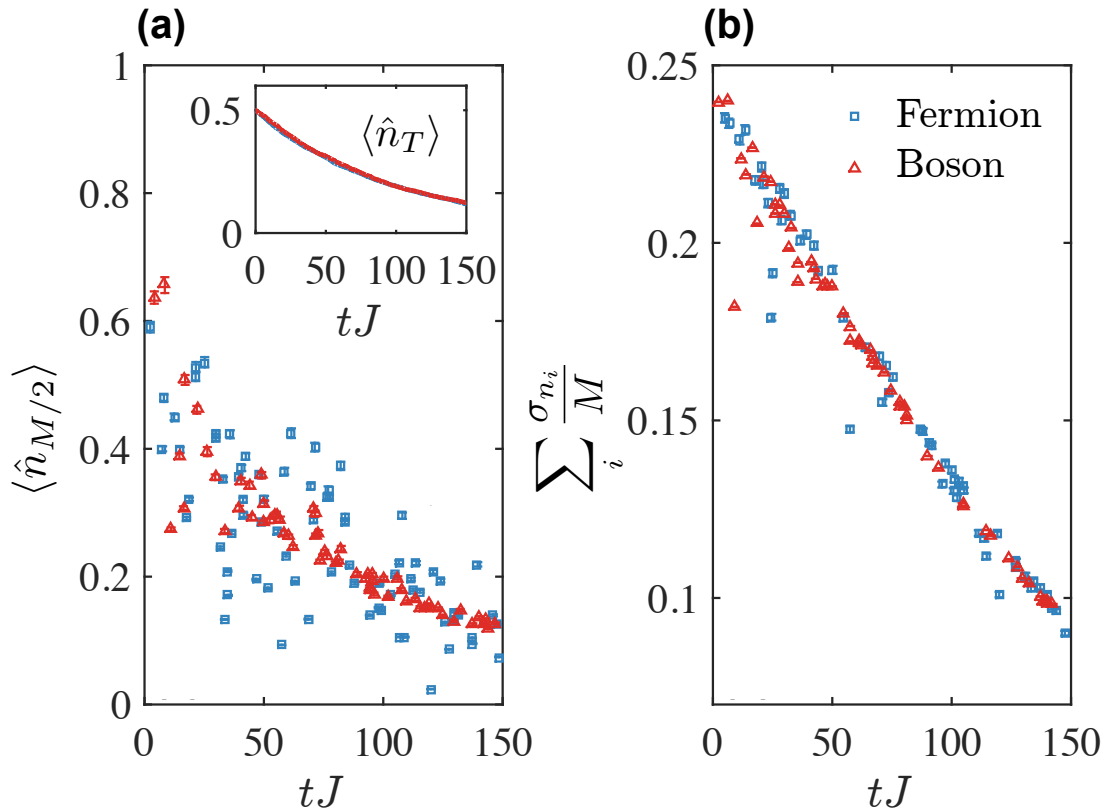


Figure 6.8: (a) Comparison of bosonic and fermionic evolution of the middle site density $\langle \hat{n}_{M/2} \rangle$ for a system with $M = 16$, $n_0 = 0.5$, $J = 1$, $\gamma_l = 0.01$, $\gamma_d = 0$; numerical parameters are $dt = 0.001$ and $D = 200$. The inset shows the total particle number $\langle \hat{n}_T \rangle$ to provide some guidance over the evolution of the total occupation in the lattice as losses occur. (b) Same as (a) for the normalized total density fluctuations $\sum_i \sigma_{n_i} / M$. These calculations are performed beginning from a charge density wave at half-filling, with a particle on each even-numbered site. Note that these functions are rapidly oscillating, and that each point represents a snapshot of the values on a randomly spaced grid in time. The data includes statistical error bars, which are contained within the point markers in most of the cases.

As a complementary step, we include the results of Fig.6.7 after filtering them with a random time grid in Fig.6.8 (both of the figures are generated with the same dataset). The idea is to imitate the conditions of an experiment where we cannot resolve the full dynamics and also individual measurements take some time that might vary in every

instance. Since all the presented quantities are highly-fluctuating curves in time, we intend to test which of the features observed before are robust in this scenario. Some features cannot be captured in this random grid like the fact that both bosons and fermions overlap at short times since no loss has occurred on average.

Nonetheless, we can still resolve the differences between bosons and fermions, specially in the case of the local density (Fig.6.8a) where the higher amplitude of the fermionic fluctuations manifests clearly even in the random grid. For the case of the total fluctuations, Fig.6.8b, we still observe some of the drops in the curve due to correlation revivals. However, these are now captured less often and so differences between fermions and bosons at long times ($t \sim 100 - 150$) are smaller. However, we consider that overall the ability to distinguish particle statistics is robust in this worst-case-scenario conditions.

We would now like to study if the addition of dephasing to the system, which typically occurs in experiments at similar timescales to losses, plays a role in the distinction between different particle statistics in the dynamics. We will study again the case of local densities in the central lattice site and we will now include the odd-even imbalance as our global quantity to compare with. This choice is based on the fact that we expect it to exhibit higher differences than the ones we obtained for the total fluctuations. The imbalance should be more sensitive to any density-density correlation between neighbour sites. Since our initial state has an antiferromagnetic-like density distribution, fluctuations over time in the imbalance might be larger for fermions as the loss operator, see Eq.(6.14), carries non-local information of the particle occupation.

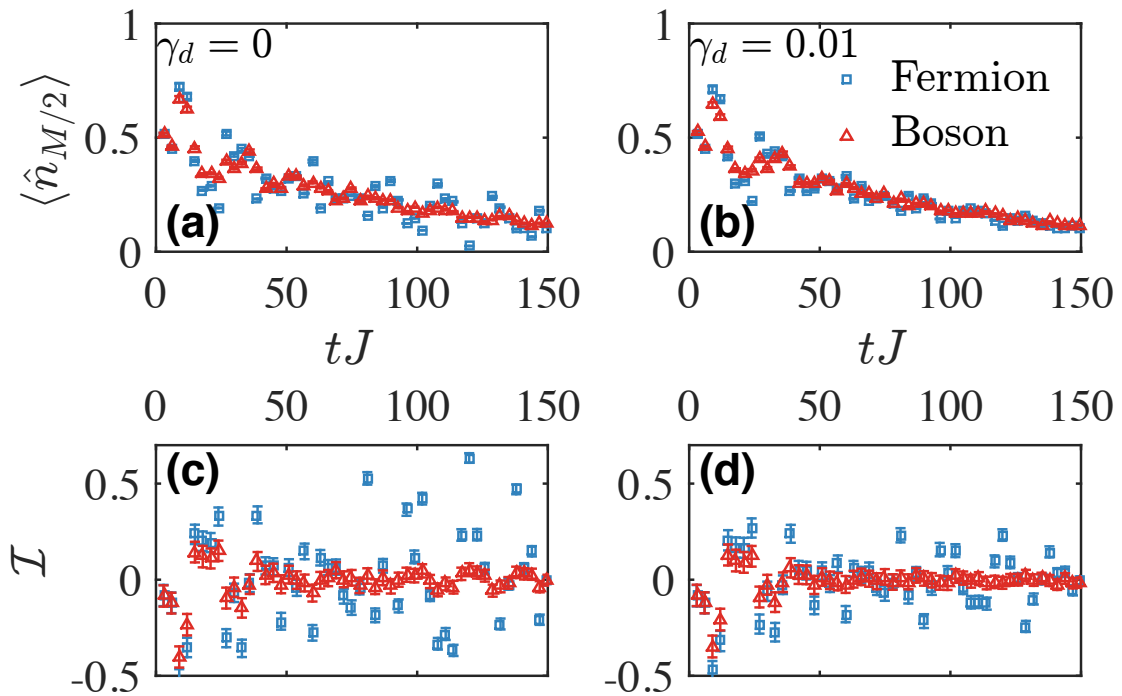


Figure 6.9: (a) Comparison of bosonic and fermionic evolution of the middle site density $\langle \hat{n}_{M/2} \rangle$ for a system with $M = 16$, $n_0 = 0.5$, $J = 1$, $dt = 0.001$, $\gamma_l = 0.01$, $\gamma_d = 0$; (b) same as (a) with $\gamma_d = 0.01$; (c) Comparison of bosonic and fermionic evolution of the odd-even imbalance \mathcal{I} with same parameters as (a); (d) same as (c) with $\gamma_d = 0.01$. These calculations are performed beginning from a charge density wave at half-filling, with a particle on each odd-numbered site. Note that these functions are rapidly oscillating, and that each point represents a snapshot of the values on a regularly spaced grid in time.

In Fig.6.9, we show both the local density on the central lattice site and the system odd-even imbalance, analyzing the robustness of both in the presence of dephasing. In Fig.6.9a and c, we compare the single site density and the imbalance without dephasing. We can observe that even though in both cases fermions and bosons oscillate around the same average value the fermionic fluctuations are much higher specially in the case of the imbalance. The addition of dephasing (Fig.6.9b and d) has a detrimental effect on the distinction, reducing the ability to observe differences between fermionic and bosonic dynamics. However, the imbalance maintains a robust difference between the fermionic and bosonic profiles showing that even in the presence of dephasing, the imbalance can be considered as a valid indicator of the particle statistics.

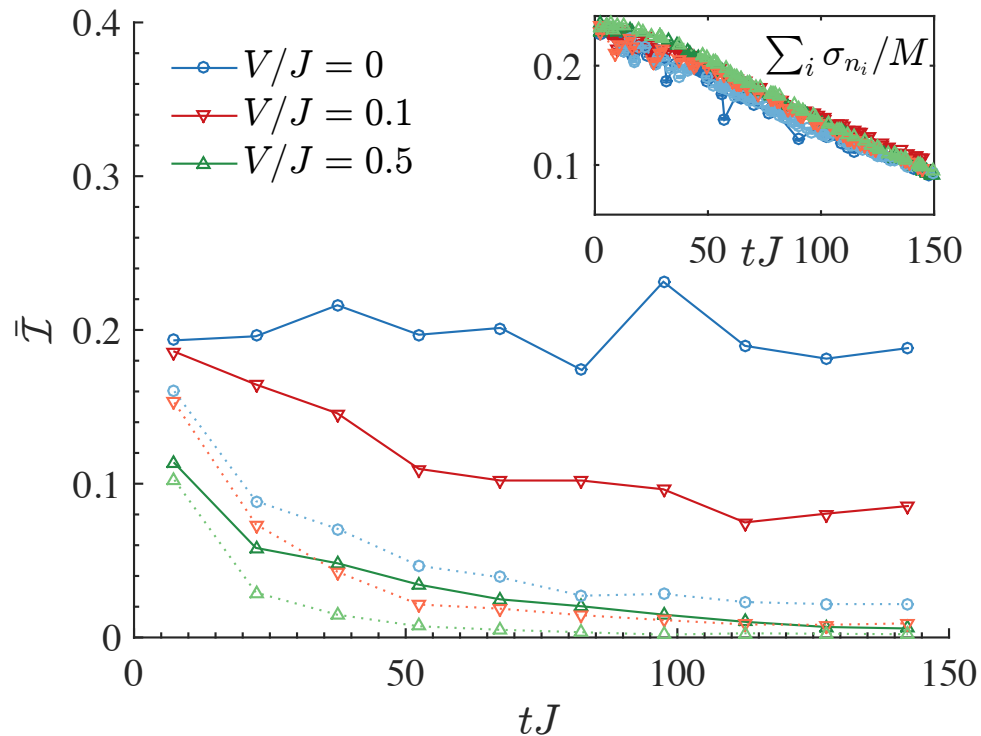


Figure 6.10: Comparison of bosonic (dashed line) and fermionic (solid line) evolution of the time-block averaged imbalance $\bar{\mathcal{I}} = \sum_i^{i+N_{\delta t}} |\mathcal{I}(t_i)| / N_{\delta t}$ for a system with $M = 16$, $n_0 = 0.5$, $J = 1$, $dt = 0.001$, $N_{\delta t} = 300$, $\gamma_l = 0.01$, $\gamma_d = 0$ and variable off-site interaction strength V . The imbalance average drops over time in the presence of interaction but remain distinguishable for both species. Inset: total density fluctuation for the same parameters, included for the purpose of comparison. Here, all lines overlap while we observe relevant differences in the imbalance. These calculations are performed beginning from a charge density wave at half-filling, with a particle on each odd-numbered site.

Finally, we also mentioned in the previous sections the possibility of including an onsite-interaction term of the form $\sum_{\langle ij \rangle} V \hat{n}_i \hat{n}_j$ either due to finite but large interaction strengths in bosons or by a dipole-dipole type of coupling that is added externally. As the imbalance has shown so far the best response in the sense of our ability to distinguish particle statistic in the stochastic-loss regime, we would like to investigate its robustness in the presence of this type of terms. Since the imbalance is a highly-oscillating function specially for the fermionic case in Fig.6.10, we present a time-block averaged imbalance $\bar{\mathcal{I}} = \sum_i^{i+N_{\delta t}} |\mathcal{I}(t_i)| / N_{\delta t}$, where $N_{\delta t}$ is the number of time points over which we average. Averaging the absolute value allows

us to study smoother profiles, which we can more easily compare. We observe in the results that the differences between fermions and bosons are reduced as we increase the onsite-interaction strength but they remain distinguishable for the simulated time even for the case of $V/J = 0.5$. This can be compared to the case of the lattice-averaged density fluctuations, another lattice-averaged quantity, included in the inset for the sake of comparison where we observe that all the curves almost overlap for any choice of parameters.

From this analysis we can establish that the imbalance – a global quantity related to local densities – is robust to moderate interactions and to moderate dephasing at rates comparable to the losses, and provides an interesting quantity with which to investigate differences between HCBs and spinless fermions also in the case of randomized losses in space and time.

6.4.3 Analysis of the density fluctuation damping

In Fig.6.6a and Fig.6.7a we presented the local densities of fermions and HCBs both in the presence and the absence of loss, with all the curves fluctuating around an average value $n_{steady} = n_T(t)/M$. However, it was difficult to compare the amplitudes of these fluctuations as in the case of $\gamma_l \neq 0$ the overall density was decreasing over time ($n_T(t \rightarrow \infty) = 0$). In Fig.6.11 we compare the normalized density fluctuation from the predicted average density $|\langle \hat{n}_{M/2} \rangle - \langle \hat{n}_T/M \rangle| / \langle \hat{n}_T \rangle$ for closed, fermionic and bosonic system.

By normalizing the fluctuations to the total particle number we can observe that the relative fluctuations decrease over time in the closed system and in the bosonic case, with the latter damping being stronger. On the other hand, fermionic losses seem to maintain the relative density fluctuations approximately constant for the simulated time. Highlighting once again the difference in behaviour between bosonic and fermionic atoms. As these curves overlap quite strongly for the three cases in Fig.6.11 we also provide time-block averages (solid lines) to help visualize how the fermionic fluctuations persist over time in comparison with bosons and the case of no losses.

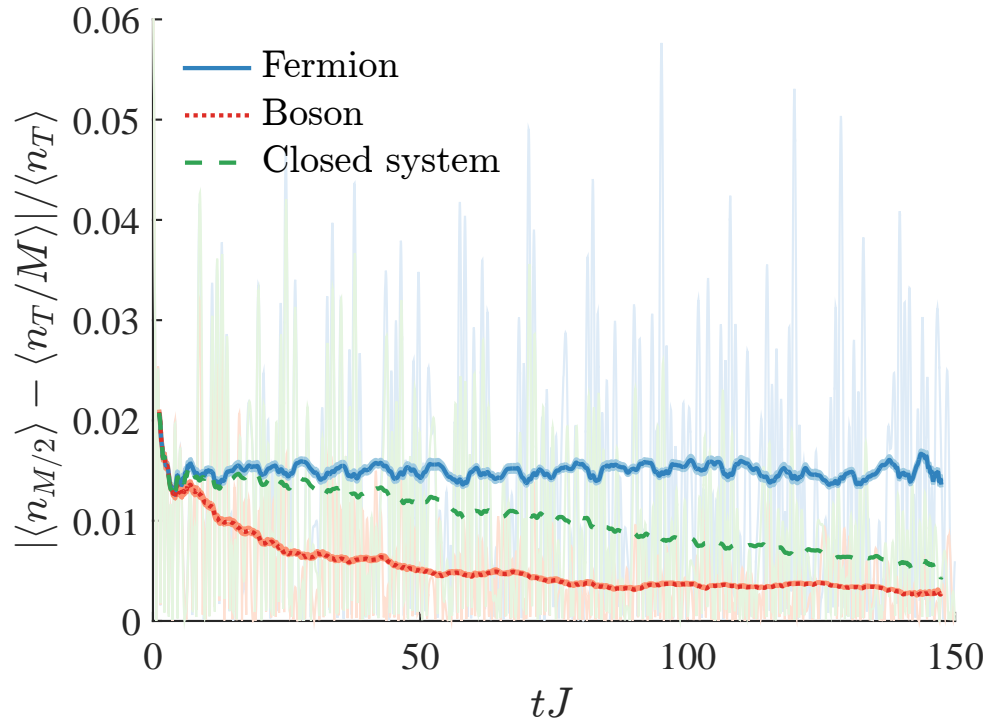


Figure 6.11: Evolution of the middle site density fluctuation from the expected long-time average $|\langle \hat{n}_{M/2} \rangle - \langle \hat{n}_T/M \rangle| / \langle \hat{n}_T \rangle$ for a system with $M = 16$, $n_0 = 0.5$, $J = 1$, $\gamma_l = 0.01$, $\gamma_d = 0$ and a closed system ($\gamma_l = 0$). We provide time-block averages (lines) with a block length of 50 data points of the full dataset (shades) for better visualization. We observe how the fermionic deviation remains approximately constant for the studied time while the bosons and the closed system approach the long-time expected average with the former exhibits smaller deviations.

6.4.4 Short-time imbalance profile

As a complementary result we present the short-time evolution of the system imbalance since these can be analytically calculated for the case of no onsite interaction (free fermions). In Fig.6.12, we observe a good agreement with the analytical results for all the curves before the revivals due to finite-size systems take place. After that, all numerical calculations depart from the analytical result. We also observe a higher damping in the oscillation of the bosons as it was the case when analyzing the local density in subsection 6.4.3 while fermions remain closer to the case of no losses (where both fermions and bosons coincide).

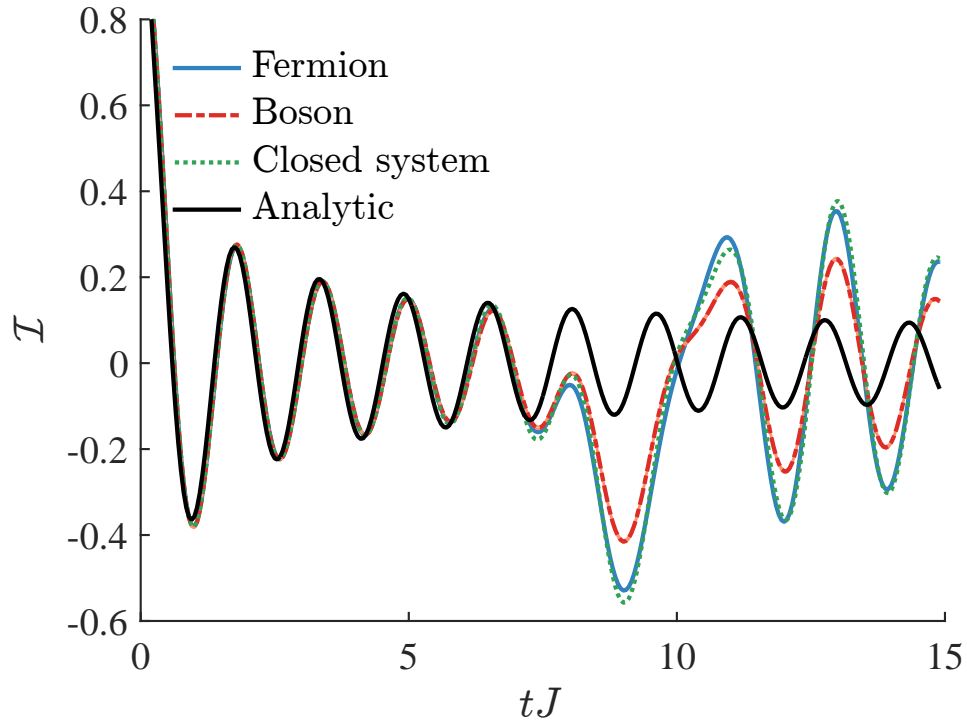


Figure 6.12: Short-time evolution of the system odd-even imbalance \mathcal{I} for a system with $M = 16$, $n_0 = 0.5$, $J = 1$, $\gamma_d = 0$. We compare the case of closed system ($\gamma_l = 0$), fermionic and bosonic systems subject to loss ($\gamma_l = 0.01$) and the analytical result for free fermions given by the zeroth order Bessel function $\mathcal{I} \propto J_0(4Jt)$.

6.5 Conclusion

In this chapter, we have proposed a method to probe particle statistics of the system, an inherent property of the closed system, through the use of dissipation. In this way, we have shown how particle losses generate differences even in local quantities for hardcore bosons and spinless fermions. We have identified relevant signatures in experimentally measurable observables such as local densities or entropies, which would behave remarkably different in the presence of loss. In addition, we have shown that losses produce differences between HCBs and fermions whether they are deterministically induced, or occur randomly due to natural experimental processes. Thus, studying losses in these system has proven not only relevant for the improved description of the experimental conditions but also insightful as it provides infor-

mation about closed-system properties, such as the particle statistics. Moreover, we have provided a careful analysis of the robustness of the differences proposed, testing how other dissipation sources, such as dephasing, or the presence of second-order terms would affect the results.

In the future, we would like to relate the measurements on section 6.3 with more general two-point correlation measurements as the quantities that we investigate are quite similar to them since they are given by $\propto \langle \hat{a}_i U(t) \hat{a}_k \rangle$.

Some other of the future directions are focused on systems with slow intrinsic time scales, like the case of many-body localized systems connecting with chapter 7. In particular, we would be interested in exploring how these analysis would apply to quasi-periodic systems, like the case of quasi-crystals, where disorder is not required. However, these system usually require increasing the dimensionality of the system and so our numerical algorithms would need to be extended.

Alternatively, we would be interested in applying neural-network-related techniques [155] (which connect with tensor network ideas) to the systematic distinction of particle statistics. We would like to explore if Machine Learning algorithms would help us not only distinguish particle statistics but also if they could provide information about the system by analyzing properties we obtain from tensor networks, such as the entanglement spectrum.

Chapter 7

Dynamics of many-body localization in the presence of particle loss

7.1 Introduction

In this chapter, we present the results included in our publication [139], which focuses on the role of single-particle loss in the dynamics of experiments to study many-body localization (MBL).

The question we address in this chapter arises in the context of current cold atomic experiments, whose development has allowed for the engineering of paradigmatic Hamiltonians for quantum simulation [1]. Despite the extreme control and tunability of these experiments, under certain circumstances our ability to describe them as perfectly isolated systems fails. All systems in nature are in some degree open systems, but our good understanding of dissipation on a microscopic level in cold gases allows us to systematically study these effects. In previous chapters (5 and 6) we explore the effects of engineered coupling to the environment and how our control over the system and environment interaction provides a novel toolbox for the state engineering in the lattice. However, now we take another perspective on the open system problem. Instead of focusing on the tunable control of the dissipation, we

study the case of an uncontrolled residual coupling to an external bath and its effect on the long-time dynamics in the system that can differ strongly from the closed system case.

In particular, our focus is on the study of many-body localized systems, an important example of systems with intrinsically long timescales [156, 157]. In the absence of dissipation, these systems fail to thermalize, breaking the system’s ergodicity even at infinite times. MBL has been experimentally observed both using trapped ions [158] and ultracold atom systems in optical lattices [26, 159, 160]. In the case of optical lattices, dephasing and particle loss have been experimentally observed [135] and prevent the localization to survive for the accessible experimental timescales ($\sim 1s$) as decoherence induces thermalization in the system. The failure of the closed system description gives rise to relevant effects in the observables that can be experimentally measured at intermediate times. Therefore, it is essential to properly describe both dephasing and single-particle loss, typically caused by incoherent photon scattering. While the former was widely studied in the past [136, 138, 137], showing that it can prevent localization even in the absence of inter-particle interaction, the role of particle loss in the MBL problem remains unclear and has only been addressed phenomenologically for specific initial conditions [138]. We focus on the case of fermionic systems in these dissipative dynamics, following recent experimental and theoretical work [131].

It is important to note that the inclusion of single-particle loss in our description poses certain challenges given the ‘non-local’ character of the fermionic annihilation operator¹. In order to provide an efficient description of the dynamics we present a method based on symmetry-preserving matrix product operators (following ideas introduced in section 4.1.6).

This method allows us to study the interplay of particle loss and dephasing in the MBL experiments, analyzing not only relevant observables but also how the dissipation affects the density operator and properties associated to it such as the bipartite entanglement.

¹We can infer this from a Jordan-Wigner transformation of the loss operator, see section 2.4.1.1.

This chapter is structured as follows in Sec.7.2 we provide an overview of the concept of thermalization in quantum system and why MBL systems fail to thermalize. In Sec.7.3, we introduce the concept of density imbalance, the equations of motion of the open system and the symmetry-preserving MPO method that we implement to calculate the evolution. In Sec.7.4, we summarize our main findings discussing the role of both dissipation sources for different parameter regimes. Finally, in Sec.7.5 we discuss the findings of this chapter and provide some ideas of interesting future directions to investigate based on our results.

7.2 Overview on MBL in cold atoms

7.2.1 Thermalization in quantum systems and Eigenstate Thermalization Hypothesis

Many-body localized states constitute an important example of the class of systems that do not thermalize. Thus, it is important to provide a criterion for thermalization in the context of quantum many-body systems.

In the context of a closed quantum system, we should discuss the operational understanding of what it means for the system to thermalize. The evolution of the closed system is unitary and, as a result, the system should retain information of its initial state as we could always evolve backwards to recover it. Moreover, given the unitary evolution any eigenstate of the Hamiltonian \hat{H} will give rise to stationary populations, consequently, if the state thermalizes this will occur at the level of individual eigenstates. Then, in these systems there should be a different mechanism that allows for the system to lose the information of its initial correlations.

We can summarize thermalization in the quantum context as the system relaxation to states where macroscopic observables become stationary as the system acts as its own bath, with local degrees of freedom (d.o.f.) entangling with each other and local quantum correlations being decohered. Moreover, when a quantum system thermalizes these observables can be predicted through statistical mechanics and are

universal – in the sense that they do not depend on the initial conditions.

In order to specify what we meant from the previous statement, let us divide our total quantum system, composed by a set of D d.o.f., into a subsystem S and a bath B containing all the d.o.f. we have not included in S .

If the subsystem thermalizes S , the reduced density operator ρ_{sys} should be dictated by statistical mechanics. And thus, it should coincide with the thermal equilibrium density operator $\rho_{\text{sys}}^{\text{eq}}$, defined for a system to be at equilibrium at temperature T :

$$\rho_{\text{sys}}^{\text{eq}} = \text{Tr}_{\text{bath}} (\rho_{\text{tot}}^{\text{eq}}) = \text{Tr}_{\text{bath}} \left(e^{-\beta E_{\text{eq}}} / \text{Tr} (e^{-\beta \hat{H}}) \right), \quad (7.1)$$

with $\rho_{\text{tot}}^{\text{eq}}$ the thermal density operator of the total system and E_{eq} the total energy at equilibrium. Thus, the equilibrium operator contains no information of the initial state.

In order to establish the comparison between ρ_{sys} with $\rho_{\text{sys}}^{\text{eq}}$ we need to take both the long-time and the thermodynamic limit. The latter is taken by increasing the d.o.f. in the bath, while keeping the size of S unchanged. Thus, the condition for thermalization can be written as [156]:

$$\lim_{D \rightarrow \infty} \left(\lim_{t \rightarrow \infty} \rho_{\text{sys}}(t) \right) = \lim_{D \rightarrow \infty} \rho_{\text{sys}}^{\text{eq}}. \quad (7.2)$$

Now that we have a criterion to evaluate thermalization, we require an expression for $\rho_{\text{sys}}(t)$. We can decompose it into the eigenbasis of the system $\{|n\rangle\}$ with $\hat{H}|n\rangle = E_n|n\rangle$, so that every matrix element of the density operator is given by $\rho_{nn'}(t) = \langle n | \rho_{\text{sys}}(t) | n' \rangle = \rho_{nn'}(0) e^{-i\hbar(E_{n'} - E_n)t}$. Note that then, $\rho_{nn}(t) = \rho_{nn}(0)$. Moreover, if the system thermalizes it should do so regardless of its initial state, implying that every eigenstate of the many-body Hamiltonian, which correspond to a stationary density operator $\rho^{(n)}(t) = \rho^{(n)}(0) = |n\rangle\langle n|$ is indeed thermal. This is known as the Eigenstate Thermalization Hypothesis (ETH) [161, 162, 163].

Hence, from the ETH we can associate a temperature T_n with the system such that $E_n = \langle \hat{H} \rangle_{T_n}$. Furthermore, if the system is in an eigenstate, it can be described

simply again by $\rho^{(n)}$ and $\rho_{\text{sys}}^{(n)}(t) = \rho_{\text{sys}}^{(n)}(0) = \text{Tr}_{\text{bath}}(|n\rangle\langle n|)$, which in the thermodynamic limit corresponds to $\rho_{\text{sys}}^{(n)} = \rho_{\text{sys}}^{\text{eq}}(T_n)$.

It is important to consider that we usually do not have access to the density operator but rather need to establish our analysis on the level of observables. For a given initial state $|\phi(0)\rangle = \sum_n c_n |n\rangle$, the time evolution is given by $|\phi(t)\rangle = \sum_n c_n e^{-iE_n t} |n\rangle$. Hence, we can express the time evolution of the expectation value of an operator \hat{O} as:

$$\langle \hat{O} \rangle = \sum_{n,n'} c_n^* c_{n'} e^{i(E_n - E_{n'})t} \langle n | \hat{O} | n' \rangle. \quad (7.3)$$

In order to obtain the thermal value for the expectation value we can take the long-time and time-averaged limit [161]:

$$\langle \hat{O} \rangle_{\text{thermal}} = \lim_{T \rightarrow \infty} \frac{1}{T} \int dt \sum_{n,n'} c_n^* c_{n'} e^{i(E_n - E_{n'})t} \langle n | \hat{O} | n' \rangle = \sum_n c_n^2 \langle n | \hat{O} | n \rangle. \quad (7.4)$$

This result only depends on the matrix elements of this operator and the state coefficients in the eigenbasis of \hat{H} . And, more importantly, it coincides with the value obtained from statistical mechanics using the microcanonical ensemble for a system with energy E_n (for a detailed discussion on this comparison see [161]). Systems that satisfy Eq.(7.4) are denoted as ergodic². Hence, ergodicity is responsible for the emergence of local thermodynamic equilibrium in the system.

7.2.2 Localization in quantum systems

This chapter focuses on systems that do not satisfy the ETH and so, they do not thermalize. In particular, we are interested in a subset of such states known as many-body localized states. The discussion presented in subsection 7.2.1 does not apply to many-body localized states.

Localization in quantum system was already reported by Anderson at the level of single particles [164] with a model consisting of a single particle tunneling in an

²Note that the definition of ergodic systems is different in other contexts.

infinite lattice with a random onsite potential or random tunneling elements. The version including random potentials can be simply described through a tight-binding model (as described in chapter 2) plus a local offset term

$$\hat{H} = -J \sum_{\langle ij \rangle} (\hat{c}_i^\dagger \hat{c}_j + \text{h.c.}) + \sum_i (\Delta_i \hat{c}_i^\dagger \hat{c}_i), \quad (7.5)$$

with J the tunneling amplitude, \hat{c}_i the annihilation operator of a particle in site i and Δ_i the random local potential in every lattice site. Note that $\langle ij \rangle$ denotes a sum over nearest neighbour sites. Despite the simplicity of the model, this system shows exponentially localized eigenstates and fails to thermalize. This has been observed experimentally in a large variety of systems [165, 166, 167], including cold atoms [168, 169, 170].

The concept of Anderson localization can be extended to the case of interacting particles, which is known as MBL [171, 172, 173, 174]. In the case of MBL, all eigenstates exhibit localization for high disorder values [175]. However, for weaker disorders the theoretical analysis points at numerical evidence of localization of only certain eigenstates in 1D [176] in contrast to Anderson localization. Therefore, the system undergoes a phase transition depending on the disorder strength, passing from a thermal stationary state that follows ETH to a localized ‘non-ergodic’ phase that violates ETH. It is important to mention that this phase transition not only occurs for random disorder but it is also present in quasiperiodic systems [177] when the periodicity is larger than the system size. This is the case of the Aubry-André model [178]. Lately, the use of digital micromirror devices has permitted to implement random potentials on demand (for experimental details see [25]) complementing the use of incommensurate pseudorandom models.

The many-body-localized-to-thermal quantum phase transition has been the focus of great experimental effort in the recent years, leading to conclusive observations in 1D [26], quasi-2D [159] and 2D [160]. The case of 2D is specially interesting as it becomes theoretically challenging to study and only recently certain thermalizing phases have been reported [179] that could destabilize MBL in 2D.

Finally, one of the more important points and the one we focus in is the fact that in any experimental setups the presence of decoherence plays an important role in the long-time limit, in particular in the case of MBL, which is a phenomenon that we associate with closed systems. More specifically, incoherent light scattering causes both dephasing and particle losses. Both dissipative processes eventually leads to thermalization at long times due to dissipation even for deeply localized regimes [135]. Hence, it is essential to understand the role of both of these dissipation sources and their interplay in the MBL phase transition. This is the focus of the rest of this chapter.

7.3 System description

7.3.1 Imbalance: experimental figure of merit

The calculations that we present in this chapter are tightly connected to the experiments with fermionic atoms mentioned in the introductory sections (see [26, 135]). In particular, we focus on simulating the most important observable in these experiments that is the odd-even density imbalance \mathcal{I} . We already introduced \mathcal{I} briefly (see section 6.4.1) when comparing dissipative dynamics of different particle statistics and it is given by:

$$\mathcal{I} = \frac{n^o - n^e}{n^o + n^e}, \quad (7.6)$$

where $n^{o/e} = \sum_{i \in \text{odd/even}}^M \langle \hat{n}_i \rangle$ and \hat{n}_i is the number operator on site i . The imbalance allowed us to observe distinct behaviour in bosonic or fermionic systems. However, in those calculations we did not consider any disorder term in the dynamics and, as a result, the systems were deeply in the ergodic phase.

Here the perspective is slightly different as the imbalance is not used to highlight differences in particle statistics but rather to distinguish if the state is in the ergodic or non-ergodic phase focusing on fermionic atoms only. Monitoring the imbalance is a common procedure in the MBL experiments as we briefly describe now.

The fermionic atoms in the optical lattice can be described by the following Hamiltonian:

$$H = -J \sum_i (\hat{c}_i^\dagger \hat{c}_{i+1} + h.c.) + \sum_i V_i \hat{n}_i + U \sum_i \hat{n}_i \hat{n}_{i+1}. \quad (7.7)$$

Here, $\hat{n}_i = \hat{c}_i^\dagger \hat{c}_i$, where \hat{c}_i^\dagger creates a fermion on site i , and $V_i \in [-h, h]$ are on-site energies, which are independent uniformly distributed random variables. This Hamiltonian composed by a tunneling term with amplitude J , a random onsite contribution and a first-neighbour interaction term with constant U , has been extensively studied as a model (closed) system and (for $U = 2J$) is expected to be localized for $h \gtrsim 7.2J$ [176, 180, 181].

In these experiments, the atoms are initially prepared in a charge-density-wave (CDW) state with single-atoms occupying all the odd sites. This is achieved by superimposing a second lattice with associated wavelength $\lambda_2 = 2\lambda_{lat}$ creating a superlattice structure where it is possible to systematically load atoms only in the odd sites. As a result, at $t = 0$ the value of the imbalance is $\mathcal{I} \approx 1$ and atoms are systematically prepared in an approximately pure state. Then, as particles are allowed to tunnel the imbalance evolves over time. This can be monitored by measuring the population of the odd or even sites with a superlattice band-mapping technique or considering individual site populations with a quantum gas microscope.

By monitoring the imbalance at long times, we learn about the thermalization properties of the system. This is due to the fact that in the absence of dissipation \mathcal{I} exhibits a fast initial decay followed by a damped oscillatory behaviour towards a steady value. In the ergodic phase, the imbalance vanishes at long times $\mathcal{I}(t \rightarrow \infty) = 0$. However, if the state of the system is localized it fails to thermalize and thus the initial correlations do not completely disappear. As a result, the imbalance will relax to a finite value after the transient oscillations. Therefore, the imbalance provides an accessible experimental witness for the MBL quantum phase transition.

7.3.2 Open system dynamics

In order to compute the dynamics of such systems coupled to a reservoir we can make use of the techniques presented in chapter 3 and 4. In particular, as the Born-Markov approximation is applicable in the current system we describe it through a master equation (see section 1.3). Moreover, we map the problem to the language of MPS (chapter 4) solving both the master equation directly and also making use of quantum trajectories (section 3.3.2). In both cases, we compute time evolution through TEBD (section 4.3).

As we discussed in chapter 3, the time evolution of a system coupled to a Markovian bath is governed by the master equation in the Lindblad form (see 1.3) for the density matrix given by the following expression:

$$\frac{\partial}{\partial t}\rho = \mathcal{L}[\rho] = -i[\hat{H}, \rho] + \sum_i \gamma_i \left(\hat{L}_i \rho \hat{L}_i^\dagger - \frac{1}{2} \{ \hat{L}_i^\dagger \hat{L}_i, \rho \} \right), \quad (7.8)$$

where \mathcal{L} is denoted as Lindbladian operator, here \hat{L}_i are the jump operator that describe the dissipation process on site i with amplitude γ_i . Since our interest is to model events that occur naturally in experiments, we consider single-particle loss, i.e., $\hat{L}_i = \hat{c}_i$ [129], as well as dephasing or local density measurement with $\hat{L}_i = \hat{n}_i$ [130, 131].

7.3.3 Bond-Parity Matrix-Product-Operator Formalism

In section 6.2.1, we already highlighted the difficulty of simulating fermionic losses in the language of MPS due to their ‘non-local’ character that we can formalize using a Jordan-Wigner transformation. In that case, we made use of number-conserving representation of MPS to overcome the difficulty. In this chapter we will combine this technique with similar ideas on the level of the density operator to represent fermionic losses.

Our objective is to represent the density operator and its evolution (given by Eq.7.8) in an efficient way in the language of MPO (section 4.2). As a reminder, a state in the MPS form can be written as

$$|\psi\rangle = \sum_{i_1, i_2, \dots, i_M} \text{Tr}(A^{i_1} \dots A^{i_M}) |i_1 \dots i_M\rangle, \quad (7.9)$$

where each A^{i_n} is a tensor with dimension $D \times D$ per physical index i_n . For spinless fermions, the physical index i_n represents the local occupation, i.e., the Hilbert space is spanned by all $|n_1 n_2 \dots\rangle = \prod_{\{i\}} \hat{c}_i^\dagger |vac\rangle$, where the product runs over the set $\{i\}$ of occupied sites and $|vac\rangle$ represents the vacuum state with no particles. This representation can be adapted to represent a vectorized version of the density operator (see 4.4.2). Alternatively, we can also represent it by an MPO as we choose here.

Given a density operator described in the occupation basis

$$\rho = \sum_{n_1, n_2, \dots, n_M} \sum_{n'_1, n'_2, \dots, n'_M} \rho_{\{n'_i\}}^{\{n_i\}} |n_1 \dots\rangle \langle \dots n'_1|, \quad (7.10)$$

the first term that we need to consider from Eq.7.8 is $\hat{L}_i \rho \hat{L}_i^\dagger$. If we focus on the case of single-particle loss ($\hat{L}_i = \hat{c}_i$), we immediately observe that $\hat{L}_i \rho \hat{L}_i^\dagger$ terms acquire a phase related to the particle number to the left of site i for each \hat{L}_i :

$$\hat{L}_i \rho \hat{L}_i^\dagger = \hat{c}_i | \cdot \hat{n}_i \cdot \rangle \langle \cdot \hat{n}'_i \cdot | \hat{c}_i^\dagger = (-1)^{N_{<i} + N'_{<i}} | \cdot (\hat{n}_i - 1) \cdot \rangle \langle \cdot (\hat{n}'_i + 1) \cdot |, \quad (7.11)$$

where $N_{<i} = \sum_{j<i} \langle \hat{n}_j \rangle$. The state of the system only differs in the occupation on site i in both sides of the equation. We can define the phase arising in this product of operators as the bond parity $\mathcal{P}_i = (-1)^{N_{<i} + N'_{<i}}$, which is a highly non-local operator as it depends on populations on sites $1, \dots, i-1$. In principle, we should consider all the other terms in Eq.(7.8), however, they are all quadratic in $\hat{c}_i^{(\dagger)}$ and so all phases cancel. As an example, we can consider the term $\hat{L}_i^\dagger \hat{L}_i \rho$ whose bond parity is $(-1)^{2N_{<i}} = 1$.

In order to implement the bond-parity in our operator representation let us separate the Lindbladian into bond and single-site terms:

$$\mathcal{L}[\rho] = \mathcal{L}^{(2)}[\rho] + \mathcal{L}^{(1)}[\rho], \quad (7.12)$$

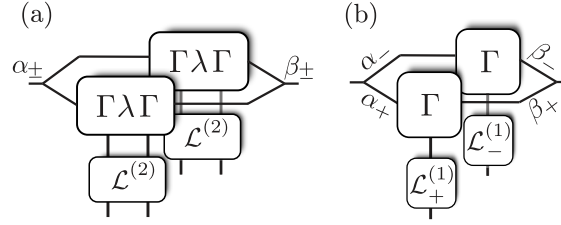


Figure 7.1: Schematic of a TEBD step for updating the MPO matrices Γ and λ , preserving the subspaces $\mathcal{P} = \pm 1$. (a) For the bond terms, the same operator $\mathcal{L}^{(2)}$ is applied in each subspace. For the case (b) of the single-site Lindblad superoperators, each block $\mathcal{P} = \pm 1$ has its own single-site operator $\mathcal{L}^{(1)}_{\pm}$ applied in the respective subspace. The sets of indices α_{\pm} and β_{\pm} correspond to the subspaces with associated quantum numbers $\mathcal{P} = \pm 1$.

where $\mathcal{L}^{(2)}$ contains the unitary evolution, and $\mathcal{L}^{(1)} = \left(\sum_i \hat{L}_i \rho \hat{L}_i^{\dagger} - \frac{1}{2} \{ \hat{L}_i^{\dagger} \hat{L}_i, \rho \} \right)$ contains only single-site terms. As we explained only terms in $\mathcal{L}^{(1)}$ can exhibit a non-vanishing phase. We can split those terms further into

$$\mathcal{L}_{i,\pm}^{(1)}[\rho] = \gamma_i \left(\pm \hat{c}_i \rho \hat{c}_i^{\dagger} - \frac{1}{2} \{ \hat{c}_i^{\dagger} \hat{c}_i, \rho \} \right), \quad (7.13)$$

The key point of our representation comes from the fact that both single-site and bond terms preserve the bond parity on the left and right bond from the site where they are applied (only modify local parity). As a result, the system has bond parity symmetry and so all updates in our MPO can be performed in the subspaces of $\mathcal{P}_i = \pm 1$ (similar to the implementation with number-conserving representation in section 4.1.6).

We can adapt the TEBD algorithm (section 4.3) to density operators [182], which we can express using Vidal's notation (section 4.1.5). Hence, the expression in Eq.(7.10) takes the form:

$$\rho = \sum_{j_1, j_2, \dots, j_L} \text{Tr} \left(\lambda^0 \Gamma^{j_1} \lambda^1 \dots \Gamma^{j_L} \lambda^L \right) \sigma^{j_1} \otimes \dots \otimes \sigma^{j_L}. \quad (7.14)$$

Here, σ^j forms a basis for the 2×2 matrices (corresponding to the local bond dimension of ρ , $d = 4$), we choose to use the Pauli matrices together with the identity σ^0 . The physical indices then come with respective (bond parity) quantum

numbers $+1$ for the diagonal σ^0 and σ^3 and -1 for σ^1 and σ^2 .

Now, that the density operator has been constructed in the MPO form we can decompose the Lindbladian into two-site Trotter gates (section 4.3), in this case using second order TEBD where we account for even and odd bond operators $\mathcal{L}^{(e)}$ and $\mathcal{L}^{(o)}$:

$$e^{\mathcal{L}t} \approx \left(\Pi e^{\frac{\Delta t}{2N} \mathcal{L}^{(1)}} \Pi e^{\frac{\Delta t}{2N} \mathcal{L}^{(e)}} \Pi e^{\frac{\Delta t}{N} \mathcal{L}^{(o)}} \Pi e^{\frac{\Delta t}{2N} \mathcal{L}^{(e)}} \Pi e^{\frac{\Delta t}{2N} \mathcal{L}^{(1)}} \right)^N. \quad (7.15)$$

In the same spirit as in section 4.1.6, we can modify the bond index keeping track of the parity by including in each bond index α_i a map $\mathcal{P} : \alpha_i \rightarrow \pm 1$. As a result of the incorporation of this symmetry, when a Trotter gate is applied we distinguish two situations:

1. Gates composed by bond operators (no sign associated) are applied as shown in Fig.7.1(a) regardless of the parity sector for the update of the state.
2. For single-site terms, the corresponding phase has to be applied to the operator in order to preserve the parity subspaces, see Fig.7.1(b). For the case of other jump operators, such as dephasing, as they are quadratic in \hat{c}_i , $\hat{L}_i = \hat{n}_i$, $\mathcal{L}_{i,+}^{(1)}[\rho] = \mathcal{L}_{i,-}^{(1)}[\rho]$ this procedure becomes trivial.

As a result, the state is updated during the time evolution preserving the parity sectors. The most important consequence is that, as we achieved in chapter 6, by incorporating a symmetry in the system we have access to the sign associated with the loss event for every parity sector. Then, we do not need to compute the non-local term $N_{<i} = \sum_{j<i} \hat{n}_j$ and so every update is local in the parity preserving representation.

Moreover, the MPO representation of the density operator allows for the simulation of mixed initial states and complements the calculations that we can achieve through the use of stochastic evolution in the form of quantum trajectories (as in chapter 6). In this chapter, we will combine both methods taking close attention at how both perform. In particular we focus on the analysis of the entanglement entropy (for the pure state evolution) and its comparison with the operator-space entanglement entropy (OSEE), which measures the factorizability of the density matrix [183] and is a measure for the efficiency of the matrix product formalism. We discuss the findings on this comparison in section 7.4.4.

7.4 Results

Here, we summarize the main results obtained from numerical simulations that we computed with the formalism presented in the previous section. We focus primarily on the evolution of the imbalance (described by Eq.(7.7) and (7.8)) and how its profile is affected by the different dissipation sources, namely dephasing and single-particle loss (with respective coupling rates γ_d and γ_l). Our initial state is chosen to be the perfect CDW with one fermion in every odd site initially and we use numerical parameters $D = 100$ (bond dimension) and $\Delta t = 0.1 [1/J]$, unless we indicate otherwise.

7.4.1 Pure loss

The first case that we analyze is the effect of single-particle loss alone while in the localized regime since dephasing has been studied in depth in the past [136, 138, 137]. We can understand the effect of loss in the system for both, weak and strong, interactions in the system from a phenomenological approach. But first let us provide some intuition for the two extreme cases:

1. In the limit of no interactions we expect the imbalance to be unaffected by losses. This is due to the fact that the population decrease, which follows an exponential decay, is homogeneous along the lattice. Since the imbalance is a normalized quantity that depends on the relative population it should remain unaffected.
2. However, in the presence of first-neighbour interactions ($U \neq 0$) the picture becomes more complex. In this case, eliminating a particle from the lattice modifies the energy of atoms in neighbour sites, enabling in many cases particle hopping. A relevant example, in the strong coupling regime (i.e., $U \gg J$) where the system is close to an eigenstate and any tunneling event from the initial configuration $|101010\dots\rangle$ is energetically prohibitive, causing that $\mathcal{I}(t \rightarrow \infty) \sim 1$. Thus, we expect that in the presence of losses the imbalance relaxes to a lower value as the removal of a particle enables system dynamics. Moreover, after the particle density has been reduced sufficiently the system becomes effectively non-interacting.

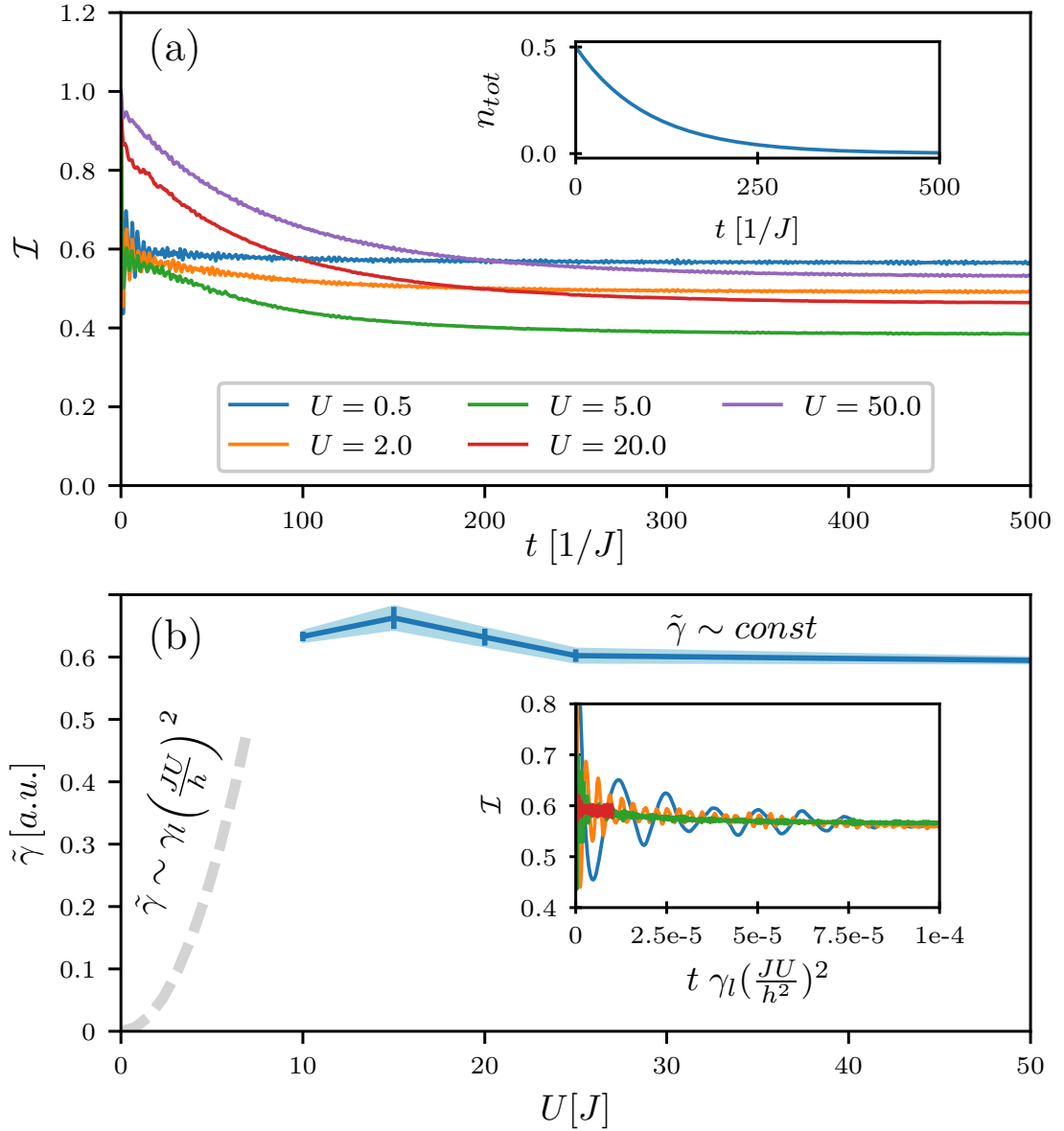


Figure 7.2: (a) Dynamics of the imbalance and particle density (inset) for loss only ($\gamma_l = 0.01$) for $h = 10J$, $N = 20$, and $U/J = 0.5 \dots 50.0$. (b) Effective decay rate of the imbalance extracted via a fit to Eq.(7.17) for $U \geq 10J$. For $U/J = 0.5, 1.0, 2.0$ and 5.0 , the qualitative behavior (gray dashed line) is confirmed via a collapse of the imbalance time traces by scaling the time with $\gamma_l J (JU/h^2)^2$ (inset).

The behavior of the imbalance in the presence of loss can be qualitatively described in a mean-field picture, where the time evolution of the imbalance can be approximated by [138, 137]

$$\frac{d\mathcal{I}}{dt} \approx -\gamma_{\text{eff}}(t)\mathcal{I}(t) \approx -\gamma n(t)\mathcal{I}(t) = -\tilde{\gamma}e^{-\gamma t}\mathcal{I}(t), \quad (7.16)$$

where $n(t) = n_0 \exp(-\gamma t)$ is the particle density and $\tilde{\gamma} = \gamma n_0$ is an effective decay rate. Integrating (7.16) yields the time dependence for the imbalance

$$\mathcal{I}(t) \propto \exp \left\{ - \left[\frac{\tilde{\gamma}}{\gamma t} (1 - e^{-\gamma t}) \right]^\beta \right\}. \quad (7.17)$$

The exponent β can be introduced phenomenologically as done here, to account for the fact that the mean-field picture is a simplification [138] and as it provides a better fit to the numerical results. At short times, where $\gamma t \ll 1$ the imbalance can be approximated by a stretched exponential:

$$\mathcal{I}(t) \approx I_0 \exp[-(\tilde{\gamma}t)^\beta]. \quad (7.18)$$

This behaviour is confirmed by the results provided in Fig.7.2(a) where we represent the evolution of the imbalance in the ‘non-ergodic’ regime ($h = 10J$), for different first-neighbour interaction strengths. We observe an initial rapid decay in the imbalance that occurs faster with increasing U . At long times, the imbalance saturates to a non-zero value (even in the limit of vanishing particle number, see inset of Fig.7.2(a)). In the regime of $U \ll h$ the initial decay can be calculated perturbatively and is expected to scale as $\gamma_i(JU/h^2)^2$ [138]. On the other hand, for large interactions we note that the initial decay is independent from the value of U and curves only differ in the long-time limit of the imbalance. In Fig.7.2(b) we analyze the value of the effective decay rate $\tilde{\gamma}$. We observe that for interactions $U \geq 10J$, Eq.(7.17) provides a robust fit with an estimated $\beta \approx 0.9$ approximately constant. For smaller interactions, we confirm the initial decay rate $\tilde{\gamma} \propto U^2$ via a data collapse of the time traces shown in the inset of Fig.7.2(b).

7.4.2 Dephasing and loss: weak interactions

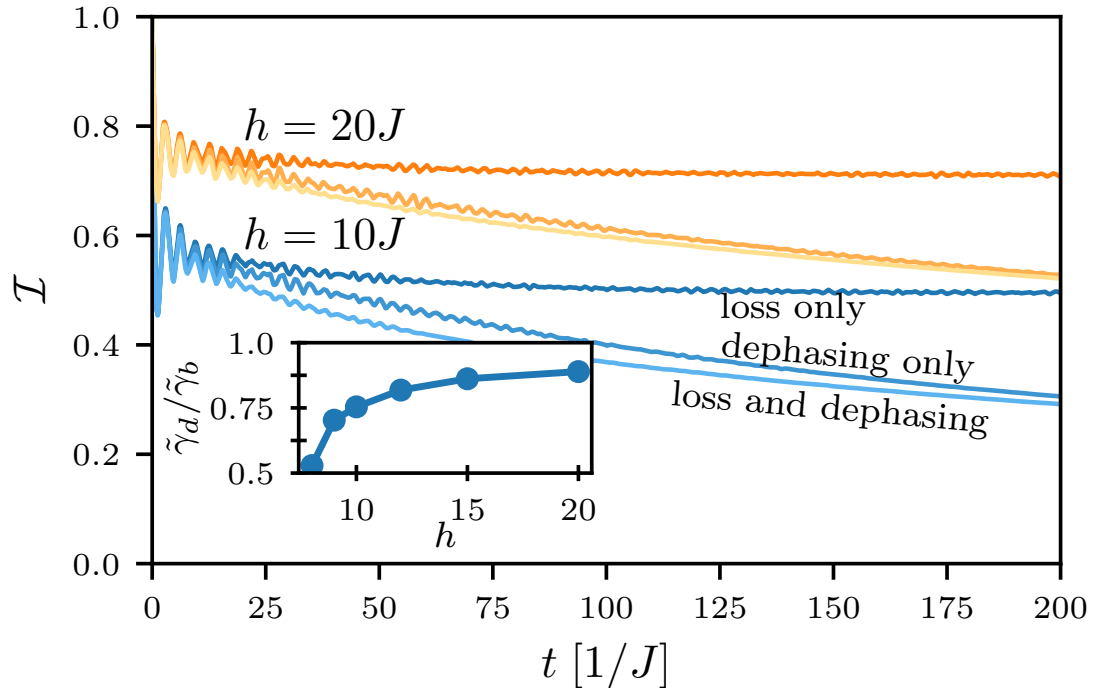


Figure 7.3: Imbalance dynamics in the presence of dephasing and loss for intermediate interactions $U = 2J$ and disorder $h = 10J$ (lower traces) and $h = 20J$. The more rapidly decaying traces represent the cases of both dephasing and loss combined $[(\gamma_d, \gamma_l) = (0.02, 0.02)]$. The ‘loss only’ (‘dephasing only’) traces have $(\gamma_d, \gamma_l) = (0.0, 0.02)$ $[(0.02, 0.0)]$. The inset shows the ratio $\tilde{\gamma}_d/\tilde{\gamma}_b$ of the decay rates extracted from pure dephasing and the combination of both dephasing and loss, respectively. For larger disorder the decay rate is dominated by the dephasing, as shown by this ratio approaching unity.

Now that we have analyzed the effects of single-particle loss, it is important to understand the interplay with other dissipation phenomena, namely dephasing. We will consider independently the case of weak and strong first-neighbour interactions.

The results associated with weak interaction ($U = 2J \ll h$) are included in Fig.7.3. As it was the case with the inclusion of losses, the addition of dephasing to the system reduces the overall imbalance and reduces localization. However, dephasing leads to

constant dissipation in the system rather than to a saturation (imbalance does not plateau at the end of the simulated times). As a result, loss has only a subleading effect in this scenario, especially for strong disorders. This comparison between the effect of both dissipation sources is examined in the inset of Fig.7.3 where we consider the values of the initial decay rate³ in the presence of dephasing only $\tilde{\gamma}_d$ and with both loss and dephasing $\tilde{\gamma}_b$. The inset highlights the leading role of dephasing in the weak interaction case. This result is consistent with recent experiments [135].

7.4.3 Dephasing and loss: strong interactions

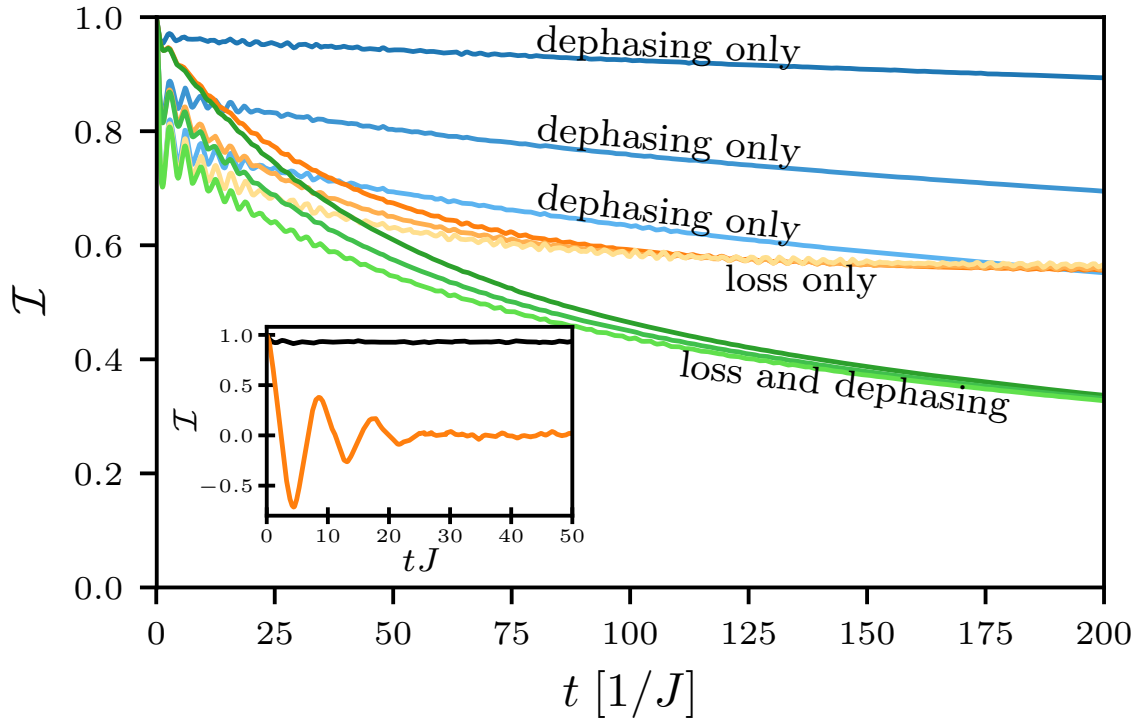


Figure 7.4: Imbalance evolution for pure dephasing (blue), pure loss (orange), and both (green) for densities $n = 0.5, 0.4$, and $n = 0.3$ (top to bottom, increasingly lighter colors) for large interactions, $U = 50J$. Here, $\Delta t = 0.025[1/J]$ was used. Inset: Imbalance evolution for an ergodic system, $h = 0.1J$, for a closed system (black) and pure loss (for $N = 12$ sites).

³Obtained by a fit to a stretched exponential decay, see Eq.7.17 and Eq.7.18, for several disorder strengths.

If we consider stronger interaction values it is important to recall the intuitive picture provided in section 7.4.1, where we indicated that in the limit of strong interaction, the CDW state is approximately an eigenstate of the Hamiltonian, with dissipation-induced tunneling scaling as $1/U^{24}$. In this scenario, dephasing alone cannot generate sufficient tunneling events to have a strong impact in the imbalance and dynamics are approximately frozen. As a result, particle loss, which produces strong differences in the energy landscape of neighbouring sites, is expected to be dominant. This is highlighted in the inset of Fig.7.4 where loss enables dynamics in the system, compared to the closed system where CDW is approximately constant and dynamics are effectively suppressed (note that here we are not requiring strong disorder).

This is confirmed in Fig.7.4, where we choose $U = 50J \gg h$. If we compare the darker lines of each colour (corresponding to $n = 0.5$ for loss only, dephasing only and both dissipations) we observe that loss reduces strongly the imbalance of the system compared to dephasing. In the presence of both dissipation sources, dephasing causes a significant decay in the long-time imbalance due to the fact that after a sufficient number of atoms have been eliminated from the lattice (the CDW is no longer an eigenstate) dephasing-induced hopping events become more likely.

Hence, it is important to investigate how this interplay between dephasing and particle loss takes place with initial configurations with $n \neq 0.5$ that can be affected by dephasing from earlier stages. In Fig.7.4 we include results associated to density-wave states with densities of $n = 0.4, 0.3$ (lighter shades), which is easily incorporate in the density operator MPO representation. We observe that in the three dissipation scenarios decreasing initial densities lead to smaller values of imbalance at the initial times. The effect of dephasing (blue curves) is enhanced strongly by the decreasing densities as we predicted since the interaction cannot prevent tunneling events in every site. Interestingly, in the case of pure loss (orange lines), even though the transient profiles differ from each other the steady imbalance is independent of the initial density. Finally, in the presence of both dissipation sources (green lines) we

⁴This factor is obtained by using perturbation theory in the limit of large U , see [138].

observe that the dependence at long times with the initial density is again rather small.

7.4.4 Evolution of entanglement entropy

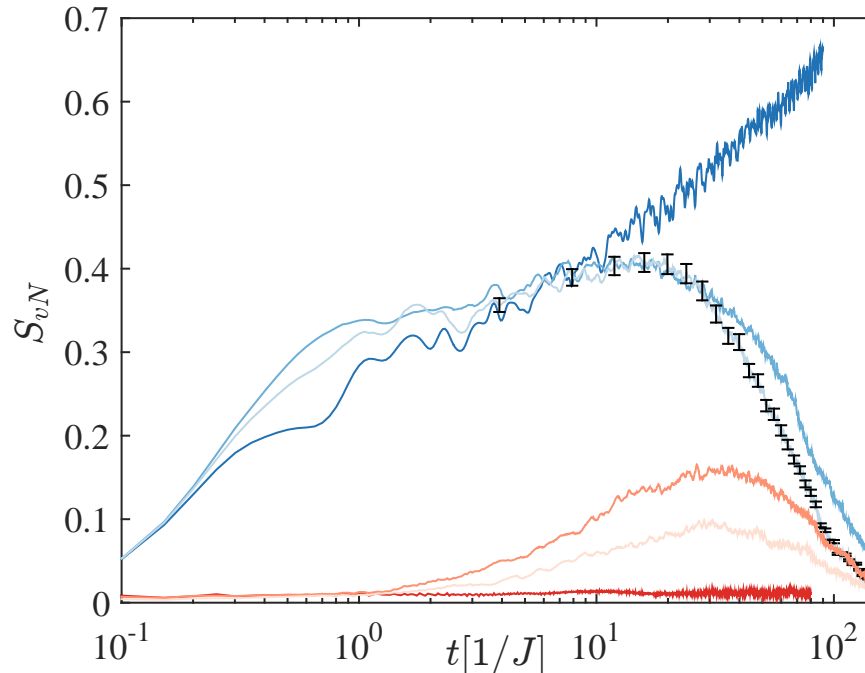


Figure 7.5: Evolution of the Von Neumann entropy S_{vN} of the middle bond $i = N/2$ of the lattice for a system with $N = 20$ and disorder strength $h = 10J$. We include results for $U = 2J$ (blue lines) and $U = 50J$ (red lines) including the closed system scenario, pure loss and loss and depasing (from darker to lighter). these results are obtained with a quantum trajectory approach (pure state evolution), with numerical parameters $D = 250$, $\Delta t = 0.001 [1/J]$. Errorbars come from trajectory averaging and are included in one of the curves only to facilitate visualization as the rest present similar errors.

As a final study beyond the experimental observables, we are interested in investigating the efficiency of the different approaches that we can use to simulate dissipative dynamics in this system. In particular, we want to study the entanglement entropy, both in the pure state and in the density operator approach. This provides an insight on not only the entanglement properties of the system but also on the bond dimension

cost of representing it through MPS. We focus again on the localized regime starting from a pure CDW state.

On the one hand, for the case of a pure state evolution, as it is for quantum trajectories, we consider the Von Neumann entropy as introduced in section 4.1.4, given by

$$S_{vN} = - \sum_{l_i}^{r_i=1} (\lambda_i)^2 \log(\lambda_i)^2, \quad (7.19)$$

with l_i the index over the bond dimension at bond i and r_i the Schmidt rank of the bipartition. The Von Neumann entropy is an essential quantity as it indicates the amount of entanglement existing between system bipartitions. In the context of open systems, S_{vN} also accounts for the entanglement of the system with its environment so it cannot be used as a measure of entanglement within the system itself. However, since the MPS representation can only support a limited bipartite entanglement $S_{vN} \leq \log(D)$ for a given bond dimension D , studying S_{vN} provides a useful indication into the efficiency of the MPS representation.

In Fig.7.5 we represent the Von Neumann entropy in the middle bond of the lattice and its dependence with both the interaction strength U and the different dissipation mechanisms in the ‘non-ergodic’ regime. For strong interactions ($U = 50J$, red curves) we observe moderate entanglement in the system; this is specially dramatic in the closed system case where no dissipation can enable dynamics and the CDW (close to an eigenstate) is approximately frozen. The addition of dissipation in the system enables dynamics increasing the value of S_{vN} . Interestingly, the addition of dephasing reduces the overall entropy as it disentangles the system. In the case of weak interactions ($U = 2J$, blue curves) we observe the logarithmic growth of entanglement for the closed localized systems, limiting our ability to model them at long times. The addition of dissipation, prevents this growth; this can be easily understood as removing particles from the system prevents the survival of long-range correlations along the system. In this case, dephasing has a subleading effect in contrast with what we observe in the case of OSEE as we explain below.

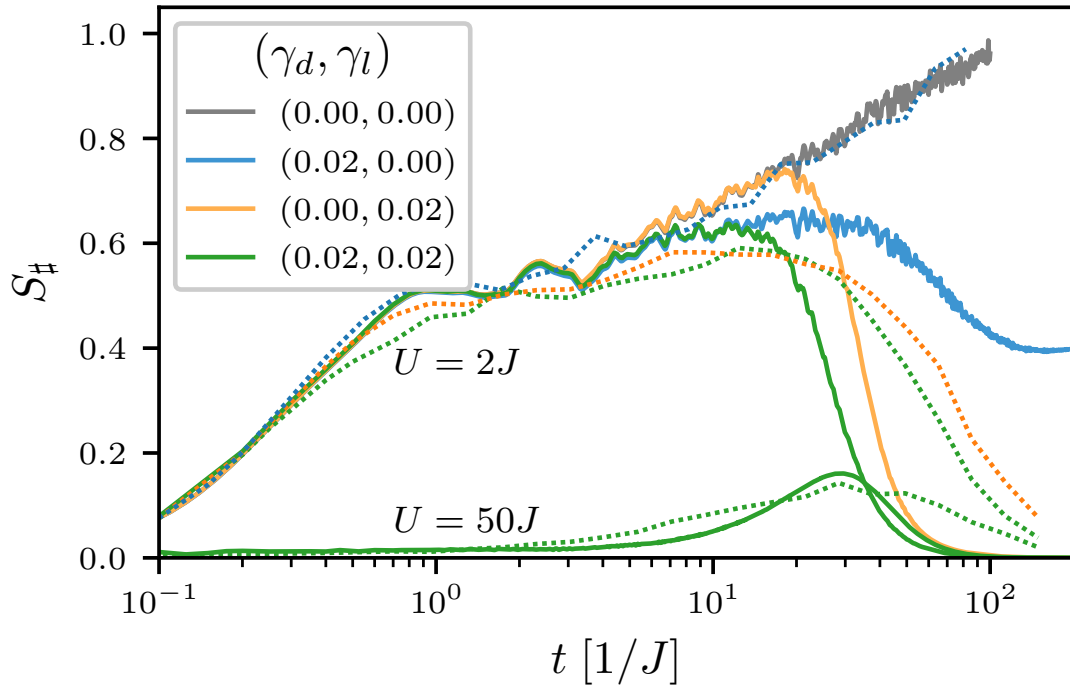


Figure 7.6: Evolution of the OSEE for $U = 2J$ and $U = 50J$ and disorder strength $h = 10J$ (solid lines) and the entanglement entropy obtained from quantum trajectory simulations (dashed lines). We used a base d , corresponding to the local Hilbert space dimension in each method, for the logarithm of the respective entropy for better comparison. The timestep used for the OSEE was $\Delta t = 0.005$ $[1/J]$. For the quantum trajectories a timestep of size $\Delta t = 0.001$ $[1/J]$ and bond dimension $D = 250$ were used.

For the case of the density operator approach, the OSEE provided by the MPO representation of the density matrix (Eq.(7.14)) is given by

$$S_{\#} = - \sum_{\alpha_i} (\lambda_{\alpha_i})^2 \log (\lambda_{\alpha_i})^2, \quad (7.20)$$

for bond $i = N/2$ with bond index α_i . The OSEE is a measure of the factorizability of the density matrix and thus its unbound growth signals the breakdown of the MPO approach.

In Fig.7.6 we compare the evolution of the entanglement entropy (dashed lines) and

the OSEE (solid lines) for different interaction strengths and baths starting from a CDW. For comparison, we calculated the entanglement entropy using a logarithm with base equal to the local Hilbert space dimension for both the quantum trajectory method ($d = 2$) and the density matrix evolution ($d = 4$).

In the case of strong interactions ($U = 50J$) we observe similar behaviour as the one Fig.7.5 with the OSEE remaining small until a relevant number of particles have been removed from the system, what enables dynamics. We observe a sharper growth and decay of the OSEE compared to S_{vN} but the profiles are qualitatively similar. The richer behaviour comes in the limit of weak interactions ($U = 2J$). In the closed system (grey), the OSEE exhibits the logarithmic growth that we observed for pure states, limiting our numerical ability to simulate it in the later times ($t \sim 100J$). The addition of dephasing (blue) decreases the OSEE for intermediate times, leading again to a logarithmic growth at long times (see [136]) that we observe towards the end of the simulated time. In contrast, the addition of dephasing does not affect the pure state entanglement entropy (blue dashed) that sits on top of the close system value. Furthermore, if we analyze the inclusion of losses (orange), the profiles are similar to the close system until $t \sim \gamma_i^{-1}$ when losses in the system become significant and a sudden drop in the OSEE is observed. It is important to note that at those times the population fraction is still significant and we cannot link to vanishing densities; then, loss is also preventing the persistence of correlations. Similar behaviour is observed for S_{vN} but with a slower growth and decay. Finally, if dephasing is present on top of losses, we observe a faster drop in both the OSEE and S_{vN} with a similar qualitative behaviour.

It is important to highlight now the differences we have observed between the entanglement entropy using both methods which are specially noticeable in the case of dephasing only. In all the cases studied, the trajectory approach provides curves that evolve more smoothly, we expect experimental results, which also have this probabilistic nature, to remain closer to the trajectory case. The differences between S_{vN} and OSEE become important when dephasing is added to the system. In the trajectory approach S_{vN} is mostly unaffected by the presence of dephasing. On the other hand, in the density matrix approach, the dephasing (that we represent as

a local density measurement) resets the system into a product state, disentangling the system. This property is obviously lost in a pure state picture. Thus, we can conclude that in the case of analyzing this system subject to dephasing at long times, the use of the MPO representation of the density operator can be quite advantageous.

7.5 Conclusion

In this chapter, we have computed the time evolution of an open fermionic many-body systems coupled to a bath, modeling relevant experimental conditions and discussing the interplay between interactions, loss and dephasing. In order to do so, we have combined a number-conserving quantum trajectory approach (as presented in chapter 6) and a MPO approach to directly compute the Lindbladian evolution preserving the ‘bond-parity’ symmetry sectors. The latter has proven to be well suited for the simulation of complex (mixed) initial states and efficient for the computation of long-time open dynamics. All this has given insight into the effects of dissipation on many-body localized states that are relevant in recent experiments.

In particular, we have focused on the effects of single-particle loss deep in the many-body localized phase. We have determined that especially in the presence of strong interactions, losses can enhance the dynamics in the localized phase, so reducing the stationary density imbalance. The results obtained agreed with the intuition gained from the phenomenological model that we proposed. Also, we have identified parameter regimes where loss or dephasing become the dominant dissipation mechanism, modifying the long-time behaviour of imbalance; even inducing thermalization in the system. Moreover, we have studied entanglement properties of the system and how different methods can provide an efficient representation of the open dynamics.

The methods presented are potentially useful to describe other systems such as experiments with large dipole-dipole interaction, e.g. lattice models with Erbium atoms [184]. Another possible system of study would be the case of quasi-periodic systems where we do not consider random local profiles but rather quasi-crystal structures.

Chapter 8

Conclusion

In this thesis we have presented a set of examples in the wide range of applications of cold atom systems not only towards quantum simulation but also in the context of quantum enhanced metrology. Cold atoms in optical lattices represent a powerful platform thanks to their high experimental tunability and flexibility and, also, the good microscopic characterization under well-controlled approximations that we possess of such systems, both as closed and open systems. Despite the theoretical and experimental effort in describing ultracold gases there are still interesting fundamental questions left to be answered, such as a better description of the properties beyond 1D or the characterization of out-of-equilibrium phases. Below, we discuss some of the directions in which we would like to drive the research projects presented in this thesis.

In chapter 5, we demonstrated the robust preparation of spin-symmetric states in fermionic models through the combination of coherent and dissipative driving for moderate system sizes. However, a proper characterization of the timescales of the stroboscopic scheme (and its scaling with N) for experimentally-relevant system sizes is essential. This requires to investigate the system dynamics beyond standard TEBD where the entanglement built-up in the system is too large to properly characterize the steady state. Alternatively, we would like to implement the number-conserving algorithm (as it was the case for chapter 6 and 7) for this model; another possibility is to study the time evolution through TDVP [123]. In addition, the variational approach presented in section 4.4.2 could allow us to investigate if the proposed

steady state is also reached in larger systems while not providing information of the timescales. Beyond the use of alternative numerical tools in the problem, we would like to analyze other experimental possibilities such as full-optical schemes using Raman sideband cooling [124] or optical transitions to metastable states to relax the requirement of sympathetic cooling.

In chapter 6, we have shown how dissipative dynamics can herald closed-system properties such as particle statistics for system that are identical in the absence of dissipation. We are interested in investigating if these differences are present in other scenarios such as quasi-periodic systems which links naturally with ideas of disordered systems and MBL and nicely connect to chapter 7. There is a growing interest in describing the phases near the MBL-to-thermal transition which are less well-understood and it would be interesting to apply open quantum system ideas to such intermediate phases. Moreover, incoherent processes can drastically modify the known phases of matter or even create new ones. A new field has emerged focused on the characterization of dynamical critical phenomena and the emergence of new universality classes through dissipation, see [64, 65].

In chapter 7, we characterize the role of different dissipation sources in the behaviour of systems with intrinsically long timescales, i.e. MBL systems. Moreover, in any open quantum system, we require powerful numerical tools that can efficiently describe the dissipative dynamics. We have observed that certain types of dissipation can positively impact our DMRG representation of the dynamics, such as dephasing notably reducing the OSEE at intermediate times while not affecting the required numerical resources of quantum trajectories. Thus, it is interesting to compare the different approaches to the numerical solution of dissipative evolution (quantum trajectories [92], MPO mapping of the density operator[139], variational approach [108] and so on) and construct a robust numerical toolbox that exploit the advantages of the different methods.

All in all, the open system perspective is an efficient way of dealing with many non-equilibrium problems, by tracing out part of the many-body problem in such a way that we only keep the more relevant degrees of freedom. This becomes

particularly relevant in the case of complex environments or S-E couplings in which we have to go beyond the usual approximations [185], like Markov or Lindblad. The rising number of applications based on out-of-equilibrium quantum system, e.g. dissipative driven Floquet systems [186], are making the open system perspective indispensable in the theoretical description.

Bibliography

- [1] I. Bloch, J. Dalibard, and S. Nascimbene. Quantum simulations with ultracold quantum gases. *Nat Phys*, 8(4):267–276, 2012.
- [2] A. J. Leggett. What do we know about high t_c ? *Nature Physics*, 2:134, 2006.
- [3] J. J . Bollinger, W. M. Itano, D. J. Wineland, and D. J. Heinzen. Optimal frequency measurements with maximally correlated states. *Phys. Rev. A*, 54:R4649–R4652, 1996.
- [4] J. Hald, J. L. Sørensen, C. Schori, and E. S. Polzik. Spin squeezed atoms: A macroscopic entangled ensemble created by light. *Phys. Rev. Lett.*, 83:1319–1322, 1999.
- [5] V. Giovannetti, S. Lloyd, and L. Maccone. Quantum-enhanced measurements: Beating the standard quantum limit. *Science*, 306(5700):1330–1336, 2004.
- [6] C. Gross, T. Zibold, E. Nicklas, J. Estève, and M. K. Oberthaler. Nonlinear atom interferometer surpasses classical precision limit. *Nature*, 464:1165, 2010.
- [7] M. Greiner, O. Mandel, T. Esslinger, T. W. Hänsch, and I. Bloch. Quantum phase transition from a superfluid to a mott insulator in a gas of ultracold atoms. *Nature*, 415:39, 2002.
- [8] T. Stöferle, H. Moritz, C. Schori, M. Köhl, and T. Esslinger. Transition from a strongly interacting 1d superfluid to a mott insulator. *Phys. Rev. Lett.*, 92:130403, 2004.
- [9] H. Metcalf and P. van der Straten. *Laser Cooling and Trapping*. Graduate Texts in Contemporary Physics Springer New York, 1999.

- [10] W. Ketterle and N.J. Van Druten. Evaporative cooling of trapped atoms. volume 37 of *Advances In Atomic, Molecular, and Optical Physics*, pages 181 – 236. Academic Press, 1996.
- [11] F. Schreck, G. Ferrari, K. L. Corwin, J. Cubizolles, L. Khaykovich, M.-O. Mewes, and C. Salomon. Sympathetic cooling of bosonic and fermionic lithium gases towards quantum degeneracy. *Phys. Rev. A*, 64:011402, 2001.
- [12] D. C. McKay and B. DeMarco. Cooling in strongly correlated optical lattices: prospects and challenges. *Reports on Progress in Physics*, 74(5):054401, 2011.
- [13] M. H. Anderson, J. R. Ensher, M. R. Matthews, C. E. Wieman, and E. A. Cornell. Observation of bose-einstein condensation in a dilute atomic vapor. *Science*, 269(5221):198–201, 1995.
- [14] C. C. Bradley, C. A. Sackett, J. J. Tollett, and R. G. Hulet. Evidence of bose-einstein condensation in an atomic gas with attractive interactions. *Phys. Rev. Lett.*, 75:1687–1690, 1995.
- [15] K. B. Davis, M. O. Mewes, M. R. Andrews, N. J. van Druten, D. S. Durfee, D. M. Kurn, and W. Ketterle. Bose-einstein condensation in a gas of sodium atoms. *Phys. Rev. Lett.*, 75:3969–3973, 1995.
- [16] E. A. Donley, N. R. Claussen, S. T. Thompson, and C. E. Wieman. Atom–molecule coherence in a bose–einstein condensate. *Nature*, 417:529, 2002.
- [17] T. Loftus, C. A. Regal, C. Ticknor, J. L. Bohn, and D. S. Jin. Resonant control of elastic collisions in an optically trapped fermi gas of atoms. *Phys. Rev. Lett.*, 88:173201, 2002.
- [18] M. Theis, G. Thalhammer, K. Winkler, M. Hellwig, G. Ruff, R. Grimm, and J. Hecker Denschlag. Tuning the scattering length with an optically induced feshbach resonance. *Phys. Rev. Lett.*, 93:123001, 2004.
- [19] M. P. A. Fisher, P. B. Weichman, G. Grinstein, and D. S. Fisher. Boson localization and the superfluid-insulator transition. *Phys. Rev. B*, 40:546–570, 1989.

- [20] B. DeMarco and D. S. Jin. Onset of fermi degeneracy in a trapped atomic gas. *Science*, 285(5434):1703–1706, 1999.
- [21] B. DeMarco, S. B. Papp, and D. S. Jin. Pauli blocking of collisions in a quantum degenerate atomic fermi gas. *Phys. Rev. Lett.*, 86:5409–5412, 2001.
- [22] A. G. Truscott, K. E. Strecker, W. I. McAlexander, G. B. Partridge, and R. G. Hulet. Observation of fermi pressure in a gas of trapped atoms. *Science*, 291(5513):2570–2572, 2001.
- [23] R. Jördens, N. Strohmaier, K. Günter, H. Moritz, and T. Esslinger. A mott insulator of fermionic atoms in an optical lattice. *Nature*, 455:204, 2008.
- [24] U. Schneider, L. Hackermüller, S. Will, Th. Best, I. Bloch, T. A. Costi, R. W. Helmes, D. Rasch, and A. Rosch. Metallic and insulating phases of repulsively interacting fermions in a 3d optical lattice. *Science*, 322(5907):1520–1525, 2008.
- [25] T. Fukuhara, A. Kantian, M. Endres, M. Cheneau, P. Schauß, S. Hild, D. Bellem, U. Schollwöck, T. Giamarchi, C. Gross, I. Bloch, and S. Kuhr. Quantum dynamics of a mobile spin impurity. *Nature Physics*, 9:235, 2013.
- [26] M. Schreiber, S. S. Hodgman, P. Bordia, H. P. Lüschen, M. H. Fischer, R. Vosk, E. Altman, U. Schneider, and I. Bloch. Observation of many-body localization of interacting fermions in a quasirandom optical lattice. *Science*, 349(6250):842–845, 2015.
- [27] W. S. Bakr, J. I. Gillen, A. Peng, S. Fölling, and M. Greiner. A quantum gas microscope for detecting single atoms in a hubbard-regime optical lattice. *Nature*, 462:74, 2009.
- [28] J. F. Sherson, C. Weitenberg, M. Endres, M. Cheneau, I. Bloch, and S. Kuhr. Single-atom-resolved fluorescence imaging of an atomic mott insulator. *Nature*, 467:68, 2010.
- [29] M. Boll, T. A. Hilker, G. Salomon, A. Omran, J. Nespolo, L. Pollet, I. Bloch, and C. Gross. Spin- and density-resolved microscopy of antiferromagnetic correlations in fermi-hubbard chains. *Science*, 353(6305):1257–1260, 2016.

- [30] M. F. Parsons, A. Mazurenko, C. S. Chiu, G. Ji, D. Greif, and M. Greiner. Site-resolved measurement of the spin-correlation function in the fermi-hubbard model. *Science*, 353(6305):1253–1256, 2016.
- [31] L. W. Cheuk, M. A. Nichols, K. R. Lawrence, M. Okan, H. Zhang, E. Khatami, N. Trivedi, T. Paiva, M. Rigol, and M. W. Zwierlein. Observation of spatial charge and spin correlations in the 2d fermi-hubbard model. *Science*, 353(6305):1260–1264, 2016.
- [32] P. T. Brown, D. Mitra, E. Guardado-Sanchez, P. Schauß, S. S. Kondov, E. Khatami, T. Paiva, N. Trivedi, D. A. Huse, and W. S. Bakr. Observation of canted antiferromagnetism with ultracold fermions in an optical lattice. 2016.
- [33] E. Haller, J. Hudson, A. Kelly, D. A. Cotta, B. Peaudecerf, G. D. Bruce, and S. Kuhr. Single-atom imaging of fermions in a quantum-gas microscope. *Nat Phys*, 11(9):738–742, 2015.
- [34] G. J. A. Edge, R. Anderson, D. Jervis, D. C. McKay, R. Day, S. Trotzky, and J. H. Thywissen. Imaging and addressing of individual fermionic atoms in an optical lattice. *Phys. Rev. A*, 92:063406, 2015.
- [35] S. R. White. Density matrix formulation for quantum renormalization groups. *Phys. Rev. Lett.*, 69:2863–2866, 1992.
- [36] S. R. White. Density-matrix algorithms for quantum renormalization groups. *Phys. Rev. B*, 48:10345–10356, 1993.
- [37] S. Östlund and S. Rommer. Thermodynamic limit of density matrix renormalization. *Phys. Rev. Lett.*, 75:3537–3540, 1995.
- [38] S. Rommer and S. Östlund. Class of ansatz wave functions for one-dimensional spin systems and their relation to the density matrix renormalization group. *Phys. Rev. B*, 55:2164–2181, 1997.
- [39] G. Vidal. Efficient classical simulation of slightly entangled quantum computations. *Phys. Rev. Lett.*, 91:147902, 2003.

- [40] A. J. Daley, C. Kollath, U. Schollwöck, and G. Vidal. Time-dependent density-matrix renormalization-group using adaptive effective hilbert spaces. *Journal of Statistical Mechanics: Theory and Experiment*, 2004(04):P04005, 2004.
- [41] S. R. White and A. E. Feiguin. Real-time evolution using the density matrix renormalization group. *Phys. Rev. Lett.*, 93:076401, 2004.
- [42] F. Verstraete, V. Murg, and J.I. Cirac. Matrix product states, projected entangled pair states, and variational renormalization group methods for quantum spin systems. *Advances in Physics*, 57(2):143–224, 2008.
- [43] H. P. Breuer and Petruccione F. *The theory of open quantum systems*. Oxford University Press, 2007.
- [44] C. Gardiner and P. Zoller. *Quantum noise: A handbook of Markovian and non-Markovian quantum stochastic methods with applications to quantum optics*. Berlin: Springer, 2004.
- [45] J. Dalibard, Y. Castin, and K. Mølmer. Wave-function approach to dissipative processes in quantum optics. *Phys. Rev. Lett.*, 68:580–583, 1992.
- [46] R. Dum, P. Zoller, and H. Ritsch. Monte carlo simulation of the atomic master equation for spontaneous emission. *Phys. Rev. A*, 45:4879–4887, 1992.
- [47] K. Mølmer, Y. Castin, and J. Dalibard. Monte carlo wave-function method in quantum optics. *J. Opt. Soc. Am. B*, 10(3):524–538, 1993.
- [48] H. J. Carmichael. *An Open Systems Approach to Quantum Optics*. Springer, Berlin, 1993.
- [49] M. Müller, S. Diehl, G. Pupillo, and P. Zoller. Engineered open systems and quantum simulations with atoms and ions. In Paul Berman, Ennio Arimondo, and Chun Lin, editors, *Advances in Atomic, Molecular, and Optical Physics*, volume 61 of *Advances In Atomic, Molecular, and Optical Physics*, pages 1 – 80. Academic Press, 2012.

- [50] J. Brossel, A. Kastler, and J. Winter. Création optique d'une inégalité de population entre les sous-niveaux zeeman de l'état fondamental des atomes. *J. phys. radium*, 13(12):668–668, 1952.
- [51] A. J. Daley, P. O. Fedichev, and P. Zoller. Single-atom cooling by superfluid immersion: A nondestructive method for qubits. *Phys. Rev. A*, 69:022306, 2004.
- [52] A. Aspect, E. Arimondo, R. Kaiser, N. Vansteenkiste, and C. Cohen-Tannoudji. Laser cooling below the one-photon recoil energy by velocity-selective coherent population trapping. *Phys. Rev. Lett.*, 61:826–829, 1988.
- [53] M. Kasevich and S. Chu. Laser cooling below a photon recoil with three-level atoms. *Phys. Rev. Lett.*, 69:1741–1744, 1992.
- [54] A. Griessner, A. J. Daley, S. R. Clark, D. Jaksch, and P. Zoller. Dark-state cooling of atoms by superfluid immersion. *Phys. Rev. Lett.*, 97:220403, 2006.
- [55] A. Griessner, A. J. Daley, S. R. Clark, D. Jaksch, and P. Zoller. Dissipative dynamics of atomic hubbard models coupled to a phonon bath: dark state cooling of atoms within a bloch band of an optical lattice. *New Journal of Physics*, 9(2):44, 2007.
- [56] S. Diehl, A. Micheli, A. Kantian, B. Kraus, H. P. Büchler, and P. Zoller. Quantum states and phases in driven open quantum systems with cold atoms. *Nature Physics*, 4:878, 2008.
- [57] B. Kraus, H. P. Büchler, S. Diehl, A. Kantian, A. Micheli, and P. Zoller. Preparation of entangled states by quantum markov processes. *Phys. Rev. A*, 78:042307, 2008.
- [58] M. Foss-Feig, A. J. Daley, J. K. Thompson, and A. M. Rey. Steady-state many-body entanglement of hot reactive fermions. *Phys. Rev. Lett.*, 109:230501, 2012.
- [59] M. J. Martin, M. Bishof, M. D. Swallows, X. Zhang, C. Benko, J. von Stecher, A. V. Gorshkov, A. M. Rey, and Jun Ye. A quantum many-body spin system in an optical lattice clock. *Science*, 341(6146):632–636, 2013.

- [60] S. Diehl, E. Rico, M. A. Baranov, and P. Zoller. Topology by dissipation in atomic quantum wires. *Nature Physics*, 7:971, 2011.
- [61] C. E. Bardyn, M. A. Baranov, C. V. Kraus, E. Rico, A. İmamoğlu, P. Zoller, and S. Diehl. Topology by dissipation. *New Journal of Physics*, 15(8):085001, 2013.
- [62] A. J. Daley, J. M. Taylor, S. Diehl, M. Baranov, and P. Zoller. Atomic three-body loss as a dynamical three-body interaction. *Phys. Rev. Lett.*, 102:040402, 2009.
- [63] A. Kantian, M. Dalmonte, S. Diehl, W. Hofstetter, P. Zoller, and A. J. Daley. Atomic color superfluid via three-body loss. *Phys. Rev. Lett.*, 103:240401, 2009.
- [64] L. M. Sieberer, S. D. Huber, E. Altman, and S. Diehl. Dynamical critical phenomena in driven-dissipative systems. *Phys. Rev. Lett.*, 110:195301, 2013.
- [65] L. M. Sieberer, S. D. Huber, E. Altman, and S. Diehl. Nonequilibrium functional renormalization for driven-dissipative bose-einstein condensation. *Phys. Rev. B*, 89:134310, 2014.
- [66] R. Grimm, M. Weidemüller, and Y. B. Ovchinnikov. Optical dipole traps for neutral atoms. volume 42 of *Advances In Atomic, Molecular, and Optical Physics*, pages 95 – 170. Academic Press, 2000.
- [67] C. Gerry, P. Knight, and P.L. Knight. *Introductory Quantum Optics*. Cambridge University Press, 2005.
- [68] Y. Castin. In: *Kaiser R., Westbrook C., David F. (eds) Coherent atomic matter waves. Les Houches - Ecole d'Ete de Physique Theorique*, volume 72. Springer, 2001.
- [69] C. J. Pethick and H. Smith. *Bose–Einstein Condensation in Dilute Gases*. Cambridge University Press, 2 edition, 2008.
- [70] S. Inouye, M. R. Andrews, J. Stenger, H. J. Miesner, D. M. Stamper-Kurn, and W. Ketterle. Observation of feshbach resonances in a bose–einstein condensate. *Nature*, 392:151, 1998.

- [71] E. Timmermans, P. Tommasini, M. Hussein, and A. Kerman. Feshbach resonances in atomic bose–einstein condensates. *Physics Reports*, 315(1):199 – 230, 1999.
- [72] G. H. Wannier. The structure of electronic excitation levels in insulating crystals. *Phys. Rev.*, 52:191–197, 1937.
- [73] W. Kohn. Analytic properties of bloch waves and wannier functions. *Phys. Rev.*, 115:809–821, 1959.
- [74] N.W. Ashcroft and N.D. Mermin. *Solid State Physics*. Saunders College, Philadelphia, 1976.
- [75] J. Hubbard. Electron correlations in narrow energy bands. *Proceedings of the Royal Society of London A: Mathematical, Physical and Engineering Sciences*, 276(1365):238–257, 1963.
- [76] F. H. L. Essler, H. Frahm, F. Göhmann, A. Klümper, and V. E. Korepin. *The One-Dimensional Hubbard Model*. Cambridge University Press, 2005.
- [77] T. Esslinger. Fermi-hubbard physics with atoms in an optical lattice. *Annual Review of Condensed Matter Physics*, 1(1):129–152, 2010.
- [78] P. Nozières and S. Schmitt-Rink. Bose condensation in an attractive fermion gas: From weak to strong coupling superconductivity. 59: 195, 1985.
- [79] A. F. Ho, M. A. Cazalilla, and T. Giamarchi. Quantum simulation of the hubbard model: The attractive route. *Phys. Rev. A*, 79:033620, 2009.
- [80] A. Toschi, P. Barone, M. Capone, and C. Castellani. Pairing and superconductivity from weak to strong coupling in the attractive hubbard model. *New Journal of Physics*, 7(1):7, 2005.
- [81] F. Werner, O. Parcollet, A. Georges, and S. R. Hassan. Interaction-induced adiabatic cooling and antiferromagnetism of cold fermions in optical lattices. *Phys. Rev. Lett.*, 95:056401, 2005.

- [82] S. Trotzky, P. Cheinet, S. Fölling, M. Feld, U. Schnorrberger, A. M. Rey, A. Polkovnikov, E. A. Demler, M. D. Lukin, and I. Bloch. Time-resolved observation and control of superexchange interactions with ultracold atoms in optical lattices. *Science*, 319(5861):295–299, 2008.
- [83] S. Sachdev. *Quantum Phase Transitions*. Cambridge University Press, 2001.
- [84] W. Krauth, M. Caffarel, and J. P. Bouchaud. Gutzwiller wave function for a model of strongly interacting bosons. *Phys. Rev. B*, 45:3137–3140, 1992.
- [85] T. D. Kühner, S. R. White, and H. Monien. One-dimensional bose-hubbard model with nearest-neighbor interaction. *Phys. Rev. B*, 61:12474–12489, 2000.
- [86] U. M. Ascher and L. R. Petzold. *Computer methods for ordinary differential equations and differential-algebraic equations*, volume 61. Siam, 1998.
- [87] Y. Saad. *Numerical Methods for Large Eigenvalue Problems*. Algorithms and architectures for advanced scientific computing. Manchester University Press, 1992.
- [88] R. B. Sidje. Expokit: a software package for computing matrix exponentials. *ACM Transactions on Mathematical Software (TOMS)*, 24(1):130–156, 1998.
- [89] A. T. Sornborger and E. D. Stewart. Higher-order methods for simulations on quantum computers. *Phys. Rev. A*, 60:1956–1965, 1999.
- [90] C. Cohen-Tannoudji and D. Guèry-Odelin. *Advances in Atomic Physics: An Overview*. World Scientific, 2011.
- [91] R. Alicki and K. Lendi. *Quantum Dynamical Semigroups and Applications*, volume 717 of *Lect. Notes Phys.* Springer, Berlin, 2007.
- [92] A. J. Daley. Quantum trajectories and open many-body quantum systems. *Advances in Physics*, 63(2):77–149, 2014.
- [93] G. Lindblad. On the generators of quantum dynamical semigroups. *Comm. Math. Phys.*, 48(2):119–130, 1976.

- [94] C. W. Gardiner and M. J. Collett. Input and output in damped quantum systems: Quantum stochastic differential equations and the master equation. *Phys. Rev. A*, 31:3761–3774, 1985.
- [95] M. B. Plenio and P. L. Knight. The quantum-jump approach to dissipative dynamics in quantum optics. *Rev. Mod. Phys.*, 70:101–144, 1998.
- [96] F. Verstraete and J. I. Cirac. Matrix product states represent ground states faithfully. *Phys. Rev. B*, 73:094423, 2006.
- [97] F. Verstraete, J. J. García-Ripoll, and J. I. Cirac. Matrix product density operators: Simulation of finite-temperature and dissipative systems. *Phys. Rev. Lett.*, 93:207204, 2004.
- [98] B. Pirvu, V. Murg, J. I. Cirac, and F. Verstraete. Matrix product operator representations. *New Journal of Physics*, 12(2):025012, 2010.
- [99] U. Schollwöck. The density-matrix renormalization group in the age of matrix product states. *Annals of Physics*, 326(1):96 – 192, 2011. January 2011 Special Issue.
- [100] M. A. Nielsen and I. L. Chuang. *Quantum Computation and Quantum Information: 10th Anniversary Edition*. Cambridge University Press, 2010.
- [101] M. B. Hastings. An area law for one-dimensional quantum systems. *Journal of Statistical Mechanics: Theory and Experiment*, 2007(08):P08024, 2007.
- [102] M. M. Wolf, F. Verstraete, M. B. Hastings, and J. I. Cirac. Area laws in quantum systems: Mutual information and correlations. *Phys. Rev. Lett.*, 100:070502, 2008.
- [103] J. Eisert, M. Cramer, and M. B. Plenio. Colloquium: Area laws for the entanglement entropy. *Rev. Mod. Phys.*, 82:277–306, 2010.
- [104] D. Poulin, A. Qarry, R. Somma, and F. Verstraete. Quantum simulation of time-dependent hamiltonians and the convenient illusion of hilbert space. *Phys. Rev. Lett.*, 106:170501, 2011.

- [105] U. Schollwöck. The density-matrix renormalization group. *Rev. Mod. Phys.*, 77:259–315, 2005.
- [106] I. P. McCulloch. From density-matrix renormalization group to matrix product states. *Journal of Statistical Mechanics: Theory and Experiment*, 2007(10):P10014, 2007.
- [107] M. L. Wall and L. D. Carr. Out-of-equilibrium dynamics with matrix product states. *New Journal of Physics*, 14(12):125015, 2012.
- [108] J. Cui, J. I. Cirac, and M. C. Bañuls. Variational matrix product operators for the steady state of dissipative quantum systems. *Phys. Rev. Lett.*, 114:220601, 2015.
- [109] G. De las Cuevas, N. Schuch, D. Pérez-García, and J. I. Cirac. Purifications of multipartite states: limitations and constructive methods. *New Journal of Physics*, 15(12):123021, 2013.
- [110] M. Lubasch, J. I. Cirac, and M. C. Bañuls. Algorithms for finite projected entangled pair states. *Phys. Rev. B*, 90:064425, 2014.
- [111] E. Mascarenhas, H. Flayac, and V. Savona. Matrix-product-operator approach to the nonequilibrium steady state of driven-dissipative quantum arrays. *Phys. Rev. A*, 92:022116, 2015.
- [112] D. J. Wineland, J. J. Bollinger, W. M. Itano, F. L. Moore, and D. J. Heinzen. Spin squeezing and reduced quantum noise in spectroscopy. *Phys. Rev. A*, 46:R6797–R6800, 1992.
- [113] A. Solomon. Quantum measurement and control, by h.m. wiseman and g.j. milburn. *Contemporary Physics*, 52(2):162–163, 2011.
- [114] V. Giovannetti, S. Lloyd, and L. Maccone. Advances in quantum metrology. *Nature Photonics*, 5:222, 2011.
- [115] W. Yi, S. Diehl, A. J. Daley, and P. Zoller. Driven-dissipative many-body pairing states for cold fermionic atoms in an optical lattice. *New Journal of Physics*, 14(5):055002, 2012.

- [116] C. W. Helstrom. Quantum detection and estimation theory. *Journal of Statistical Physics*, 1(2):231–252, 1969.
- [117] M. G. A. Paris. Quantum estimation for quantum technology. *International Journal of Quantum Information*, 07(supp01):125–137, 2009.
- [118] P. Hyllus, W. Laskowski, R. Krischek, C. Schwemmer, W. Wieczorek, H. Weinfurter, L. Pezzé, and A. Smerzi. Fisher information and multiparticle entanglement. *Phys. Rev. A*, 85:022321, 2012.
- [119] H. Cramer. *Mathematical Methods of Statistics*. Princeton University Press, 1946.
- [120] A. S. Holevo. *Probabilistic and Statistical Aspects of Quantum Theory*, volume 34. North-Holland, Amsterdam, 1982.
- [121] S. L. Braunstein and C. M. Caves. Statistical distance and the geometry of quantum states. *Phys. Rev. Lett.*, 72:3439–3443, 1994.
- [122] V. Giovannetti, S. Lloyd, and L. Maccone. Quantum metrology. *Phys. Rev. Lett.*, 96:010401, 2006.
- [123] J. Haegeman, J. I. Cirac, T. J. Osborne, I. Pižorn, H. Verschelde, and F. Verstraete. Time-dependent variational principle for quantum lattices. *Phys. Rev. Lett.*, 107:070601, 2011.
- [124] A. Reiserer, C. Nölleke, S. Ritter, and G. Rempe. Ground-state cooling of a single atom at the center of an optical cavity. *Phys. Rev. Lett.*, 110:223003, 2013.
- [125] J. Yago Malo, E. P. L. van Nieuwenburg, M. H. Fischer, and A. J. Daley. Particle statistics and lossy dynamics of ultracold atoms in optical lattices. *Phys. Rev. A*, 97:053614, 2018.
- [126] T. Gericke, P. Wurtz, D. Reitz, T. Langen, and H. Ott. High-resolution scanning electron microscopy of an ultracold quantum gas. *Nat Phys*, 4(12):949–953, 2008.

- [127] C. Weitenberg, M. Endres, J. F. Sherson, M. Cheneau, P. Schausz, T. Fukuhara, I. Bloch, and S. Kuhr. Single-spin addressing in an atomic mott insulator. *Nature*, 471(7338):319–324, 2011.
- [128] M. Lewenstein, A. Sanpera, and V. Ahufinger. *Ultracold Atoms in Optical Lattices: Simulating quantum many-body systems*. OUP Oxford, 2012.
- [129] P. Barmettler and C. Kollath. Controllable manipulation and detection of local densities and bipartite entanglement in a quantum gas by a dissipative defect. *Phys. Rev. A*, 84:041606, 2011.
- [130] H. Pichler, A. J. Daley, and P. Zoller. Nonequilibrium dynamics of bosonic atoms in optical lattices: Decoherence of many-body states due to spontaneous emission. *Phys. Rev. A*, 82:063605, 2010.
- [131] S. Sarkar, S. Langer, J. Schachenmayer, and A. J. Daley. Light scattering and dissipative dynamics of many fermionic atoms in an optical lattice. *Phys. Rev. A*, 90:023618, 2014.
- [132] M. Müller, S. Diehl, G. Pupillo, and P. Zoller. Engineered open systems and quantum simulations with atoms and ions. *Advances In Atomic, Molecular, and Optical Physics*, 61:1 – 80, 2012. *Advances in Atomic, Molecular, and Optical Physics*.
- [133] I. Vidanović, D. Cocks, and W. Hofstetter. Dissipation through localized loss in bosonic systems with long-range interactions. *Phys. Rev. A*, 89:053614, 2014.
- [134] G. Kordas, S. Wimberger, and D. Witthaut. Dissipation-induced macroscopic entanglement in an open optical lattice. *EPL (Europhysics Letters)*, 100(3):30007, 2012.
- [135] H. P. Lüschen, P. Bordia, S. S. Hodgman, M. Schreiber, S. Sarkar, A. J. Daley, M. H. Fischer, E. Altman, I. Bloch, and U. Schneider. Signatures of many-body localization in a controlled open quantum system. *Phys. Rev. X*, 7:011034, 2017.
- [136] M. V. Medvedyeva, T. Prosen, and M. Žnidarič. Influence of dephasing on many-body localization. *Phys. Rev. B*, 93:094205, 2016.

- [137] E. Levi, M. Heyl, I. Lesanovsky, and J. P. Garrahan. Robustness of many-body localization in the presence of dissipation. *Phys. Rev. Lett.*, 116:237203, 2016.
- [138] M. H Fischer, M. Maksymenko, and E. Altman. Dynamics of a many-body-localized system coupled to a bath. *Phys. Rev. Lett.*, 116:160401, 2016.
- [139] E. P. L. van Nieuwenburg, J. Yago Malo, A. J. Daley, and M. H. Fischer. Dynamics of many-body localization in the presence of particle loss. *Quantum Science and Technology*, 3(1):01LT02, 2018.
- [140] M. Girardeau. Relationship between systems of impenetrable bosons and fermions in one dimension. *Journal of Mathematical Physics*, 1(6):516–523, 1960.
- [141] T. Kinoshita, T. Wenger, and D. S. Weiss. Observation of a one-dimensional tonks-girardeau gas. *Science*, 305(5687):1125–1128, 2004.
- [142] B. Paredes, A. Widera, V. Murg, O. Mandel, S. Folling, I. Cirac, G. V. Shlyapnikov, T. W. Hansch, and I. Bloch. Tonks-girardeau gas of ultracold atoms in an optical lattice. *Nature*, 429(6989):277–281, 2004.
- [143] P. M. Preiss, R. Ma, M. E. Tai, A. Lukin, M. Rispoli, P. Zupancic, Y. Lahini, R. Islam, and M. Greiner. Strongly correlated quantum walks in optical lattices. *Science*, 347(6227):1229–1233, 2015.
- [144] T. Cheon and T. Shigehara. Fermion-boson duality of one-dimensional quantum particles with generalized contact interactions. *Phys. Rev. Lett.*, 82:2536–2539, 1999.
- [145] C. Kittel, H.K. Charles Kittel, K. Charles, H. Kroemer, K. Herbert, U.C. Kittel, and U.H. Kroemer. *Thermal Physics*. W. H. Freeman, 1980.
- [146] M. Olshanii. Atomic scattering in the presence of an external confinement and a gas of impenetrable bosons. *Phys. Rev. Lett.*, 81:938–941, 1998.
- [147] U. Schollwöck. The density-matrix renormalization group in the age of matrix product states. *Annals of Physics*, 326(1):96 – 192, 2011. January 2011 Special Issue.

- [148] E. H. Lieb and D. W. Robinson. The finite group velocity of quantum spin systems. *Commun. Math. Phys.*, 28(3):251–257, 1972.
- [149] R. Islam, R. Ma, P. M. Preiss, M. Eric Tai, A. Lukin, M. Rispoli, and M. Greiner. Measuring entanglement entropy in a quantum many-body system. *Nature*, 528(7580):77–83, 2015.
- [150] A. J. Daley, H. Pichler, J. Schachenmayer, and P. Zoller. Measuring entanglement growth in quench dynamics of bosons in an optical lattice. *Phys. Rev. Lett.*, 109:020505, 2012.
- [151] H. Pichler, L. Bonnes, A. J. Daley, A. M. Läuchli, and P. Zoller. Thermal versus entanglement entropy: a measurement protocol for fermionic atoms with a quantum gas microscope. *New Journal of Physics*, 15(6):063003, 2013.
- [152] D. Poletti, P. Barmettler, A. Georges, and C. Kollath. Emergence of glasslike dynamics for dissipative and strongly interacting bosons. *Phys. Rev. Lett.*, 111:195301, 2013.
- [153] A. Frisch, M. Mark, K. Aikawa, S. Baier, R. Grimm, A. Petrov, S. Kotochigova, G. Quéméner, M. Lepers, O. Dulieu, and F. Ferlaino. Ultracold dipolar molecules composed of strongly magnetic atoms. *Phys. Rev. Lett.*, 115:203201, 2015.
- [154] P. Barmettler, M. Punk, V. Gritsev, E. Demler, and E. Altman. Relaxation of antiferromagnetic order in spin-1/2 chains following a quantum quench. *Phys. Rev. Lett.*, 102:130603, 2009.
- [155] G. Carleo and M. Troyer. Solving the quantum many-body problem with artificial neural networks. *Science*, 355(6325):602–606, 2017.
- [156] R. Nandkishore and D. A. Huse. Many-body localization and thermalization in quantum statistical mechanics. *Annual Review of Condensed Matter Physics*, 6(1):15–38, 2015.
- [157] E. Altman and R. Vosk. Universal dynamics and renormalization in many-body-localized systems. *Annual Review of Condensed Matter Physics*, 6(1):383–409, 2015.

- [158] J. Smith, A. Lee, P. Richerme, B. Neyenhuis, P. W. Hess, P. Hauke, M. Heyl, D. A. Huse, and C. Monroe. Many-body localization in a quantum simulator with programmable random disorder. *Nature Physics*, 12:907, 2016.
- [159] P. Bordia, H. P. Lüschen, S. S. Hodgman, M. Schreiber, I. Bloch, and U. Schneider. Coupling identical one-dimensional many-body localized systems. *Phys. Rev. Lett.*, 116:140401, 2016.
- [160] J. Choi, S. Hild, J. Zeiher, P. Schauß, A. Rubio-Abadal, T. Yefsah, V. Khemani, D. A. Huse, I. Bloch, and C. Gross. Exploring the many-body localization transition in two dimensions. *Science*, 352(6293):1547–1552, 2016.
- [161] J. M. Deutsch. Quantum statistical mechanics in a closed system. *Phys. Rev. A*, 43:2046–2049, 1991.
- [162] M. Srednicki. Chaos and quantum thermalization. *Phys. Rev. E*, 50:888–901, 1994.
- [163] M. Rigol, V. Dunjko, and M. Olshanii. Thermalization and its mechanism for generic isolated quantum systems. *Nature*, 452:854, 2008.
- [164] P. W. Anderson. Absence of diffusion in certain random lattices. *Phys. Rev.*, 109:1492–1505, 1958.
- [165] D. S. Wiersma, P. Bartolini, A. Lagendijk, and R. Righini. Localization of light in a disordered medium. *Nature*, 390:671, 1997.
- [166] T. Schwartz, G. Bartal, S. Fishman, and M. Segev. Transport and anderson localization in disordered two-dimensional photonic lattices. *Nature*, 446:52, 2007.
- [167] Y. Lahini, A. Avidan, F. Pozzi, M. Sorel, R. Morandotti, D. N. Christodoulides, and Y. Silberberg. Anderson localization and nonlinearity in one-dimensional disordered photonic lattices. *Phys. Rev. Lett.*, 100:013906, 2008.
- [168] J. Billy, V. Josse, Z. Zuo, A. Bernard, B. Hambrecht, P. Lugan, D. Clément, L. Sanchez-Palencia, P. Bouyer, and A. Aspect. Direct observation of anderson localization of matter waves in a controlled disorder. *Nature*, 453:891, 2008.

- [169] S. S. Kondov, W. R. McGehee, J. J. Zirbel, and B. DeMarco. Three-dimensional anderson localization of ultracold matter. *Science*, 334(6052):66–68, 2011.
- [170] F. Jendrzejewski, A. Bernard, K. Mueller, P. Cheinet, V. Josse, M. Piraud, L. Pezzé, L. Sanchez-Palencia, A. Aspect, and P. Bouyer. Three-dimensional localization of ultracold atoms in an optical disordered potential. 8:398, 2012.
- [171] M. Žnidarič, T. Prosen, and P. Prelovšek. Many-body localization in the heisenberg xxz magnet in a random field. *Phys. Rev. B*, 77:064426, 2008.
- [172] J. H. Bardarson, F. Pollmann, and J. E. Moore. Unbounded growth of entanglement in models of many-body localization. *Phys. Rev. Lett.*, 109:017202, 2012.
- [173] B. Bauer and C. Nayak. Area laws in a many-body localized state and its implications for topological order. *Journal of Statistical Mechanics: Theory and Experiment*, 2013(09):P09005, 2013.
- [174] R. Vosk and E. Altman. Many-body localization in one dimension as a dynamical renormalization group fixed point. *Phys. Rev. Lett.*, 110:067204, 2013.
- [175] D.M. Basko, I.L. Aleiner, and B.L. Altshuler. Metal–insulator transition in a weakly interacting many-electron system with localized single-particle states. *Annals of Physics*, 321(5):1126 – 1205, 2006.
- [176] A. Pal and D. A. Huse. Many-body localization phase transition. *Phys. Rev. B*, 82:174411, 2010.
- [177] S. Iyer, V. Oganesyan, G. Refael, and D. A. Huse. Many-body localization in a quasiperiodic system. *Phys. Rev. B*, 87:134202, 2013.
- [178] S. Aubry and G. André. Analyticity breaking and anderson localization in incommensurate lattices. *Ann. Israel Phys. Soc*, 3(133):18, 1980.
- [179] W. De Roeck and F. Huveneers. Stability and instability towards delocalization in many-body localization systems. *Phys. Rev. B*, 95:155129, 2017.

-
- [180] D. J. Luitz, N. Laflorencie, and F. Alet. Many-body localization edge in the random-field heisenberg chain. *Phys. Rev. B*, 91:081103, 2015.
- [181] M. Serbyn, Z. Papić, and D. A. Abanin. Criterion for many-body localization-delocalization phase transition. *Phys. Rev. X*, 5:041047, 2015.
- [182] M. Zwolak and G. Vidal. Mixed-state dynamics in one-dimensional quantum lattice systems: A time-dependent superoperator renormalization algorithm. *Phys. Rev. Lett.*, 93:207205, 2004.
- [183] T. Prosen and I. Pižorn. Operator space entanglement entropy in a transverse ising chain. *Phys. Rev. A*, 76:032316, 2007.
- [184] S. Baier, M. J. Mark, D. Petter, K. Aikawa, L. Chomaz, Z. Cai, M. Baranov, P. Zoller, and F. Ferlaino. Extended bose-hubbard models with ultracold magnetic atoms. *Science*, 352(6282):201–205, 2016.
- [185] F. Cosco, M. Borrelli, J.J. Mendoza-Arenas, F. Plastina, D. Jaksch, and S. Maniscalco. Bose-hubbard lattice as a controllable environment for open quantum systems. *Phys. Rev. A*, 97:040101, 2018.
- [186] A. S. D. Dietrich, M. Kiffner, and D. Jaksch. Probing microscopic models for system-bath interactions via parametric driving. *Phys. Rev. A*, 98:012122, 2018.